MEASUREMENT OF TURBULENT FLOWS WITH A ROTATED HOT-FILM ANEMOMETER

by

G. L. Marsh
and
J. A. Peterka

Supported by

National Science Foundation Grant
ENG76-03135

Fluid Mechanics and Diffusion Laboratory
College of Engineering
Colorado State University
Fort Collins, Colorado 80523

May 1977

CER76-77GLM-JAP64

ABSTRACT

MEASUREMENT OF TURBULENT FLOWS

WITH A ROTATED HOT-FILM ANEMOMETER

Numerous research efforts have been devoted to measuring the velocity characteristics of turbulent flows in order to understand the nature and physical processes of these flows. A new hot-film anemometer technique to measure the mean velocity vector and the six components of Reynolds stress in turbulent flows is discussed in this report.

During the development of this measurement system, emphasis was placed on the simplicity in which velocity measurements could be obtained in a three-dimensional turbulent flow and on the accuracy of the acquired data. A Monte Carlo simulation technique was used to predict the resolution in the measurement quantities. Validation experiments were conducted by obtaining turbulent velocity measurements in a fully developed turbulent pipe flow and also in a turbulent shear flow (simulating the planetary boundary layer). Velocity measurements were also obtained in the wake of a power plant model immersed in a turbulent boundary layer to demonstrate the capability of the measurement system.

Measurements of the Reynolds stress components in the fully developed turbulent pipe flow showed good agreement with predictions based on the measured pressure drop in the pipe and data taken by other investigators. Reynolds stress measurements taken in the turbulent shear flow also compared well with data taken by other investigators.

The scatter in the measurements of the turbulent velocity components indicated that the Monte Carlo method was accurately predicting the resolution in these measurement quantities.

ACKNOWLEDGMENTS

Financial support for this research was provided under National Science Foundation Grant No. ENG 76-03135.

TABLE OF CONTENTS

LIST OF FIGURES

LIST OF SYMBOLS

Fluctuating quantities are denoted by $A = \overline{A} + a$, $\overline{A}$ is the mean component and a is the fluctuating component, $a' = \sqrt{\overline{a^2}}$.

Symbol	Definition
A	Hot-film anemometer calibration constant
A,B,C,D	Constants used in equation (2-3)
a,b	Constants used in the functional relationship of Friehe and Schwarz
A_1, A_2, A_3	Rotated hot-film anemometer calibration constants
B	Hot-film anemometer calibration constant
c	Hot-film anemometer calibration constant
D,d	Separation distance, size of cubic roughness elements
d	Diameter of hot wire (film) sensor
d_r	Defined in Figure 5
E,e	Anemometer bridge voltage
E_{rms}	Root-mean-square anemometer bridge voltage
F_i	Defined in equation (B.15)
F_j	Defined in equation (A.5)
$f_{U_j}(\overline{\theta})$	Defined in equation (B.10)
H	Height of building 1 (defined in Figure 7)
h	Defined in equation (B.2)
$h_{U_iU_j}(\overline{U}_T)$	Second partial derivative of h with respect to U_iU_j $h_{U_iU_j}(\overline{U}_T) = \partial^2 h/\partial U_i \partial U_j$
k	Constant used in the functional relationship of Hinze
k_1, k_2	Constants used in the functional relationships of Jorgensen
ℓ	Length of hot wire (film) sensor

Symbol	Definition
Nu	Nusselt number
Nu*	Corrected Nusselt number
n	Constant defined in equation (2.2)
P	Static pressure
R	Pipe radius
Re	Reynolds number
S	Defined in equation (A.3)
S	Defined in equation (B.13)
s	Defined in equation (A.3)
U,V,W	Velocities in x, y, z directions
$\overline{U}_c$	Mean velocity at the center of the pipe
$\overline{U}_\delta$	Mean velocity at the top of the boundary layer
$\overline{U}_s$	Mean swirl velocity $\overline{U}_s^2 = \overline{V}^2 + \overline{W}^2$
U_T	Total velocity vector magnitude $U_T^2 = U^2 + V^2 + W^2$
$\overline{U}_o$	Mean velocity in approach flow
$\overline{U}_o - \overline{U}$	Mean velocity defect
u_τ	Shear velocity
$\overline{uv}, \overline{uw}, \overline{vw}$	Turbulent shear stresses
X,Y,Z	Space coordinates, defined in Figure 2, Figure 5, and Figure 7
X	Defined in equation (A.7)
X	Defined in equation (B.12)
x	Random data value defined in equation (C.1)
$\overline{x}$	"Exact" experimental data value defined in equation (C.1)
Y'	(R - Y)
z	Pseudorandom number defined in equation (C.1)

Greek Symbols	Definition
α	Defined in Figure 1
β_1, β_2	Defined in Figure 10
δ	Boundary layer thickness
ε	Constant used in the functional relationship of Fujita and Kovasznay
γ	Defined in Figure 1
ϕ	Defined in Figure 10
Φ_1, Φ_2	Defined in Figure 10
ψ	Angular position of probe support axis (defined in Figure 10)
ρ	Density of air
σ	Standard deviation [defined in equation (C.1)]
θ	Angle of incidence between mean velocity vector and hot film sensor (defined in Figure 10)

Superscripts	
-	Time average
'	Root-mean-square

Chapter I

INTRODUCTION

Examples of turbulent flow occurring in nature and in engineering applications are numerous. Even if these examples are limited to the realm of wind engineering, the list would still be quite extensive. The planetary boundary layer is in turbulent motion along with the jet streams in the upper troposphere. The motion of cumulus clouds is turbulent, and the plume from a smokestack is in turbulent motion. The air flowing in the vicinity of urban centers and in the wake of buildings are in highly turbulent motion. In nature, turbulent motion is the rule rather than the exception.

Since turbulent flow is so prevalent, an extensive amount of work has been devoted to understanding its nature and physical processes. To be able to measure the mean velocity direction and magnitude in a turbulent flow is important in understanding the physical processes of the flow. Numerous research efforts have been conducted in measuring the secondary flows in fully developed turbulent flow in noncircular ducts. Hansen and Cermak (1975) have taken measurements of a weak vortex which is contained in the wake of surface obstacles that are submerged in a thick turbulent boundary layer. The measurement of this weak vortex has helped explain some of the basic physical mechanisms occurring in vortex-containing wakes.

A significant factor in understanding the characteristics of turbulent flows is the measurement of the six components of Reynolds stress. The turbulent intensity components (u', v', w') give an indication of the strength of the turbulent fluctuations in the flow.

The turbulent energy density of a turbulent field is given by $(u'^2 + v'^2 + w'^2)/2$. Shear stress components are useful in developing and verifying closure models for the equations of motion for turbulent flow.

When the techniques of hot-wire anemometry are applied to the task of obtaining measurements of the mean velocity vector and Reynolds stresses, the directional properties of the hot wire have to be considered. Normally, the procedure which is used in obtaining these measurement quantities has been to locate the mean velocity direction and yaw the hot wire to this mean velocity vector. Commonly used techniques include an X-wire probe, with two wires at 90 degrees to each other, which is positioned with each wire at 45 degrees to the mean velocity vector or a single wire which is yawed successively to X-wire positions.

The hot-film anemometry technique which is used in this thesis is different from other methods in the fact that the direction of the mean velocity vector in a three-dimensional flow does not have to be known precisely before turbulence measurements can be taken and film yaw angles to the mean flow other than 45 degrees are used. A single hot film, slanted 45 degrees to its sensor prong supports, is positioned at an arbitrary, but restricted, angle to the flow and then is rotated about the axis of its probe support. Measurements of mean and rms voltage are obtained at a number of angular positions. The mean velocity vector and velocity correlations are calculated from this data in a coordinate system which is aligned with the axis of the probe support, and then these measurement quantities are rotated to a reference coordinate system which is fixed to the boundary geometry of

the flow. Additional emphasis is placed on the fact that only one set of measurements has to be taken with this hot film sensor at each measurement location. This facilitates the measurements of the velocity characteristics by reducing the amount of time which is required to obtain the experimental data.

In order to verify the accuracy of the measurement technique which is used in this thesis, measurements of mean velocity and turbulence characteristics have been taken in two turbulent flows where measurements of these same quantities have been taken by other investigators. Velocity measurements have been taken in a fully developed turbulent pipe flow and also in a turbulent shear flow in the wind tunnel (simulating the planetary boundary layer). Finally, to illustrate the capability of this measurement technique, an extensive set of measurements has been taken in a single vertical plane in the wake of a surface mounted power plant model which is immersed in a turbulent boundary layer.

The remaining chapters are organized in the following manner: In Chapter II a brief survey will be presented on how mean and fluctuating velocity measurements in turbulent flows have been taken in the past using the techniques of hot-wire anemometry. A description of the techniques which are used in obtaining and analyzing the experimental data will be presented in Chapter III. In this chapter the development, method of operation, and the resolution in the measurements of the experimental quantities of this hot-film anemometry technique will be discussed in detail. Chapter IV contains the experimental results and and interpretation of their significance. Conclusions are presented in Chapter V along with some suggestions on further investigation relating to this measurement system.

Chapter II

LITERATURE SURVEY

Introduction

The measurement of the mean velocity vector, the three Reynolds normal stresses, and the three Reynolds shear stresses in a three-dimensional turbulent flow is a difficult task. In order to measure the mean velocity components and Reynolds stresses using hot-wire anemometry techniques, the directional sensitivities of the hot wire have to be known, thus an extensive amount of work has been conducted to understand these directional properties. This chapter is devoted to summarizing some of the work which has been conducted in investigating the directional sensitivities of the hot wire and measuring the mean velocity vector and Reynolds stresses.

Directional Sensitivities

To determine the directional sensitivities of a hot wire inclined to the mean velocity vector, Sears (1948) approached this problem theoretically by considering the laminar flow over an infinitely long cylinder inclined to a uniform velocity field. The two velocity components normal to the cylinder axis were found to be independent of the axial velocity component. Furthermore, when an infinitely long cylinder was heated uniformly along its axis, the temperature field was independent of the axial velocity component, and the rate of convective heat loss per unit length was dependent only on the normal velocity components. Thus, the cosine law was established for an infinite wire. It was generally accepted that the cosine law could be adopted when considering the convective heat loss from a cylinder of finite length.

Investigating the validity of using the cosine law for finite wires, Schubauer and Klebanoff (1946) concluded that the cosine law could be used for wires with finite length when the angle of yaw, γ, was less than 70° (Figure 1). The observable deviations from the cosine law were attributed to the aging of the wire. Assuming the cosine law to be valid, the heat transfer coefficient could then be related to the Reynolds number as follows:

$$Nu = A + B(Re \cos \gamma)^{1/2} \qquad (2\text{-}1)$$

where Nu and Re are the Nusselt and Reynolds numbers, respectively (both being based on the wire diameter).

Sandborn and Lawrence (1955) used the following equation

$$Nu = A + B\, Re^{1/2}(\cos \gamma)^{n} \qquad (2\text{-}2)$$

and concluded that n varied with each wire tested. Extensive measurements were taken changing the angle of yaw from 0° to 90°, i.e. the wire parallel to the mean velocity direction. Furthermore, it was found that the effect of the length-to-diameter ratio, l/d, on the rate of heat loss from a normal wire could be eliminated by using end loss corrections. It was assumed that these end loss corrections were invariant with a change in the yaw angle of the wire. Sandborn and Lawrence suggested an empirical relation of the form:

$$Nu = (A + B(Re \cos \gamma)^{1/2})\cos \gamma + (C + D(Re \sin \gamma)^{1/2})\sin \gamma \qquad (2\text{-}3)$$

which was based on the weighted addition of the heat losses of normal and parallel wires. However, systematic deviations were found, and thus a more accurate equation was considered necessary.

Hinze (1959) suggested that if the angle of yaw was less than 70°, the cosine law was valid. However, when the yaw angle was greater than 70°, the axial velocity component became important. For this case the effective velocity could approximately be obtained from the relation:

$$U_E^2(\gamma) = U^2(o)\ (\cos^2 \gamma + k^2 \sin^2 \gamma) \qquad (2\text{-}4)$$

where $U_E(\gamma)$ was the effective cooling velocity detected by the wire. The factor k had a value between 0.1 and 0.3 depending on the magnitude of the velocity, and it would increase with decreasing velocity. As the length-to-diameter ratio increased and for all practical purposes approached the case of an infinite wire, the value of k would become zero.

Webster (1962) used equation (2-4) and performed systematic experiments in a low-turbulence wind tunnel trying to verify that the value of k was nonzero and to determine values for the parameter under various conditions. Values of k were calculated for various velocities and 1/d ratios of the wire and the mean value $k = 0.20 \pm 0.01$ was obtained. There seemed to be no systematic variation in the value of k with a change in 1/d ratio from 86:1 to 1456:1. This was a little surprising considering that there was such a large difference between the maximum and minimum 1/d ratios, and it would seem reasonable to expect that over such a large range the value of k would decrease as the 1/d ratio increased. In other words, the largest 1/d ratio, 1456:1, seemed, for all practical purposes, to be approaching the case of an infinite wire where k would be zero.

Delleur (1966) found a good correlation existed between the corrected Nusselt number, Nu*, and the normal component of the velocity,

expressed by $Re^{1/2}(\cos \gamma)^{1/2}$, when γ was 67.5° and smaller. The corrected Nusselt number was determined by considering the conduction effect of the sensor supports. Using Hinze's relationship, the value of k was determined to be 0.176 which was smaller than the value obtained by Webster but within the range Hinze suggested.

Friehe and Schwarz (1968) used the following relationship:

$$U_E(\gamma) = U(o)\, f^2(\gamma) \qquad (2\text{-}5)$$

where $f(\gamma) = a + b \cos^{1/2} \gamma$ and a and b are parameters depending on the 1/d ratio. The above relation for $f(\gamma)$ can be written $f(\gamma) = (1-b) + b\cos^{1/2} \gamma$. For films, the relation appeared to hold quite well for the range of γ from 0° to 60°, whereas for wires, the relation appeared to be valid for an angle up to 75°. The length-to-diameter ratio of the wire was varied, and as the 1/d ratio increased from 18 to 100, the dependence of heat transfer on yaw angle approached the cosine law. The change in heat transfer from a yawed wire due to the orientation of the probe supports and vortex shedding from the wire was also considered. With the probe supports oriented transversely to the mean velocity direction, at some angle α to the mean velocity vector (Figure 1), the proposed relation for $f(\gamma)$ was found to be valid up to a critical angle depending on the velocity. For this reason, it was recommended that when measurements were taken with a sensor yawed to the mean flow, the sensor supports should be aligned such that the angle α is zero. One experiment was conducted where the Reynolds number, based on the sensor diameter, was approximately 150 which was well above the critical value of 44 for vortex shedding to occur. The relation for $f(\gamma)$ held only for angles of yaw up to 35°, thus showing that vortex shedding significantly

affected the angular dependence of the sensor. By equating equation (2-6) and Hinze's formula, a comparison between the two functional relationships was made. By using the results from their experiments, Friehe and Schwarz showed that there was a slight decrease in k with increasing γ over the range 0° to 60°. The average value of k was approximately 0.25 which was slightly higher than the value given by Webster but within the range stated by Hinze.

Jorgensen (1971) considered the problem of varying the yaw angle, γ, while keeping the pitch angle, α, equal to zero, and then changing the pitch angle keeping the yaw angle equal to zero (Figure 1). The author used Hinze's relationship to account for the differences in heat transfer

$$U_E^2(\gamma) = U^2(o)\ (\cos^2\gamma + k_1^2 \sin^2\gamma) \quad \text{for } \alpha = 0 \tag{2-6}$$

$$U_E^2(\alpha) = U^2(o)\ (\cos^2\alpha + k_2^2 \sin^2\alpha) \quad \text{for } \gamma = 0 \tag{2-7}$$

where k_1 = yaw factor

k_2 = pitch factor.

The value of k_1 was calculated for different wires and mean velocities. Since only three mean velocities were used, a dependence of k_1 on velocity could not be made. Depending on the sensor used, the value of k_1 varied between the range of 0.55 and 0.1, and it decreased with increasing values of γ. Since k_1 varied with yaw angle, it was necessary to pick a value of k_1 which would give the least error in U(o). To obtain the minimum error, k_1 should be based on some value of γ near or at the outer limit of the range of γ used in the data acquisition. The pitch factor, k_2, changed only slightly with a change

in the pitch angle. By neglecting the pitch correction, i.e. neglecting the relationship given in equation (2-7) which accounted for the change in the heat transfer from the sensor at various pitch angles of the probe body, the maximum errors in U(o) were found to be between 5 percent and 12 percent. By including the pitch correction and using the value of k_2 for $\alpha = 90°$, errors in U(o) of between 1 and 2 percent were realized. Jorgensen stated that the pitch correction was necessary because of the blockage effect of the probe body and of changes in heat conduction to the end prong supports with varying degrees of inclination relative to the direction of flow. Errors arising due to the pitch factor, k_2, will increase with decreasing prong spacing, prong length, and length-to-diameter ratio.

More recently, Champagne, Sleicker, and Wehrmann (1967) conducted extensive tests measuring the heat transfer from inclined and normal wires. The measurements indicated that the heat loss from an inclined wire was larger than that from a wire normal to the flow with the same normal component of velocity. The magnitude of the increase in heat transfer from an inclined wire over a normal wire was found to be quite small, but it was nevertheless detectable. The maximum increase occurred from the wire with the smallest length-to-diameter ratio; 1/d = 200. However, no measurable difference from the cosine law was found when the 1/d ratio was 600. The data, indicating deviations from the cosine law existed, were then correlated using Hinze's relationship. The value of k did not appear to vary as the yaw angle was changed, and k was found to be equal to 0.20 for a 1/d ratio of 200. Two kinds of hydrodynamic end effects were considered in the work by Champagne, Sleicher, and Wehrmann. The first kind of hydrodynamic end effect was the distortion

of the flow field by the end supports, which causes flow acceleration across the wire near the upstream support and flow deceleration near the downstream support. Heat transfer measurements were taken using different sizes of end supports, and the results showed that the size of the end supports did not contribute to the deviations from the cosine law. The second kind of hydrodynamic end effect considered was the development of the axial component of velocity near the upstream support. It was found that the axial component development effects did not account for the increase in heat transfer for the yawed wire. In order to investigate the possibility that deviations from the cosine law can be attributed to a difference in the end conduction losses between normal and yawed wires, precise temperature distribution measurements were taken on normal and yawed wires. The results indicated that inclined and normal wires have nearly identical end conduction losses, although the temperature distribution on an inclined wire was asymmetrical. The conclusion drawn was that the deviation from the cosine law was caused by an increase in the convection heat loss attributable to the tangential component of velocity.

Fujita and Kovasznay (1968) proposed the following relationship to represent the heat transfer from a yawed wire:

$$f(\gamma) = \cos \gamma + \varepsilon(\cos \gamma - \cos 2\gamma) \qquad (2\text{-}8)$$

and found that the relationship worked reasonably well for $\gamma < 70°$. A single value of ε was calculated by taking a weighted average over a number of angular positions.

Sandborn (1972) suggested that the most accurate evaluation of a yawed wire appeared to be a semi-graphic approach, where no specific curve fitting was attempted. When a hot wire was calibrated for mean

velocity and flow angle to the wire, the graphical representation of the calibration was a surface where the heat transfer from the wire varied with a change in mean velocity and flow angle. Therefore, the fluctuating voltage output of the wire should be a function of the fluctuation in mean velocity and flow angle. This relationship could be represented in the following manner:

$$e = \frac{\partial E}{\partial U} u + \frac{\partial E}{\partial \gamma} \frac{v}{\overline{U}} \qquad (2\text{-}9)$$

The sensitivities of the hot wire to a change in mean velocity and flow angle could be obtained graphically from the calibration surface.

Mean Velocity Vector and Reynolds Stresses

From the preceeding section it is evident that a considerable amount of disagreement exists on how the heat transfer from a wire varies with the yaw angle of the wire. The accuracy of the velocity measurements will be affected by what functional relationship is chosen to describe the heat loss from a yawed wire.

Champagne and Sleicher (1967) derived the hot wire response equations for linearized constant temperature operation. The effects of the tangential velocity component were included by using Hinze's relationship in the analysis. Assuming low intensity turbulence, the equations were applied to an X-array to determine the errors in the turbulence quantities which would arise from the assumption of normal component cooling. For the case of a wire with a length-to-diameter ratio of 200 and assuming a value of k equal to 0.20, the calculated values of u'^2/U^2 (where U is the local mean longitudinal velocity) were found to be the same by using either Hinze's relationship or the cosine law. However, the assumption of cosine law cooling could cause an error in v'^2/U^2

and w'^2/U^2 of 17 percent and an error in the Reynolds shear stresses of 8 percent.

Following the same analysis of Champagne and Sleicher, Friehe and Schwarz (1968) derived the hot wire response equations but used the authors own relationship to account for the effect of the tangential velocity component. The errors which arise from the assumption of cosine law cooling were determined for hot wires and hot films. Again, there was no error in the value of u'^2/U^2. However, for a hot film with an 1/d ratio of 20, the error in v'^2/U^2 and w'^2/U^2 was 37 percent, while the error in the shear stresses was 16 percent.

Delleur (1966) measured the flow direction sensitivity of a single hot wire and paired hot wires and found that the X-array had a higher angular sensitivity than the single wire. The author stated that single and crossed wires may be used to determine flow direction with an accuracy better than 0.05° as long as the turbulence intensity is below 12 percent. The accuracy decreased with an increase in turbulence intensity.

Fujita and Kovasznay (1968) used a single rotated hot wire anemometer to obtain values of u'^2, v'^2, and $\overline{uv}$. A single wire oriented normal to its sensor prong supports was rotated in a plane parallel to the surface of the bounding flow. The single wire had a distinct advantage over an X-array since the matching of two slightly different wires was not required. The hot wire response equations, relating the mean square of the voltage fluctuations to the values of u'^2, v'^2, and $\overline{uv}$, were derived for linearized operation. Traces of the mean voltage and the mean square of the voltage fluctuations were plotted with respect to angular position of the wire. The mean velocity direction

was determined from the trace of the mean voltage. Theoretically, only three values of the mean square voltage must be taken with the wire located at different angles to the flow. However, by measuring more than three values and applying the method of least squares, the accuracy of the system was improved.

The system was checked by comparing the results of measurements of $\overline{uv}$ in a fully developed turbulent pipe flow with the same values calculated from the measured pressure drop along the pipes. The agreement between the two values of $\overline{uv}$ was good.

Bissonnette and Mellor (1974) applied the technique used by Fujita and Kovasznay to obtain measurements of the mean velocity vector and six Reynolds stresses in an axisymmetric turbulent boundary layer with a sudden circumferential strain. There were two main differences between the method developed by Bissonnette and Mellor and the method used by Fujita and Kovasznay. First, in order to obtain the six velocity correlations, Bissonnette and Mellor rotated a wire, slanted at 45° to the sensor prong supports, about the axis of the probe support which was aligned normal to the flow. By using a 45° slanted wire, the hot wire response equations related the mean square value of the voltage fluctuations to the six velocity correlations. The second difference was that Bissonnette and Mellor used Hinze's relationship to account for the heat loss from a yawed wire.

The authors were unable to take accurate and consistent measurements of the six velocity correlations using the single slanted wire. Therefore, a single normal wire was used to obtain three of the velocity correlations and then these values were used in the hot wire response equations derived for the slanted wire to determine the remaining

velocity correlations. Much better accuracy and consistency was achieved by using this latter technique, however, it required two sets of measurements.

To check the accuracy of this measurement technique, measurements of the six velocity correlations were taken in a fully developed turbulent pipe flow. The measured value of $\overline{uv}$ showed good agreement (better than 2 percent to 3 percent) with the value determined from the pressure drop along the pipe. The measured values of u', v', and w' compared well with the values obtained by other investigators. Finally, the stress components $\overline{uw}$ and $\overline{vw}$, theoretically zero, were measured to be less than 5 percent of the local u'^2.

As was mentioned earlier, Bissonnette and Mellor obtained measurements in an axisymmetric turbulent boundary layer with a sudden circumferential strain. This flow condition was produced by placing a rotating cylinder in a low turbulence flow stream with the axis of the cylinder aligned with the mean flow direction. In order to take turbulence measurements in this highly skewed flow, the direction of the mean velocity was found, and then the six velocity correlations were calculated in a reference frame aligned with the mean velocity vector. The velocity correlation tensor was then rotated to a reference frame aligned with the axis of the cylinder.

Pierce and Ezekwe (1976) also took measurements of the six components of the velocity correlation in a three-dimensional turbulent boundary layer. A comparison was made between two hot-wire anemometer techniques used to measure the turbulent components. One technique used a single rotated wire and followed the procedure and analysis of Bissonnette and Mellor. The other technique used a combination of X-array traverses to measure the turbulent components following a

procedure developed by Gessner (1964). Four traverses of fixed X-arrays were made through the boundary layer orienting the probe with respect to the local boundary layer velocity vector. Single traverses were made with a horizontal X-array, a vertical X-array, and two traverses were made with a slant X-array (an array contained in a plane along the local flow direction and at 45° with the physical floor). The local mean flow vector was measured by using a single wire which, in this case, was the lower wire of the horizontal X-array.

The comparison of the measurements obtained by the two methods was good, although there was more scatter in the results obtained with the rotating hot wire. An attempt was made to measure all six turbulent components by rotating a single slanted wire. However, considerably more scatter was found in these measurements which was similar to the results obtained by Bissonnette and Mellor.

In conclusion, an excellent review of the hot-wire anemometry techniques used by earlier investigators to measure mean and turbulent velocities was given in a paper by Cooper and Tulin (1955).

Chapter III

DATA ACQUISITION AND ANALYSIS

Pipe Test Facility

One set of velocity measurements was obtained in a pipe facility located in the Fluid Dynamics and Diffusion Laboratory of Colorado State University, Fort Collins, Colorado. A schematic of the pipe showing the coordinate system is presented in Figure 2. Air passes through a 1.52 hp axial flow blower, enters a contraction, and is blown through the pipe. The straight section of the pipe is 12.2 m long and has a constant diameter of 14.6 cm. The inside of the pipe has been painted except for a section 0.33 m long at the end of the pipe where a smooth inside surface exists. Four pressure taps are located within 2 m of the end of the pipe.

The Reynolds number of the pipe, which is based on the pipe diameter, for all measurements is 7×10^4. Mean velocity profiles have not been taken over the length of the pipe to determine the location where the flow becomes fully developed turbulent. However, the length of the pipe (83.5 pipe diameters) should provide a fully developed turbulent flow over at least the last 3 m of the pipe. A mean velocity profile has been taken at a location 7.62 cm upstream from the end of the pipe, and the flow is found to be fully developed turbulent. All measurements are taken at this location in the pipe.

Wind Tunnel Facility

Two sets of velocity measurements have been taken in the industrial aerodynamics wind tunnel which is located in the Fluid Dynamics and Diffusion Laboratory. A schematic of the wind tunnel is shown in Figure 3. The tunnel is a closed-circuit facility which is powered by a

75 hp single-speed induction motor. Controlling the speed in the wind tunnel is a 16-blade variable-pitch axial fan. The square cross section of the tunnel is 3.3 m^2, and the length of the test section is 18.3 m. The contraction ratio at the entrance of the test section is 4:1. The mean velocity in the test section can be adjusted continuously from 1.0 m/s to 24.4 m/s. The ceiling of the last 7.3 m of the test section is adjustable to maintain a zero pressure gradient along the tunnel.

In order to generate a thick turbulent boundary layer, a long test section was used in conjunction with spires, a barrier, and roughness elements on the floor of the wind tunnel. Peterka and Cermak (1974) discussed the use of these methods to artificially develop a boundary layer. The spires which were used in this work were developed by Peterka and Cermak (1974). The dimensions of the spires and their location in the wind tunnel are shown in Figures 4 and 5, respectively. The location of the barrier was 0.61 m downstream of the spires, and it had dimensions 0.089 m x 0.191 m. The roughness elements began at a distance 1.22 m downstream of the spires and extended the length of the test section. The model which was used in conjunction with one set of velocity measurements was located 8.3 spires heights downstream of the spires, so at this location a boundary layer in reasonable equilibrium existed. The condition used to indicate the development of an equilibrium boundary layer was that any changes in flow characteristics occurring in the downstream direction were less than the resolution of the measurement system.

Two different boundary layers were used in this study. The spires and barrier were used to generate both of the boundary layers. However, a change in the roughness elements was made to develop two distinct

boundary layers. Boundary layer 1 was developed over a smooth floor, while boundary layer 2 was formed by using cubes spaced uniformly on the floor of the wind tunnel. The dimensions of the cubes and their location in the wind tunnel are shown in Figure 6. Akins and Cermak (1976) made detailed measurements of these two boundary layers at a location 16.7 m downstream of the spires. The coordinate system which is used for these measurements is shown in Figure 5. It is important to point out that no roughness elements are located within a circle having a radius, d_r, from the origin of the coordinate system. The magnitude of the radius, d_r, for boundary layer 2 is given in Figure 6. Each boundary layer had a thickness of 1.27 m. The power-law exponent of boundary layer 1 was 0.12, and its roughness height was 12.2 μm. Boundary layer 2 had a power-law exponent of 0.27 and a roughness height of 2.79 mm. No appreciable change occurred in the mean velocity profiles in the lateral or longitudinal direction from the origin of the coordinate system. A more detailed discussion of the nature of these boundary layers is included in the work by Akins and Cermak (1976).

A schematic of the power plant model which is used in this work is shown in Figure 7. A picture of the model is shown in Figure 8. This model has been used in an ongoing building study at Colorado State University, and it has been chosen because an extensive amount of velocity data has been taken in the wake of the model. This velocity data consists of mean velocity defects and turbulence intensity excesses. The three buildings are constructed out of Lucite, and the elevated terrain is made from styrofoam. The entire model was mounted on a 0.635 cm thick square piece of Masonite which was then fastened to the floor of the wind tunnel. This model was only tested in boundary layer

1. The coordinate system is located on the floor of the wind tunnel, and its orientation with respect to the model is shown in Figure 7. The height, H, is 11.28 cm, and all longitudinal, lateral, and vertical distances have been normalized by H.

Velocity Measurements

A mechanical traverse with a travel of 1.3 m was used to remotely position the transducers. The position of the transducer was measured remotely to within a resolution of $\pm$ 3.0 x 10^{-4} m using a potentiometer. The traverse operated only in one direction; however, it could be moved manually to obtain measurements at different locations.

The longitudinal mean velocity profile in the pipe was taken by using three different methods. One velocity profile was taken by using a pitot-static tube connected to a MKS Baratron Pressure Meter (Type 77). The effect of turbulence intensity on the velocity measurements using the pitot-static tube was negligible. The maximum longitudinal turbulence intensity was approximately 11 percent. This turbulence intensity would cause an error in the velocity measurement of less than 1 percent of the longitudinal mean velocity. The other profiles were taken by two hot-film anemometer systems.

Profiles of the mean longitudinal velocity and the longitudinal velocity fluctuations were taken with a single hot film oriented normal to the pipe longitudinal axis. A Thermo-Systems, Inc., Model 1050, constant temperature anemometer unit was used with a TSI-10 platinum-coated quartz cylindrical film. This unit was operated without linearization or filtering. The film had a sensing diameter of 25 μm and a sensing length of 510 μm. The frequency response of the anemometer unit was calculated using the manufacturer's specifications (in response to a

square-wave test signal), and the unit was found to have a frequency response (down 3dB) up to 16 KHz. This frequency response was adequate for the measurements taken in the two boundary layers of the wind tunnel, since Akins and Cermak (1976) found that no significant turbulent kinetic energy existed in the flow at a frequency of 2000 Hz. The longitudinal turbulence intensity measurements in the pipe were compared with similar measurements obtained by Laufer (1954) to determine if the frequency response of this anemometer unit was adequate.

The hot film was calibrated using a Thermo-Systems, Inc., Model 1125, calibrator and the MKS Baratron Pressure Meter. This calibrator supplied a low turbulence intensity air flow and was also calibrated by using the pitot-static tube and the same pressure meter. The calibrator was accurate to within 1 percent of the velocity measured by the pitot-static tube.

The calibration data was fit to a variable exponent form of King's Law:

$$E^2 = A + B\,U^C \tag{3-1}$$

by using a least squares technique. The local turbulence intensity was calculated by using the following equation:

$$\frac{u'}{\overline{U}} = \frac{2EE_{rms}}{cBU^C} . \tag{3-2}$$

The mean voltage of the anemometer bridge output was obtained using a Thermo-Systems, Inc., Model 1047, averaging circuit. True root-mean-square voltages were measured by averaging the d-c output of a DISA, Model 55D35, rms voltmeter with the averaging circuit. A stable and

repeatable reading of the mean and rms voltages was obtained by using a one minute averaging time.

Since the calibration of the hot film was not conducted in the test facilities, and no system was available to control the fluid temperature in the test facilities, a correction, accounting for the difference in temperature between the calibration and test locations, must be made. This correction followed the method given by Bearman (1971) and required that two conditions must be met to ensure accurate results in the velocity measurements. The temperature differences had to be small (less than approximately 12°C), and the mean velocity had to be greater than 0.9 to 1.5 m/sec. These conditions were met for all the tests performed.

The hot film was always calibrated before and after the velocity measurements were taken. In this way the hot film calibration obtained before testing could be verified. The measurement data was reduced using the calibrations obtained before and after testing, and there was always good agreement between the two sets of data. The difference in the mean and rms velocity between the two sets of data was never greater than 1.6 percent and 1.2 percent, respectively. This measurement procedure also served as a means of verifying the temperature correction that was used in the data reduction.

Rotated Hot-Film Anemometer

Introduction

A rotated hot-film anemometer system, designed by J. A. Peterka, was used to obtain the mean velocity profile and the six Reynolds stresses in the pipe and all the velocity measurements in the wind tunnel. This system was used by Hansen and Cermak (1975) to measure the location and strength of a weak vortex in the wake of an obstacle

submerged in a thick turbulent boundary layer. Emphasis was placed on a system which could measure weak cross-flow components with a high degree of resolution. When the system was originally designed, the analysis was carried through to a point where, theoretically, the mean velocity vector and Reynolds stress components could be measured. Hansen and Cermak found that in a low turbulence flow (longitudinal turbulence intensity less than 12 percent) the system was capable of detecting a cross flow having a magnitude which was one percent of the local longitudinal velocity. After the system was designed, measurements of the Reynolds stress components were taken in a fully developed turbulent pipe flow. Accurate and consistent measurements of the Reynolds stresses could not be obtained. The remaining part of this section will discuss the development of the rotated hot-film anemometer system so it could be used to obtain accurate measurements of the Reynolds stresses in a three-dimensional turbulent flow.

Principle of Operation

This rotated hot-film anemometer system uses the same principle and analysis which is used in any other yawed sensor. The hot film is yawed to the flow and then is rotated about its probe support axis varying the angle of incidence between the mean flow and the sensor. By using simple geometrical considerations, information about the magnitude and direction of the mean velocity vector can be extracted from the measurements. Theoretically, the sensor would only have to be rotated to three different angles to measure the mean velocity vector. However, by rotating the film to more than three angles and applying a least-squares technique, the "best fit" solution to the equation for the mean velocity components can be obtained. The three mean velocity components can then

be used in the hot-film anemometer response equation for turbulent flow to obtain the values of the six components of velocity correlation. Here again, six different angular positions of the film would be sufficient to calculate the velocity correlations. However, the "best fit" solution to the equation can be obtained by rotating the sensor to more than six angular positions and applying the method of least-squares. This system has an advantage over other anemometer techniques since the direction of the mean velocity vector in a three-dimensional turbulent flow does not have to be known precisely before measurements of the turbulence characteristics of the flow can be taken. In addition, only one set of measurements has to be taken at each measurement location considerable reducing the time which is required to obtain the measurements.

A picture of the rotated hot-film probe support is shown in Figure 9. A schematic showing the probe coordinate system and other useful notation is shown in Figure 10. An 0.46 m long Thermo-Systems, Inc., probe support is mounted to a frame. A TSI-10 hot film, which is yawed at 45° to the sensor end supports, is rotated remotely about the axis of the probe support by a d-c motor. The angular position of the film is monitored remotely by a potentiometer. The entire frame is attached to the mechanical traverse and is oriented at small angles of pitch and yaw to the mean longitudinal velocity of the flow. These angles of pitch and yaw are important in obtaining measurements of the Reynolds stresses and will be discussed in more detail in a latter section. The probe support is then rotated to the desired number of angular positions. Each angular position (ψ) is recorded along with the mean and rms voltages which are averaged for one minute using the averaging unit.

The hot film is calibrated by positioning the frame and probe support on a calibration stand to which an angular scale has been attached. A picture showing the calibration setup is presented in Figure 11. The film is calibrated over a range of velocities and a range of angles from 20° to 90°, i.e. when the flow is normal to the film. This data is fit to a surface of the form:

$$E^2 = A + BU^C f(\theta) \qquad (3\text{-}3)$$

where $f(\theta)$ is given by $f(\theta) = 1.0 + A_1 \theta + A_2\theta^2 + A_3\theta^3$. The selection of this functional form is discussed in a later section. The six constants are determined by using a least squares method and an iterative technique.

The three components of mean velocity are calculated first by using the mean voltage data which is obtained at each angular position of the probe support. The details of this analysis are given in Appendix A. Initially, a guess of the values of the three mean velocity components ($\overline{U}$, $\overline{V}$, and $\overline{W}$) is made. These values of $\overline{U}$, $\overline{V}$, and $\overline{W}$ are given in relation to a coordinate system where $\overline{U}$ coincides with the longitudinal axis of the probe support, and $\overline{V}$ and $\overline{W}$ form an orthogonal set. By using simple geometrical considerations, these three mean velocity components along with the angular position (ψ) and the angle ϕ can then be used to determine the angle of incidence (θ) between the mean velocity vector and the film at each angular position of the film. Now, the least squares technique is applied to the equation for the mean velocities, and then Newton's iterative method is applied to alter the initial guess of the mean velocity components. This process is continued until the three mean velocity components do not vary more than a specified minimum. The values of the three mean velocity components are now specified in the probe coordinate system.

Once the three components of mean velocity have been calculated, the hot-film anemometer response equations for turbulent flow can be derived. The details of this analysis are given in Appendix B. The analysis follows the usual procedure in the sense that by operating on equation (3-3) the mean square of the voltage fluctuations is found to be a function of the three components of velocity (U, V, and W) and the angles ψ and ϕ. By expanding this relationship in a Taylor series about the three components of mean velocity, an equation relating the mean square of the voltage fluctuations to the six components of velocity correlation can be derived. The least squares technique is applied to the resulting equation, and by using the values of the three mean velocity components and the mean square voltages which are obtained at different angles of incidence (θ) of the film, the six velocity correlations can be calculated.

A simple vector and tensor rotation is required to rotate the mean velocity components and velocity correlations from the probe coordinate system to the desired reference coordinate system. This rotation was performed differently for each of the three test conditions in this thesis. For measurements in the pipe, the angles of rotation were determined for each measurement location such that the values of $\overline{V}$ and $\overline{W}$ were zero in a reference coordinate system aligned with the longitudinal axis of the pipe. For measurements taken in the wind tunnel in boundary layer 2, the rotation angles were calculated such that the values of $\overline{V}$ and $\overline{W}$ were zero in the reference coordinate system when averaged over a number of measurement locations at the outer portion of the boundary layer. These angles of rotation were then used for the remainder of the measurement locations in the boundary layer. This

procedure was followed to account for the fact that small, but significant, components of cross flow might exist in the lower portion of the boundary layer. For measurements taken in the wake of the power plant model, the rotation angles were determined in the following manner. A set of measurements were taken with and without the model. The angles of rotation were then calculated following the previous procedure for all measurements taken in the undisturbed boundary layer (the values of $\overline{V}$ and $\overline{W}$ were zero in the reference coordinate system when averaged over all the measurements in the undisturbed boundary layer). These same rotation angles were used for the measurements taken in the wake of the model. Since it was necessary to move the mechanical traverse for each vertical profile, a different set of rotation angles was calculated for each profile. By calculating the angles of rotation in this manner, the measurements taken in the wake of the model will represent only the effect that the model had on the boundary layer flow. This procedure provided an additional check on errors occurring in the measurements due to slight misalignments in the probe support.

Directional Sensitivities of the Hot Film

From Chapter II, it was obvious that a considerable amount of disagreement existed on which relationship should be used to account for the directional properties of a yawed sensor. A cubic was chosen in this measurement technique to describe this relationship.

A typical rotated hot-film calibration is shown in Figure 12. To evaluate the accuracy of this function, a set of calibration data was fit to equation (3-1). A typical graph indicating the accuracy of this particular $f(\theta)$ for a range of yaw angles from 20° to 90° is shown in Figure 13. This graph was plotted for only one velocity, however, the

same kind of accuracy was realized for a range of velocities from 6 m/sec to 17 m/sec. Three other functional relationships for $f(\theta)$ (the cosine law, Hinze's relationship, and the relationship proposed by Friehe and Schwarz (1969)) were also evaluated with the calibration data. The cosine law fit the data well for angles greater than 30°, while the relationships of Hinze and Friehe and Schwarz fit the data reasonably well for all angles greater than 20°. The cubic gave the best fit to the calibration data over the entire range of angles.

Error Analysis

In order to determine the resolution of the measurements taken with the rotated hot-film anemometer system, a Monte Carlo simulation technique was used. The simulation technique was conducted in the following manner: Basically, the rotated hot-film data reduction program was used as a "black box". Random errors were applied to sets of generated data which, in turn, were supplied to the reduction program. A list of solutions was calculated by the reduction program, and from this list the standard deviation of the different measurement quantities could be calculated and used as a measure of the resolution of the system.

In acquiring the data which is used in the data reduction program, there are five measurement values which are susceptible to random errors, and an estimation of the standard deviation of these random errors for each measurement value is calculated. By assuming values for the three mean velocity components and six velocity correlations for a particular flow condition and by supplying rotation angles of the probe support (ψ) along with the angle ϕ, the rotated hot-film reduction program can be used in reverse to generate values for the mean voltages and the rms values of the fluctuating voltages. These generated values are

considered to be the "exact" ones in order to obtain the desired measurements of the mean velocity components and velocity correlations. By using the standard deviation of the random errors in the five measurement quantities, random errors can be distributed to all the so-called "exact" data values, and then the data reduction program is used to calculate the desired measurement quantities. Again, another set of random errors is distributed to the "exact" data values, and another set of measurement quantities is calculated. This process is repeated a significant number of times (50 iterations have been found to be adequate), and the standard deviation in the desired measurement quantities is then calculated. The details of the Monte Carlo simulation technique are given in Appendix C.

The results of this Monte Carlo technique are shown in Table 2. These results are presented for two cases: one when the longitudinal turbulence intensity of the flow is 6 percent and another when the longitudinal turbulence intensity is 18 percent.

The standard deviations in the mean velocity components and mean swirl velocity, $\overline{U}_s = [\overline{V}^2 + \overline{W}^2]^{1/2}$, are given as the percent of the local $\overline{U}$. The resolution in these components is always better than 2.0 percent of the local mean longitudinal velocity. There is little difference between the resolutions for the low and high turbulence cases, and this is understandable since there is only a small difference in the standard deviation of the mean voltages for the low and high turbulence cases (Table 1). It is interesting to note that for the low turbulence intensity case, the resolution in the mean swirl velocity is approximately one percent of the local mean longitudinal velocity. This is approximately the value determined by Hansen and Cermak (1975). The resolution in the values of β_1 and β_2 (Figure 10) for the low turbulence

intensity case are 0.50° and 0.61°, respectively. Hansen and Cermak (1975) have obtained experimental uncertainty values of 0.39° and 0.63° for β_1 and β_2, respectively. The resolution in these same measurement quantities for the high turbulence intensity case is less than the resolution given by Hansen and Cermak (1975). This is due to the small difference in the standard deviation of the mean voltages for the low and high turbulence cases. At this time it is not known why there is not a significantly greater standard deviation in the mean voltages for the high turbulence case.

The standard deviations in the Reynolds normal stresses are given as a percent of the local u'. The resolutions in u', v', and w' for the low turbulence intensity case are 5.85 percent, 10.15 percent, and 11.26 percent, respectively. Even better resolutions exist for the high turbulence case. It should be kept in mind that the standard deviations for the low turbulence case are significantly greater than the ones for the high turbulence case since the local u' is significantly smaller for the low turbulence case compared to the high turbulence case. The standard deviation given in m/sec is significantly greater for the high turbulence case compared with the low turbulence case.

The standard deviations in the Reynolds shear stresses are given as a percent of the local u'^2. The resolutions in $\overline{uv}$, $\overline{uw}$, and $\overline{vw}$ for the low turbulence intensity case are 4.85 percent, 4.59 percent, and 2.89 percent, respectively. Slightly less accuracy is realized for the high turbulence case compared to the low turbulence case. This is exactly opposite to the results of the Reynolds normal stresses, thus indicating that the high turbulence intensity affects the resolution of the Reynolds shear stresses more than the Reynolds normal stresses. These generated

resolutions of the Reynolds stress components are compared with the experimental scatter in these measurement quanitites in Chapter IV.

The linearized analysis which is used in deriving the hot-film anemometer response equations for turbulent flow is not valid for very high turbulence intensity flows. Hinze (1959) stated that errors in the measurement of turbulent characteristics of 10 to 20 percent could be realized if the longitudinal turbulence intensity of the flow was as high as 20 to 25 percent. If velocity measurements are taken in regions of separated flow with a hot-film anomometer, the errors in these measurements would be quite large due to the high turbulence intensities and reverse flows which occur in these regions.

Measurement Procedure

The principle of operation of this rotated hot-film anemometer system was discussed in detail earlier. A significant amount of effort was conducted in this work to determine whether or not an optimum solution in regards to the accuracy and resolution of the measurements was possible by taking data in a prescribed manner.

As has been explained earlier, mean voltages and the rms values of the voltage fluctuations are measured at different angular positions of the probe support. Typical graphs of the angular variation in mean voltages and rms voltages are presented in Figures 14 and 15, respectively. It should be mentioned here that the "generated" data given in the figures is the so-called "exact" data which is used in the Monte Carlo technique. The other data points are the actual values which are acquired in the turbulent flow. In other words, the "generated" data gives the "best fit" solution through the actual data. The mean voltage curve is symmetrical with respect to a particular value of ψ, however,

the rms voltage curve is not symmetrical. For this reason, voltages have been taken over a full range of ψ values of 360° to ensure that all the significant characteristics of the voltage curves are included when acquiring the data.

The Monte Carlo simulation technique has also been used to determine if there is an optimum number of angular positions (ψ), such that the accuracy in the solutions is not improved by acquiring data at more angular positions. The results of this study are presented in Figures 16 and 17, respectively. The number of angular positions has to be greater than six for the calculation of the six Reynolds stresses, and twelve appears to be an optimum number.

As it turns out, the angles at which the probe support is offset to the assumed mean velocity vector are extremely important in obtaining a solution for the six Reynolds stress components. The Monte Carlo technique has been used to determine the resolution in the velocity components of this measurement system when the probe support is aligned with the mean velocity vector. In this position the angle of incidence (θ) would be approximately 45° for every angular position of the probe support (ψ). When applying the Monte Carlo technique with the probe support in this position, no mean cross-flow velocity components exist. The resolution in the three mean velocity components is not significantly affected. However, there is a significant effect in the resolution of the six velocity correlations, in fact, a reasonable solution could not be obtained. The reason for this inability to obtain a solution for the six velocity correlations when the probe support is oriented in such a manner has not been determined.

The Monte Carlo technique has also been used to determine if there are optimum angles at which the probe support can be offset from the

assumed mean flow direction to acquire the maximum resolution in the desired solutions. It should be mentioned here that these offset angles have to be restricted to a range of about 20°. The desired angle of incidence (θ) was restricted to the range of 20°-75°. If the value of θ becomes much smaller than 20°, the film will be subjected to probe-tip interference effects. In a highly turbulent flow the instantaneous velocity vector may vary by several degrees from the mean velocity vector, and therefore, in order to allow some leeway, it is necessary to keep the mean θ angle greater than 20°. If the angle θ becomes too close to 90°, i.e. the mean velocity is normal to the film, the instantaneous value of θ could possibly become greater than 90°, and the sensor would be incapable of perceiving on which side of 90° the instantaneous velocity vector is directed. To alleviate this problem, the angle θ was restricted to angles significantly less than 90°. The Monte Carlo technique has also been applied to cases where voltage data has been generated where a few angles of θ are between 75° and 80°. The results showed that two slightly different solutions for the mean velocity components existed. One solution was the correct one where the particular values of θ were between 75° and 80°. However, by using different initial guesses for the three mean velocity components, a second solution was obtained where these particular values of θ lie between 110° and 115°. This same procedure was applied to angles of incidence of 75° and less, but two different solutions could not be obtained. Therefore, the maximum value of θ was restricted to 75°.

Now, after stating the restrictions which were placed on the angles of yaw and pitch of the probe support, the results of the Monte Carlo technique show that different offset angles do not significantly improve

the resolution of the mean velocity components (Figure 18). However, a definite improvement in the resolution of the six velocity correlations exists when the angles of yaw and pitch are the largest. This improvement in the resolution is shown in Figure 19. The standard deviations of some velocity correlations are not shown on the graph in Figure 19. These values are much larger than the scale which is used on the graph. This graph also shows how the scatter in the solution of the velocity correlations increases as the offset angles approach zero. For the work conducted in this thesis, the angles of yaw and pitch of the probe support were always kept between 15° and 20°.

It is important to mention here that an incorrect rotation of the solutions from the probe coordinate system to the desired reference coordinate system can significantly effect the results of the velocity correlations. Due to the orientation of the probe coordinate system, the solutions for the mean and turbulent velocity components first have to be rotated around the y'-axis (Figure 10) and then have to be rotated around the z' axis in order for the probe coordinate system to coincide with the reference coordinate system. Since the y' axis is contained in the x-y plane, the first rotation about the y' axis moves the z' axis through the angle Φ_1 at which point the z' axis and z axis coincide. The x' axis is now contained in the x-y plane, and the second rotation about the z' axis (or z axis) moves the y' axis and x' axis through the angle Φ_2 at which point the two coordinate systems coincide. If, however, the rotation is made around the z' axis first and then around the y' axis, the probe coordinate system will not coincide with the reference coordinate system and will be out of alignment by a small angle. Slight differences occur in the solutions of the mean velocity components when

using either rotation procedure. However, since certain velocity correlations are extremely small quantities, a significant difference in these values (as much as 30 percent in $\overline{uv}$) is evident when using one rotation procedure instead of the other.

Chapter IV

RESULTS AND DISCUSSION

The results of the velocity measurements which have been taken in a fully developed turbulent pipe flow and in the wind tunnel are presented in this chapter. As explained previously, velocity measurements in the pipe flow are compared with predictions which are based on the measured pressure drop in the pipe and data taken by other investigators. One set of velocity measurements was obtained for a vertical profile in a particular boundary layer in the wind tunnel and was compared with similar measurements using conventional X-wire techniques taken by other investigators. Finally, velocity measurements were taken in the wake of a power plant model immersed in a turbulent boundary layer to demonstrate the capability of this measurement system.

Pipe Test Measurements

The mean velocity profile of the pipe is shown in Figure 20. Good agreement exists among the three different methods which have been used to take these measurements, thus verifying the mean velocity measurements taken with the rotated hot-film anemometer system. A blockage effect was observed when the hot-film anemometer probes and pitot tube were mounted in the pipe. The turbulent velocity measurements were significantly affected within a region where Y'/R is less than 0.2 due to this blockage effect. Accordingly, mean and turbulent velocity measurements obtained in this region with the hot-film anemometer probes were not included in the pipe test results. The blockage effect caused by the pitot tube was not as pronounced, and since only mean velocity measurements were taken with the pitot tube, the measurements taken within this blockage region are included in Figure 20. No blockage corrections were applied to these measurements.

From the theory of fully developed turbulent pipe flow, the friction velocity is given by

$$u_\tau^2 = -\frac{R}{2}\frac{1}{\rho}\frac{dP}{dx} \tag{4-1}$$

and the Reynolds shear stress, except very close to the wall, is

$$\overline{uv} = u_\tau^2 \, Y/R \tag{4-2}$$

where R is the radius of the pipe and P is the static pressure. The axial pressure gradient in the last 2 m of the pipe is linear, and by using this measurement in conjunction with equations (4-1) and (4-2), the friction velocity and Reynolds shear stress can be calculated.

In Figure 21, the measurements of $\overline{uv}$ taken with the rotated hot-film anemometer system are compared with the values which are obtained from the measured pressure gradient in the pipe. The measurements compare well in the center region of the pipe up to the location where the blockage effect becomes significant. The difference between the values of $\overline{uv}$ lies within the resolution of the $\overline{uv}$ component given by the Monte Carlo technique. The measurement value of $\overline{uv}$ where Y'/R is approximately 0.2 still shows some slight effect due to the blockage of the probe. Corrections accounting for the blockage effect have been applied to the measurements of the shear stress within the region where the probe blockage becomes significant, and the corrected shear stress measurements compare well with the shear stress predicted from the measured pressure gradient in the pipe. The difference in these measurements always fell within the resolution of the $\overline{uv}$ component given by the Monte Carlo technique. However, these blockage corrections are as large as 60 percent near the pipe wall, and considering the

approximations which are used in these corrections, the reliability of these corrected shear stress measurements is highly questionable. Therefore, the corrected shear stress measurements taken within this region are omitted.

The results of the three components of the velocity fluctuations are shown in Figures 22 and 23. The u' component is compared with the results of Laufer (1954) and data which has been obtained in the pipe with the use of a single normal hot film. The results show that there is excellent agreement among the different measurements of the u' component. However, the v' component is larger than the values given by Laufer. Similar results can be seen in the w' component, although the difference between the measurements is not as large as the difference seen in the v' component. The values of the remaining shear stress components, $\overline{uw}$ and $\overline{vw}$, theoretically zero, are all less than 18 percent of the local u'^2. This is significantly larger than the resolution given for these components in Chapter III.

The results of the measurements taken in the pipe were encouraging. The effect of probe blockage limited the usefulness of this measurement system in obtaining velocity measurements near the wall of this particular pipe. This problem has to be alleviated if measurements near the pipe wall are to be obtained. Although the measurements of v' and w' show the same trend as the data of Laufer, the reason why the measurements of these turbulent components in this pipe flow are larger than the data of Laufer has not been resolved at this time. It was mentioned before that the inside of the pipe was coated with paint up to a point within 0.38 m of the end of the pipe, which was observed

to significantly roughen the surface. It is not known precisely what effect this nonuniform roughness has on the turbulence characteristics of the pipe flow.

Instead of redesigning the probe in this rotated hot-film anemometer so that probe blockage effects would not interfere with the velocity measurements near the pipe wall and obtaining more extensive measurements to determine if there were any peculiarities in the turbulent flow in this particular pipe due to the nonuniform roughness along the pipe wall, it was decided that a more beneficial approach would be to take similar measurements in the wind tunnel. Akins and Cermak (1976) measured the turbulence characteristics of several boundary layers in the wind tunnel using X-wire techniques, so this data could be used as an additional check on the rotated hot-film measurement system.

Wind Tunnel Measurements

Measurements in Boundary Layer 2

The current rotated hot-film data are compared to the velocity measurements taken by Akins and Cermak in boundary layer 2 (as named in that reference) in Figures 24-30. Figure 24 shows the excellent agreement in the measurement of the mean velocity profile.

In Figure 25a, the measurements of the u' component taken with the rotated hot film are slightly smaller than the values of Akins and Cermak. One would expect this to be the case, since Akins and Cermak's measurements have been taken with a single normal hot film. This film would be sensitive to the u' component, but also to one of the cross components of turbulent fluctuating velocities. Hinze (1959) suggested an analysis which could be used to estimate the size of the error in the

measurement of the u' component taken with a single normal sensor due to the cross components of turbulent fluctuating velocities. The presence of these cross components in a highly turbulent flow would cause the measurement of the u' component to be larger than the true value of u'. A higher turbulence intensity of the flow would increase the error in the measurement of the u' component. Hinze estimated the size of this error for an isotropic turbulent flow. In Figure 25b Hinze's correction has been applied to the measurements taken by Akins and Cermak. The agreement between the measurements taken with the rotated hot-film anomometer and the corrected data of Akins and Cermak is excellent within the highly turbulent region of the flow between $Z/\delta = 0.06$ and $Z/\delta = 0.2$. Less agreement is evident between the two sets of data at the two measurement positions which are less than $Z/\delta = 0.06$. These positions are located in a region which is within and just above the roughness elements where the location of the probe tips in relation to individual roughness elements may alter the results. Since the measurements were taken near the center of a circle where no roughness elements were located, a slight curvature of the mean velocity vectors toward the open area could be expected in this region. The orientation of the probe tips in relation to this curvature in the mean velocity vector may alter the results. The agreement between the two sets of data at all measurement locations greater than $Z/\delta = 0.2$ is always better than 6 percent. Figure 25a also shows that there is very little scatter in the measurements of the u' component taken with the rotated hot-film system. The resolution of the u' component given by the Monte Carlo technique is always less than 6 percent of the local u', which indicates there should be little scatter in these measurements.

Looking at the other components of turbulent fluctuating velocities, Figures 26 and 27 show that the measurements of v' and w' taken with the rotated hot film are significantly larger than the values taken by Akins and Cermak. It should be mentioned here that Akins and Cermak's measurements of the v' and w' components and the remaining turbulent shear stress components have been taken with an X-array using hot films and the assumption of normal component cooling. It has been stated in Chapter II that Champagne and Sleicher (1967) have analyzed the kind of errors one would expect in the measurements of the Reynolds stress components if only normal component cooling of the sensor is assumed in the hot wire response equations. Champagne and Sleicher have only analyzed cases when hot wires are used; however, Friehe and Schwarz (1968) have followed a similar analysis for cases in which hot films are used. By using this information and the information about the particular hot films Akins and Cermak have used, it is possible to calculate the corrections which should be made in the velocity correlation measurements taken by Akins and Cermak. When the above corrections have been applied, Figures 26 and 27 show there is excellent agreement, always better than 7 percent between the two sets of measurements, except for a few points within 0.08 m of the floor of the wind tunnel. There seems to be a definite trend in the measurements of v' and w' taken with the rotated hot film in this region; however, it is not certain if this is actually a characteristic of the flow which has not been sensed by the X-array. Here again, this is the region where individual roughness element effects may be important.

There is sufficient scatter in the measurement values of v' and w' in the lower portion of the boundary layer to make possible an evaluation

of the Monte Carlo technique. The dashed line shown in Figures 26 and 27 is drawn through the average value of the measurement quantities between Z/δ of 0.1 and 0.3. The solid lines on both sides of the dashed line indicate the resolution given by the Monte Carlo technique. The scatter in the measurement values falls within the resolution limits, which indicate that the Monte Carlo technique is accurately predicting the resolution in the v' and w' components. It should also be mentioned here that all of the corrected measurement values of Akins and Cermak in this lower region of the boundary layer lie within the resolution limits of the rotated hot-film anemometer.

The comparison of the measurements of $\overline{uw}$ is shown in Figure 28. Here again, a correction has been made to the measurements taken by Akins and Cermak. There is good agreement between the two sets of measurements except near the wind tunnel floor where individual roughness element effects may be important. To evaluate the resolution in the $\overline{uw}$ component given by the Monte Carlo technique, a constant shear stress value has been selected for a region less than $Z/\delta = 0.2$. This value is an average of the measurement values in this region and is indicated by the dashed line. The resolution limits are again given by the solid lines. Except for the one measurement value at $Z/\delta = 0.06$, the values of $\overline{uw}$ lie within the resolution limits given by the Monte Carlo technique. It is not known at this time if the measurement value $Z/\delta = 0.06$ is an actual representation of the shear stress profile, or if it is just a spurious data value.

The measurements of the $\overline{uv}$ component have been compared in Figure 29. The agreement between the two sets of data is good except for measurements taken within 0.13 m of the floor where individual roughness

element effects may be important. In order to evaluate the Monte Carlo technique, again, a constant value of $\overline{uv}$ has been selected for the region less than $Z/\delta = 0.2$. This value has only been selected to illustrate the resolution of this component. The measurement values of $\overline{uv}$ (except for the value at $Z/\delta = 0.06$) fall well within the resolution limits, which may indicate that the Monte Carlo technique slightly underestimates the resolution of this component. Here again, all the measurement values taken by Akins and Cermak lie within the resolution limits of the rotated hot-film anemometer.

The remaining shear stress component, $\overline{vw}$, is shown in Figure 30 along with the values of $\overline{uw}$ and $\overline{uv}$ taken with the rotated hot film. For this particular boundary layer flow, $\overline{vw}$ should be zero, and the measurement value is always less than 6 percent of the local u'^2. This is slightly higher than the resolution value of 3.33 percent of u'^2 which is predicted by the Monte Carlo technique.

Measurements in Wake of Model

All of the velocity measurements which have been taken in the wake of the power plant model and are presented in this thesis have been taken in a vertical plane which is located at a distance, $X/H = 10$, downwind from the model. This downwind position has been chosen because it lies beyond the separation bubble behind the model, thus ensuring that the hot film does not lie in a region where reverse flows occur. At this downwind location a significant mean velocity defect and turbulence intensity excess exist, which ensures that there is still a significant amount of turbulent mixing occurring between the undisturbed and disturbed flows.

The mean cross-flow velocity vector distribution in the vertical plane is shown in Figure 31. This diagram illustrates how the undisturbed flow is carried into the disturbed flow in the wake of the model. No organized vorticity can be seen at this downstream location, however, there seems to be a channeling of the mean velocity to a location to the left and below the top of building number 1. There is only a longitudinal component of the mean velocity vector in this region. If there is a significant amount of fluid flowing into this region, one would expect to see a detectable acceleration of the longitudinal mean velocity. Longitudinal mean velocity measurements taken slightly upwind and downwind from X/H = 10 may indicate there is an acceleration in the longitudinal mean velocity in this region. An indication of this acceleration appears in Figure 33 and will be discussed in a subsequent paragraph.

Figure 32 depicts vertical profiles of the longitudinal mean velocity defect in the wake of the model at different spanwise distances from the longitudinal axis of the model coordinate system. The largest velocity defect in the vertical profiles occurs at a location less than half of the height H. The vertical profile of the velocity defect on the centerline shows that the largest vertical extent of the wake occurs at this location, and that the flow has returned to its undisturbed state by 2.0 to 2.5 building heights above the top of building number 1. The profiles at lateral distances from the centerline show that the velocity defect in the wake decreases at increasing lateral distances from the centerline, except at Y/H = -0.68. Here, the velocity defect below the height H is greater than the defect occurring on the centerline, but the flow returns to its undisturbed state sooner than the flow at

the centerline. This seems reasonable looking at Figure 7 and noting the asymmetry of the model with respect to the centerline and the location where the vertical profiles have been taken.

Lateral profiles of the longitudinal mean velocity defect at different vertical positions is shown in Figure 33. This figure gives a better illustration of how the largest velocity defect does not occur at Y/H = 0, but instead occurs at Y/H = -0.68. At the two vertical locations below the height of building 1, the flow has not returned to its undisturbed state at lateral distances of Y/H = 1.58. The extent of the wake is naturally greater in the negative Y direction since the model extends farther laterally in this direction. It is also interesting to note that at increasing heights the lateral profiles of velocity defect tend to become more symmetrical with respect to the centerline. This is due to the diminishing effect the shorter buildings in the negative lateral direction have on the wake flow at increasing heights in the wake. It has been mentioned earlier that the mean flow in the wake is being channeled into a small region to the left and below the top of building 1. The lateral profile at Z/H = 0.90 indicates that an increase in mean velocity occurs at Y/H = 1.13, and this location is in the region in question. The mean velocity then decreases slightly at Y/H = 1.58. This may be an indication that an acceleration of the longitudinal mean velocity is occurring in this region. There is no indication of an increase in the longitudinal mean velocity from the lateral profile of velocity deficit at Z/H = 0.45.

Contours of the local longitudinal, lateral, and vertical turbulence intensity (in percent) are shown in Figures 34-36. The maximum longitudinal, lateral, and vertical turbulence intensities are 18.0

percent, 19.0 percent, and 18.0 percent, respectively. In the region where these maximum turbulence intensities occur, the values of the three components of turbulence intensity have approximately the same magnitude at a number of measurement locations. In a flow closer to equilibrium this may indicate that an isotropic turbulence field exists in this region. That is not the case for this flow, however, since a large turbulent shear stress exists in this region. It is not known at this time why the three components of turbulence intensity in this region are nearly equal. These values can be compared with the maximum longitudinal, lateral, and vertical turbulence intensities in this region of the flow without the model of 10.0 percent, 9.0 percent, and 7.0 percent, respectively. The contours of the longitudinal turbulence intensity show that the maximum longitudinal turbulence intensity occurs in the region where there is the largest mean velocity defect and not directly behind building 1. A greater degree of symmetry about the centerline is evident in the contours of the lateral and vertical turbulence intensities. The maximum lateral and vertical turbulence intensities occur near the centerline and at a height of less than H/2. All three graphs of the contours of turbulence intensity show that the largest vertical extent of the wake occurs at the centerline and then decreases at increasing lateral distances from the centerline. The lateral and vertical turbulence intensities decrease more rapidly from their maximum value to their undisturbed value outside the wake than does the longitudinal turbulence intensity. The contours of the longitudinal turbulence intensity indicate that the wake extends to a greater lateral distance in the negative direction, which is consistent with the mean velocity defect profiles.

The shear stress profiles of $\overline{uw}$ are shown in Figures 37a-37g. The shear stress profile without the model has been plotted with the shear stress profile with the model. By plotting the profiles in this manner, the area between the two profiles represents the increase in the shear stress in the flow which is caused by the disturbance of the model.

Figure 37a represents the shear stress profile of $\overline{uw}$ on the centerline. The maximum shear stress occurs at approximately the height H. The shear stress diminishes at increasing heights until it coincides with the shear stress in the undisturbed flow at approximately Z/H = 2.5, which indicates that the wake extends to this height. This is consistent with the vertical wake extent given by the mean velocity profiles. The maximum shear stress occurs at approximately the same location as the maximum rate of change in the vertical mean velocity profile, as expected. At increasing lateral distances in the positive direction, the maximum shear stress decreases in magnitude and occurs at decreasing heights in each profile. This is expected since the maximum rate of change in mean velocity occurs at lower heights in each vertical profile in the lateral direction. The shear stress profile at Y/H = 1.58 shows that there is very little difference between the shear stresses with and without the model, and therefore, the wake does not extend laterally much beyond this distance. The shear stress profiles in the negative lateral direction show a similar pattern to the profiles in the positive lateral direction when comparing the magnitude and location of the maximum shear stress. However, the shear stress profile for Y/H = -1.58 definitely indicates that the wake extends much farther in the negative lateral direction than the positive, which is consistent with the lateral mean velocity profiles.

These shear stress profiles of $\overline{uw}$ can also be used as a check on the precision of the measurement. The shear stress measurements taken without the model should be approximately the same for each lateral position. These lateral profiles are approximately the same. Except for a couple of measurement values, the scatter in the individual measurements of $\overline{uw}$ falls within the resolution of this component given by the Monte Carlo technique.

The shear stress profiles of $\overline{uv}$ are shown in Figures 38a-38d. Here again, the profiles have been plotted for the cases with and without the model. The shear stress profile for Z/H = 0.45 is shown in Figure 38a. The maximum shear stress in the positive lateral direction is between 1/2 and 1 building height from the centerline. This is approximately the same location as the maximum rate of change in the lateral mean velocity profile. Since the slope of the lateral mean velocity profile changes sign over the lateral extent of the wake, the value of $\overline{uv}$ should also change sign. This does not occur for the lateral profile at Z/H = 0.45, but the values of $\overline{uv}$ at Y/H equal to -0.68 and -1.58 decrease to approximately the same as the values without the model. This characteristic of the flow is more evident for the lateral profile at Z/H = 0.90 shown in Figure 38b. The values of $\overline{uv}$ become slightly negative at Y/H values of -0.68 and -1.58. Only a small shear stress exists in the lateral profile at Z/H = 1.80, and the shear stress profile at Z/H = 2.25 indicates that the wake does not extend above this height.

The precision of the measurements of $\overline{uv}$ can be evaluated by looking at the lateral profiles without the model in place. Except for a few measurement values, the scatter in the data is within the measurement resolution of the $\overline{uv}$ component.

The flow in the wake of this particular model is very complex. To obtain a better picture of the physical mechanisms which are occurring in the flow, more extensive measurements should be taken at numerous downwind locations behind the model and at farther lateral positions from the centerline. These velocity measurements taken in the wake of the model give an indication of the capability of the rotated hot-film anemometer system.

Chapter V

CONCLUSIONS AND RECOMMENDATIONS

A rotated hot-film anemometer has been developed to take sensitive measurements of the three mean velocity components and the six components of Reynolds stress in a three-dimensional turbulent flow. Several conclusions can be drawn about the capability and reliability of this measurement system.

This rotated hot-film anemometer has the advantage that the direction of the mean velocity vector in a three-dimensional turbulent flow does not have to be known precisely before measurements of the turbulence characteristics of the flow can be taken. It has the additional advantage that only one set of measurements has to be taken at each measurement location. This considerably reduces the time required to obtain this information.

For a low turbulence intensity flow ($u'/\overline{U} = 0.06$), the mean cross-flow velocity can be measured to within one percent of the local mean longitudinal velocity. The Reynolds normal stress components can be measured within 12 percent of the local u', and the Reynolds shear stress components can be measured within 5 percent of the local u'^2. Lower resolutions in these components are realized for a high turbulence intensity flow ($u'/\overline{U} = 0.18$). For very large turbulence intensity flows, the errors would increase greatly.

Velocity measurements taken in a fully developed turbulent pipe flow indicate that the anemometer is accurately measuring the mean velocity components. Accurate measurements of the shear stress component, $\overline{uv}$, have been taken in the center region of the pipe up to the location where probe blockage effects become significant. Although the

measurements of u' agree well with data taken by other investigators, the measurements of v' and w' are higher than the values obtained by others. It is not known at this time why better agreement is not obtained in the latter measurement quantities. Local excessive pipe roughness may have disturbed the flow.

Mean velocity and Reynolds stress measurements taken in a turbulent boundary layer in the wind tunnel show good agreement with the same quantities taken by other investigators. In regions of high turbulence intensity ($u'/\overline{U} > 0.16$) there is less agreement in the Reynolds stress measurements which may have been caused by the orientation of the probe tips in relation to the surface mounted roughness elements. The set of measurements taken in the wake of a model structure immersed in a turbulent boundary layer in the wind tunnel gave an indication of the capability of this rotated hot-film anemometer for analyzing three-dimensional flows.

A number of recommendations for further work with this rotated hot-film anemometer can be made. Additional measurements of the Reynolds stress components should be taken in a fully developed turbulent pipe flow where probe blockage effects do not interfere with measurements taken near the pipe wall and the inner wall surface is smooth and uniform. A research effort should be conducted to determine if the measurement corrections which are suggested by Champagne and Sleicher (1967) and by Friehe and Schwarz (1968) are valid. Additional studies should be conducted to determine if the system could be used to obtain accurate Reynolds stress measurements with the probe support aligned with the mean velocity vector. Additional studies of the angle response of the

sensor are necessary to select a universal function. The rotated hot-film anemometer system needs additional validation experiments with a range of parameters.

If the rotated hot-film anemometer continues to give reliable results in additional validation tests, the simplicity of the measurement procedure should make it an attractive technique for acquiring mean velocity and turbulence measurements in three-dimensional turbulent flows.

LIST OF REFERENCES

Akins, R. E. and Cermak, J. E., 1976, "Wind Pressures on Buildings," Colorado State University, Fluid Mechanics Program Technical Report CER76-77REA-JEC15.

Bearman, P.W., 1971, "Corrections for the Effect of Ambient Temperature Drift on Hot-Wire Measurements in Incompressible Flow," DISA Information Bulletin No. 11.

Bissonnette, L. R. and Mellor, G. L., 1974, "Experiments on the Behavior of an Axisymmetric Turbulent Boundary Layer with a Sudden Circumferential Strain," Journal of Fluid Mechanics, Vol. 63, Part 2, pp. 369-413.

Champagne, F. H., Sleicher, C. A., and Wehrmann, O. H., 1967, "Turbulence Measurements with Inclined Hot-Wires, Part 1. Heat Transfer Experiments with Inclined Hot-Wires," Journal of Fluid Mechanics, Vol. 28, Part 1, pp. 153-175.

Champagne, F. H. and Sleicher, C. A., 1967, "Turbulence Measurements with Inclined Hot-Wires, Part 2. Hot-Wire Response Equations," Journal of Fluid Mechanics, Vol. 28, Part 1, pp. 177-182.

Cooper, R. D. and Tulin, M. P., 1955, "Turbulence Measurements with the Hot-Wire Anemometer," AGARDograph No. 12.

Delleur, J. W., 1966, "Flow Direction Measurement by Hot-Wire Anemometry," Proceedings of the American Society of Civil Engineers, Journal of the Engineering Mechanics Division, Vol. 92, No. EM4, pp. 45-70.

Friehe, C. A. and Schwarz, W. H., 1968, "Deviations from the Cosine Law for Yawed Cylindrical Anemometer Sensors," Journal of Applied Mechanics, Paper No. 68 - WA/Apm-16.

Fujita, H. and Kovasznay, L. S. G., 1968, "Measurements of Reynolds Stress by a Single Rotated Hot Wire Anemometer," Review of Scientific Instruments, Vol. 39, No. 9, pp. 1351-1355.

Gessner, F. B., 1964, "A Method of Measuring Reynolds Stresses with a Constant Current; Hot-Wire Anemometer," American Society of Mechanical Engineers, Paper 64-WA/FE-34.

Hansen, A. C. and Cermak, J. E., 1975, "Vortex-Containing Wakes of Surface Obstacles," Colorado State University, Fluid Mechanics Program Technical Report CER75-76ACH-JEC16.

Hansen, A. C., 1975, Personal Communication.

Hinze, J. O., 1959, Turbulence, McGraw-Hill Book Co., New York.

Jorgensen, F. E., 1971, "Directional Sensitivity of Wire and Fiber-Film Probes," DISA Information Bulletin No. 11.

Laufer, J., 1954, "The Structure of Turbulence in Fully Developed Pipe Flow," National Advisory Committee for Aeronautics, Technical Report No. 1174.

Peterka, J. A. and Cermak, J. E., 1974, "Simulation of Atmospheric Flows in Short Wind Tunnel Test Sections," Colorado State University, Fluid Mechanics Program Technical Report CER73-74JAP-JEC32.

Pierce, F. J. and Ezekwe, C. I., 1976, "Comparison of Reynolds Stress Diagnostics by Fixed and Rotating Probes," American Institute of Aeronautics and Astronautics Journal, Vol. 14, No. 3, pp. 412-414.

Sandborn, V. A. and Laurence, J. C., 1955, "Heat Loss from Yawed Hot Wires at Subsonic Mach Numbers," National Advisory Committee for Aeronautics, Technical Note No. 3563.

Sandborn, V. A., 1972, "Class Notes for Experimental Methods in Fluid Mechanics," Department of Civil Engineering, Colorado State University, CER71-72VAS40.

Schubauer, G. B. and Klebanoff, P. S., 1946,"Theory and Application of Hot-Wire Instruments in the Investigation of Turbulent Boundary Layers," National Advisory Committee for Aeronautics, Wartime Report-86.

Sears, W. R., 1948, "The Boundary Layer of Yawed Cylinders," Journal of the Aeronautical Sciences, Vol. 15, pp. 49-52.

Webster, C. A. G., 1962, "A Note on the Sensitivity to Yaw of a Hot-Wire Anemometer," Journal of Fluid Mechanics, Vol. 13, Part 2, pp. 307-312.

Appendix A

MEAN VELOCITY CALCULATIONS FROM THE ROTATED HOT-FILM DATA

The three components of mean velocity are calculated in the probe coordinate system from N (approximately twelve) values of mean anemometer bridge voltages ($\overline{E}_i$), N angular positions of the film orientation (ψ_i), and the value of ϕ using a least squares technique. Initially, the film is calibrated over a range of flow velocities and angles of yaw to the flow. The calibration data is then fit to the following equation using a least squares technique:

$$\overline{E}^2 = A + B\,\overline{U}_T^{\,c}\, f(\overline{\theta}) \qquad (A.1)$$

where $f(\overline{\theta}) = 1.0 + A_1\,\overline{\theta} + A_2\,\overline{\theta}^2 + A_3\,\overline{\theta}^3$ and $\overline{U}_T = [\overline{U}^2 + \overline{V}^2 + \overline{W}^2]^{1/2}$. Since equation (A.1) is a variable exponent form of King's Law, an initial value of the exponent, c, is assumed, and then Newton's iterative technique is used to alter the initial value of the exponent. This iterative process continues until the change in the exponent is less than a specified minimum. Referring to Figure 10, and using simple geometrical considerations, the angle $\overline{\theta}$ is given by the following equation:

$$\overline{\theta} = \text{Arccos}\left[\frac{\overline{U}\cos\phi + \overline{V}\sin\phi\cos\psi + \overline{W}\sin\phi\sin\psi}{\overline{U}_T}\right] \qquad (A.2)$$

The method of least squares is then applied to equation (A.1) in the following manner:

$$S = \sum_{i=1}^{N} [\overline{U}_T^{\,c}\, f(\overline{\theta}_i) - s_i]^2 \qquad (A.3)$$

where $s_i = [\overline{E}_i^2 - A]/B$. The value of S is then minimized using the following conditions:

$$\frac{\partial S}{\partial \overline{U}} = 0, \quad \frac{\partial S}{\partial \overline{V}} = 0, \quad \frac{\partial S}{\partial \overline{W}} = 0 \tag{A.4}$$

Applying the conditions in (A.4) to equation (A.3) gives the following set of equations:

$$\frac{\partial S}{\partial \overline{U}_j} = 0 = \sum_{i=1}^{N} [\overline{U}_T{}^c f(\overline{\theta}_i) - s_i]\ \overline{U}_T{}^{c-2} [c\overline{U}_j f(\overline{\theta}_i) + \overline{U}_T{}^2 f'(\overline{\theta}_i)\ \frac{\partial \overline{\theta}_i}{\partial \overline{U}_j}] =$$

$$F_j,\ j = 1,\ 2,\ 3 \tag{A.5}$$

(A.5) gives a system of three equations and three unknowns in $\overline{U}$, $\overline{V}$, and $\overline{W}$. Assuming initial guesses for $\overline{U}$, $\overline{V}$, and $\overline{W}$, values of F_j can be calculated. First order corrections to the mean velocity components are calculated using Newton's iterative method as follows:

$$F_{j\ new} = 0 = F_{j\ old} + \frac{\partial F_j}{\partial \overline{U}_k}\ \Delta \overline{U}_k,\ j = 1,\ 2,\ 3. \tag{A.6}$$

The details in the calculation of the coefficients in equations (A.6) become quite involved. Equation (A.5) is written in the following form for convenience in programming:

$$F_1 = \sum_{i=1}^{N} X_{1_i}\ X_2\ X_{3_i}$$

$$F_2 = \sum_{i=1}^{N} X_{1_i}\ X_2\ X_{4_i} \tag{A.7}$$

$$F_3 = \sum_{i=1}^{N} X_{1_i}\ X_2\ X_{5_i}$$

where the definitions of X_{ℓ_i} are obvious by comparing the equations in (A.7) to equation (A.5). The value of $\partial F_i/\partial \bar{U}_k$ is given in the following form:

$$\frac{\partial F_1}{\partial \bar{U}_k} = \sum_{i=1}^{N} \left\{ \frac{\partial X_{1_i}}{\partial \bar{U}_k} X_2 X_{3_i} + X_{1_i} \frac{\partial X_2}{\partial \bar{U}_k} X_{3_i} + X_{1_i} X_2 \frac{\partial X_{3_i}}{\partial \bar{U}_k} \right\} \tag{A.8}$$

Similar equations can be written for $\partial F_2/\partial \bar{U}_k$ and $\partial F_3/\partial \bar{U}_k$. The quantities which are contained in $\partial F_1/\partial \bar{U}_k$, $\partial F_2/\partial \bar{U}_k$, and $\partial F_3/\partial \bar{U}_k$ are written in the following form:

$$\frac{\partial X_1}{\partial \bar{U}_k} = c\, \bar{U}_k\, \bar{U}_T^{c-2} f(\bar{\theta}) + \bar{U}_T^{c} f'(\bar{\theta}) \frac{\partial \bar{\theta}}{\partial \bar{U}_k} \tag{A.9}$$

$$\frac{\partial X_2}{\partial \bar{U}_k} = (c-2)\, \bar{U}_k\, \bar{U}_T^{c-4} \tag{A.10}$$

$$\frac{\partial X_3}{\partial \bar{U}} = c\, f(\bar{\theta}) + (c+2)\, \bar{U} f'(\bar{\theta}) \frac{\partial \bar{\theta}}{\partial \bar{U}} + \bar{U}_T^{2} f''(\bar{\theta}) \left(\frac{\partial \bar{\theta}}{\partial \bar{U}}\right)^2 + \bar{U}_T^{2} f'(\bar{\theta}) \frac{\partial^2 \bar{\theta}}{\partial \bar{U}^2} \tag{A.11}$$

$$\frac{\partial X_3}{\partial \bar{V}} = c\, \bar{U} f'(\bar{\theta}) \frac{\partial \bar{\theta}}{\partial \bar{V}} + 2\bar{V} f'(\bar{\theta}) \frac{\partial \bar{\theta}}{\partial \bar{U}} + \bar{U}_T^{2} f''(\bar{\theta}) \frac{\partial \bar{\theta}}{\partial \bar{U}} \frac{\partial \bar{\theta}}{\partial \bar{V}} + \bar{U}_T^{2} f'(\bar{\theta}) \frac{\partial^2 \bar{\theta}}{\partial \bar{U} \partial \bar{V}} \tag{A.12}$$

$$\frac{\partial X_3}{\partial \bar{W}} = c\, \bar{U} f'(\bar{\theta}) \frac{\partial \bar{\theta}}{\partial \bar{W}} + 2\, \bar{W} f'(\bar{\theta}) \frac{\partial \bar{\theta}}{\partial \bar{U}} + \bar{U}_T^{2} f''(\bar{\theta}) \frac{\partial \bar{\theta}}{\partial \bar{U}} \frac{\partial \bar{\theta}}{\partial \bar{W}} + \bar{U}_T^{2} f'(\bar{\theta}) \frac{\partial^2 \bar{\theta}}{\partial \bar{U} \partial \bar{W}} \tag{A.13}$$

Similarly,

$$\frac{\partial X_4}{\partial \bar{U}_k} = c\, f(\bar{\theta})\, \delta_{2k} + c\, \bar{U}_2\, f'(\bar{\theta})\, \frac{\partial \bar{\theta}}{\partial \bar{U}_k} + 2\, \bar{U}_k\, f'(\bar{\theta})\, \frac{\partial \bar{\theta}}{\partial \bar{U}_2}$$

$$+ \bar{U}_T^{\,2}\, f''(\bar{\theta})\, \frac{\partial \bar{\theta}}{\partial \bar{U}_k}\, \frac{\partial \bar{\theta}}{\partial \bar{U}_2} + \bar{U}_T^{\,2}\, f'(\bar{\theta})\, \frac{\partial^2 \bar{\theta}}{\partial \bar{U}_k \partial \bar{U}_2} \qquad \text{(A.14)}$$

and

$$\frac{\partial X_5}{\partial \bar{U}_k} = c\, f(\bar{\theta})\, \delta_{3k} + c\, \bar{U}_3\, f'(\bar{\theta})\, \frac{\partial \bar{\theta}}{\partial \bar{U}_k} + 2\, \bar{U}_k f'(\bar{\theta})\, \frac{\partial \bar{\theta}}{\partial \bar{U}_3}$$

$$+ \bar{U}_T^{\,2}\, f''(\bar{\theta})\, \frac{\partial \bar{\theta}}{\partial \bar{U}_k}\, \frac{\partial \bar{\theta}}{\partial \bar{U}_3} + \bar{U}_T^{\,2}\, f'(\bar{\theta})\, \frac{\partial^2 \bar{\theta}}{\partial \bar{U}_k \partial \bar{U}_3} \qquad \text{(A.15)}$$

The values $\partial\bar{\theta}/\partial\bar{U}_k$ which are contained in equations (A.9) through (A.15) are given by:

$$\frac{\partial \bar{\theta}}{\partial \bar{U}} = \frac{\bar{U} \cos \bar{\theta} - \bar{U}_T \cos \phi}{\bar{U}_T^{\,2} \sin \bar{\theta}} \qquad \text{(A.16)}$$

$$\frac{\partial \bar{\theta}}{\partial \bar{V}} = \frac{\bar{V} \cos \bar{\theta} - \bar{U}_T \sin \phi \sin \psi}{\bar{U}_T^{\,2} \sin \bar{\theta}} \qquad \text{(A.17)}$$

$$\frac{\partial \bar{\theta}}{\partial \bar{W}} = \frac{\bar{W} \cos \bar{\theta} - \bar{U}_T \sin \phi \sin \psi}{\bar{U}_T^{\,2} \sin \bar{\theta}} \qquad \text{(A.18)}$$

The values of F_j and the derivations in equations (A.9) through (A.15) can now be calculated using equations (A.16) through (A.18). Making a closer examination of the quantities $\partial F_1/\partial\bar{U}_k$, $\partial F_2/\partial\bar{U}_k$, and $\partial F_3/\partial\bar{U}_k$, a simplification in the calculation of these quantities can be obtained. The quantity $\partial F_1/\partial\bar{V}$ can be written as:

$$\frac{\partial F_1}{\partial \overline{V}} = \frac{\partial^2 S}{\partial \overline{V} \partial \overline{U}}, \tag{A.19}$$

and $\partial F_2/\partial \overline{U}$ can be written as

$$\frac{\partial F_2}{\partial \overline{U}} = \frac{\partial^2 S}{\partial \overline{U} \partial \overline{V}} \tag{A.20}$$

The quantities $\partial^2 S/\partial \overline{V} \partial \overline{U}$ and $\partial^2 S/\partial \overline{U} \partial \overline{V}$ are equal, and therefore, $\partial F_1/\partial \overline{V}$ and $\partial F_2/\partial \overline{U}$ are equal. Similarly, $\partial F_1/\partial \overline{W}$ and $\partial F_3/\partial \overline{U}$, in addition to, $\partial F_2/\partial \overline{W}$ and $\partial F_3/\partial \overline{V}$, are equal, respectively, and thus, the coefficient matrix $\partial F_j/\partial \overline{U}_k$ in equation (A.6) is symmetrical. The values $\Delta \overline{U}_k$ in equation (A.6) are calculated using Gaussian elimination. The previous values of the three mean velocity components are then incremented by $\Delta \overline{U}_k$. This iteration process continues until an acceptable solution is given when the values of $\Delta \overline{U}_k$ are less than a specified minimum ($|\Delta \overline{U}_k| < 0.0005$).

Appendix B

REYNOLDS STRESS CALCULATIONS FROM THE ROTATED HOT-FILM DATA

The six velocity correlations are calculated in the probe coordinate system from N (approximately twelve) pairs of mean anemometer bridge voltages ($\overline{E}_i$) and root-mean-square voltages (E_{rms_i}), N angular positions of the film orientation (ψ_i), and the value of ϕ using a least-squares technique. Equation (A.1) can be written in the following form:

$$(\overline{E} + e)^2 = A + B\, U_T^{\,c}\, f(\theta) \tag{B.1}$$

where $U_T = [(\overline{U} + u)^2 + (\overline{V} + v)^2 + (\overline{W} + w)^2]^{1/2}$, e is the fluctuating anemometer bridge voltage, and (u, v, and w) are the fluctuating velocity components. Equation (B.1) can be written in the following form:

$$e^2 = A+B\, U_T^{\,c} f(\theta) + \overline{E}^2 - 2\overline{E}[A+B\, U_T^{\,c} f(\theta)]^{1/2} = h(U_T) \tag{B.2}$$

where $h(U_T)$ is used here for convenience. In order to relate the square of the voltage fluctuations to the six velocity correlations, the quantity $h(U_T)$ is expanded in a Taylor series about $\overline{U}$, $\overline{V}$, and $\overline{W}$ excluding all terms above second order.

The expansion is given in the following form:

$$h(U_T) = \frac{1}{2}\,[u^2\, h_{UU}(\overline{U}_T) + v^2\, h_{VV}(\overline{U}_T) + w^2\, h_{WW}(\overline{U}_T)]$$

$$+ uv\, h_{UV}(\overline{U}_T) + uw\, h_{UW}(\overline{U}_T) + vw\, h_{VW}(\overline{U}_T). \tag{B.3}$$

The quantities in equation (B.3) are listed below:

$$h_{UU}(\overline{U}_T) = \frac{1}{2}\left[\frac{B\, c\, \overline{U}_T^{\,c}}{\overline{E}}\right]^2 \left[\frac{\overline{U}}{\overline{U}_T^{\,2}}\, f(\overline{\theta}) + \frac{1}{c}\, f_U(\overline{\theta})\right]^2 \tag{B.4}$$

$$h_{VV}(\bar{U}_T) = \frac{1}{2}\left[\frac{B\ c\ \bar{U}_T^{\,c}}{\bar{E}}\right]^2\left[\frac{\bar{V}}{\bar{U}_T^{\,2}}\ f(\bar{\theta}) + \frac{1}{c}\ f_V(\bar{\theta})\right]^2 \qquad (B.5)$$

$$h_{WW}(\bar{U}_T) = \frac{1}{2}\left[\frac{B\ c\ \bar{U}_T^{\,c}}{\bar{E}}\right]^2\left[\frac{\bar{W}}{\bar{U}_T^{\,2}}\ f(\bar{\theta}) + \frac{1}{c}\ f_W(\bar{\theta})\right]^2 \qquad (B.6)$$

$$h_{UV}(\bar{U}_T) = \frac{1}{2}\left[\frac{B\ c\ \bar{U}_T^{\,c}}{\bar{E}}\right]^2\left[\frac{\bar{U}}{\bar{U}_T^{\,2}}\ f(\bar{\theta}) + \frac{1}{c}\ f_U(\bar{\theta})\right]\left[\frac{\bar{V}}{\bar{U}_T^{\,2}}\ f(\bar{\theta}) + \frac{1}{c}\ f_V(\bar{\theta})\right] \qquad (B.7)$$

$$h_{UW}(\bar{U}_T) = \frac{1}{2}\left[\frac{B\ c\ \bar{U}_T^{\,c}}{\bar{E}}\right]^2\left[\frac{\bar{U}}{\bar{U}_T^{\,2}}\ f(\bar{\theta}) + \frac{1}{c}\ f_U(\bar{\theta})\right]\left[\frac{\bar{W}}{\bar{U}_T^{\,2}}\ f(\bar{\theta}) + \frac{1}{c}\ f_W(\bar{\theta})\right] \qquad (B.8)$$

$$h_{VW}(\bar{U}_T) = \frac{1}{2}\left[\frac{B\ c\ \bar{U}_T^{\,c}}{\bar{E}}\right]^2\left[\frac{\bar{V}}{\bar{U}_T^{\,2}}\ f(\bar{\theta}) + \frac{1}{c}\ f_V(\bar{\theta})\right]\left[\frac{\bar{W}}{\bar{U}_T^{\,2}}\ f(\bar{\theta}) + \frac{1}{c}\ f_W(\bar{\theta})\right] \qquad (B.9)$$

The values of $f_{U_j}(\bar{\theta})$ ($j = 1, 2, 3$) which are contained in equations (B.4) through (B.9) are given by:

$$f_{U_j}(\bar{\theta}) = \frac{\partial f(\bar{\theta})}{\partial \bar{\theta}}\ \frac{\partial \bar{\theta}}{\partial \bar{U}_j}\ , \quad j = 1, 2, 3 \qquad (B.10)$$

After substituting the quantities (B.4) through (B.9) into equation (B.3), and then taking the average of the resulting equation, an equation in the following form is obtained:

$$\left[\frac{2\overline{E}\ E_{rms}}{Bc\overline{U}_T{}^{c-1}}\right]^2 = \left[\frac{\overline{U}}{\overline{U}_T} f(\overline{\theta}) + \frac{\overline{U}_T}{c} f_U(\overline{\theta})\right]^2 u'^2 + \left[\frac{\overline{V}}{\overline{U}_T} f(\overline{\theta}) + \frac{\overline{U}_T}{c} f_V(\overline{\theta})\right]^2 v'^2$$

$$+ \left[\frac{\overline{W}}{\overline{U}_T} f(\overline{\theta}) + \frac{\overline{U}_T}{c} f_W(\overline{\theta})\right]^2 w'^2$$

$$+ 2\left[\frac{\overline{U}}{\overline{U}_T} f(\overline{\theta}) + \frac{\overline{U}_T}{c} f_U(\overline{\theta})\right]\left[\frac{\overline{V}}{\overline{U}_T} f(\overline{\theta}) + \frac{\overline{U}_T}{c} f_V(\overline{\theta})\right] \overline{uv}$$

$$+ 2\left[\frac{\overline{U}}{\overline{U}_T} f(\overline{\theta}) + \frac{\overline{U}_T}{c} f_U(\overline{\theta})\right]\left[\frac{\overline{W}}{\overline{U}_T} f(\overline{\theta}) + \frac{\overline{U}_T}{c} f_W(\overline{\theta})\right] \overline{uw}$$

$$+ 2\left[\frac{\overline{V}}{\overline{U}_T} f(\overline{\theta}) + \frac{\overline{U}_T}{c} f_V(\overline{\theta})\right]\left[\frac{\overline{W}}{\overline{U}_T} f(\overline{\theta}) + \frac{\overline{U}_T}{c} f_W(\overline{\theta})\right] \overline{vw} \qquad (B.11)$$

Equation (B.11) is then written in the following form for more convenience in programming:

$$\left[\frac{2\overline{E}\ E_{rms}}{Bc\overline{U}_T{}^{c-1}}\right]^2 = X_1 u'^2 + X_2 v'^2 + X_3 w'^2 + 2X_4\overline{uv} + 2X_5\overline{uw} + 2X_6\overline{vw} \qquad (B.12)$$

where the definitions of X_1 through X_6 are obvious comparing equations (B.11) and (B.12).

The method of least squares is applied to equation (B.12) giving the following equation:

$$S = \sum_{i=1}^{N} \left\{ X_{1_i} u'^2 + X_{2_i} v'^2 + X_{3_i} w'^2 + 2X_{4_i}\overline{uv} + 2X_{5_i}\overline{uw} \right.$$

$$\left. + 2X_{6_i}\overline{vw} - \left[\frac{2\ \overline{E}_i\ E_{rms_i}}{B\ c\ \overline{U}_T{}^{c-1}}\right]^2 \right\}^2 \qquad (B.13)$$

The value of S is then minimized using the following conditions:

$$\frac{\partial S}{\partial u'^2} = 0, \quad \frac{\partial S}{\partial v'^2} = 0, \quad \frac{\partial S}{\partial w'^2} = 0,$$

$$\frac{\partial S}{\partial \overline{uv}} = 0, \quad \frac{\partial S}{\partial \overline{uw}} = 0, \quad \frac{\partial S}{\partial \overline{vw}} = 0 \tag{B.14}$$

By defining the quantity F_i,

$$F_i = X_{1_i} u'^2 + X_{2_i} v'^2 + X_{3_i} w'^2 + 2X_{4_i} \overline{uv} + 2X_{5_i} \overline{uw}$$

$$+ 2X_{6_i} \overline{vw} - \left[\frac{2 \bar{E}_i E_{rms_i}}{B c \bar{U}_T^{c-1}} \right]^2, \tag{B.15}$$

the conditions in (B.14) are applied to equation (B.12) yielding the following equations:

$$\frac{\partial S}{\partial u'^2} = 0 = \sum_{i=1}^{N} F_i X_{1_i}$$

$$\frac{\partial S}{\partial v'^2} = 0 = \sum_{i=1}^{N} F_i X_{2_i}$$

$$\frac{\partial S}{\partial w'^2} = 0 = \sum_{i=1}^{N} F_i X_{3_i} \tag{B.16}$$

$$\frac{\partial S}{\partial \overline{uv}} = 0 = \sum_{i=1}^{N} F_i X_{4_i}$$

$$\frac{\partial S}{\partial \overline{uw}} = 0 = \sum_{i=1}^{N} F_i X_{5_i}$$

$$\frac{\partial S}{\partial \overline{vw}} = 0 = \sum_{i=1}^{N} F_i X_{6_i}$$

Gaussian elimination is used to solve the system of six equations and six unknowns in (B.16) for the six velocity correlations. The calculations for the mean velocity and velocity correlations can be readily computed on the CDC 6400 computer.

Appendix C

ERROR ANALYSIS USING A MONTE CARLO SIMULATION TECHNIQUE

In order to use a Monte Carlo simulation technique to determine the resolution of the measurement quantities which are obtained by the rotated hot-film anemometer system, a measure of the resolution in the experimental data has to be known. Five experimental quantities are subject to the random errors which arise in the data acquisition. These quantities are the mean voltage, the rms value of the voltage fluctuations, the initial value of the angle ψ, each angle ψ, and the angle ϕ. (Normally, the value of ϕ would be 45°. However, due to the misalignment between the probe support and the sensor prong support, the angle ϕ has been found to be greater than 45° for the films which are used in this work. This value of ϕ has been accurately determined for each hot film calibration.) The resolution in these five experimental quantities was determined by obtaining sequential trials and also by comparing sets of actual data with generated data. Typical conservative values are shown in Table 1.

After the resolution in the experimental quantities had been determined, the following procedure was used to distribute random errors to the "exact" experimental data. Pseudorandom numbers are selected from a list such that they follow a Gaussian distribution. The pseudorandom numbers in this list lie between 0.0 and 1.0, and the Gaussian distribution has a mean of 1/2 and a variance of 1/36. A pseudorandom number is selected from the list, and its frequency value is calculated by using the frequency function of the Gaussian distribution. Another pseudorandom number is selected, and its magnitude is compared with the frequency value computed from the previous pseudorandom number. If the

second pseudorandom number is found to be less than the frequency value, the first pseudorandom number is then used to distribute a random error to the data. If the second pseudorandom number is greater than the corresponding frequency value, then the first number is discarded. Random errors are distributed to the experimental data using the following algorithm:

$$x = \bar{x} + 6\sigma z - 3\sigma \tag{C.1}$$

where x is the random data value, $\bar{x}$ is the "exact" experimental data value, σ is the standard deviation corresponding to the experimental quantity, and z is the pseudorandom number. By following this procedure random errors are distributed to the "exact" experimental data according to the Gaussian law. All that remains to complete this Monte Carlo technique is to supply this randomly generated experimental data to the hot-film reduction program and calculate a significant number of solutions to arrive at reasonably accurate values of the standard deviations in the measurement quantities.

TABLE 1

Standard Deviations in Experimental Quantities

Experimental Quantity		Standard Deviation
Mean Voltage	Low turbulence intensity ($u'/\bar{U} < 0.09$)	0.00810 volts
	High turbulence intensity ($u'/\bar{U} > 0.16$)	0.00858 volts
RMS Voltage	Low turbulence intensity ($u'/\bar{U} < 0.09$)	0.00056 volts
	High turbulence intensity ($u'/\bar{U} > 0.16$)	0.00086 volts
ψ_o		1.0°
ψ		1.0°
ϕ		0.25°

TABLE 2

Standard Deviations in Velocity Components

Velocity Component	Standard Deviation	
	Low turbulence intensity ($u'/\overline{U} = 0.06$)	High turbulence intensity ($u'/\overline{U} = 0.18$)
Mean Velocity*		
$\overline{U}$	0.51	0.62
$\overline{V}$	1.06	1.17
$\overline{W}$	0.87	1.04
Horizontal and Vertical Angles		
β_1	0.50°	0.59°
β_2	0.60°	0.67°
Mean Swirl Velocity*		
$\overline{U}_S$	1.33	1.96
Reynolds Normal Stresses**		
u'	5.85	3.83
v'	10.15	7.05
w'	11.26	9.94
Reynolds Shear Stresses***		
$\overline{uv}$	4.85	5.92
$\overline{uw}$	4.59	5.99
$\overline{vw}$	2.89	3.33

* Standard deviation given as a percent of the local $\overline{U}$.
** Standard deviation given as a percent of the local u'.
*** Standard deviation given as a percent of the local u'^2.

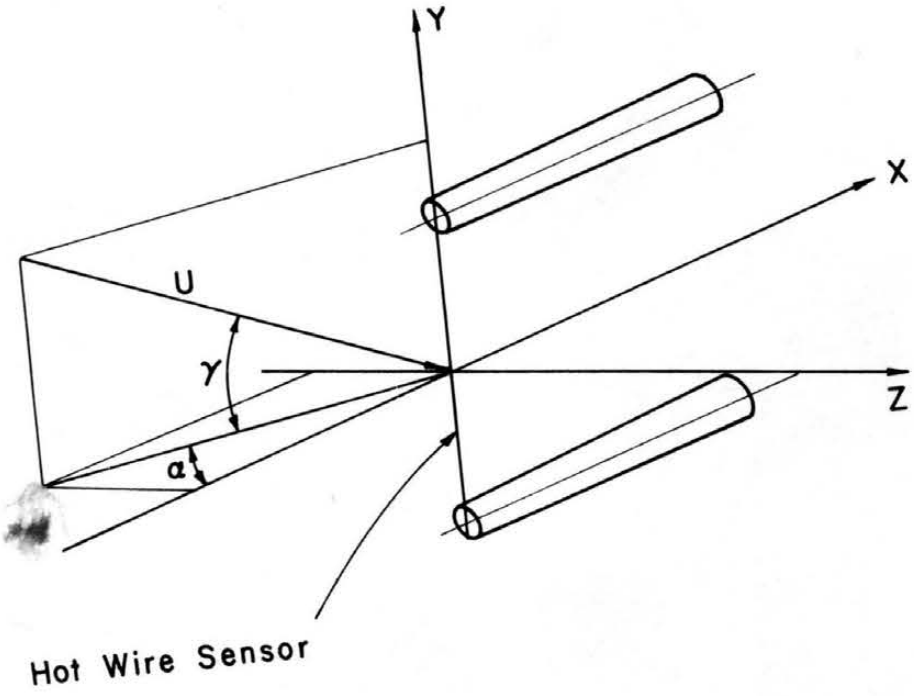

Figure 1. Schematic of the Hot Wire Sensor Showing the Angles of Yaw and Pitch.

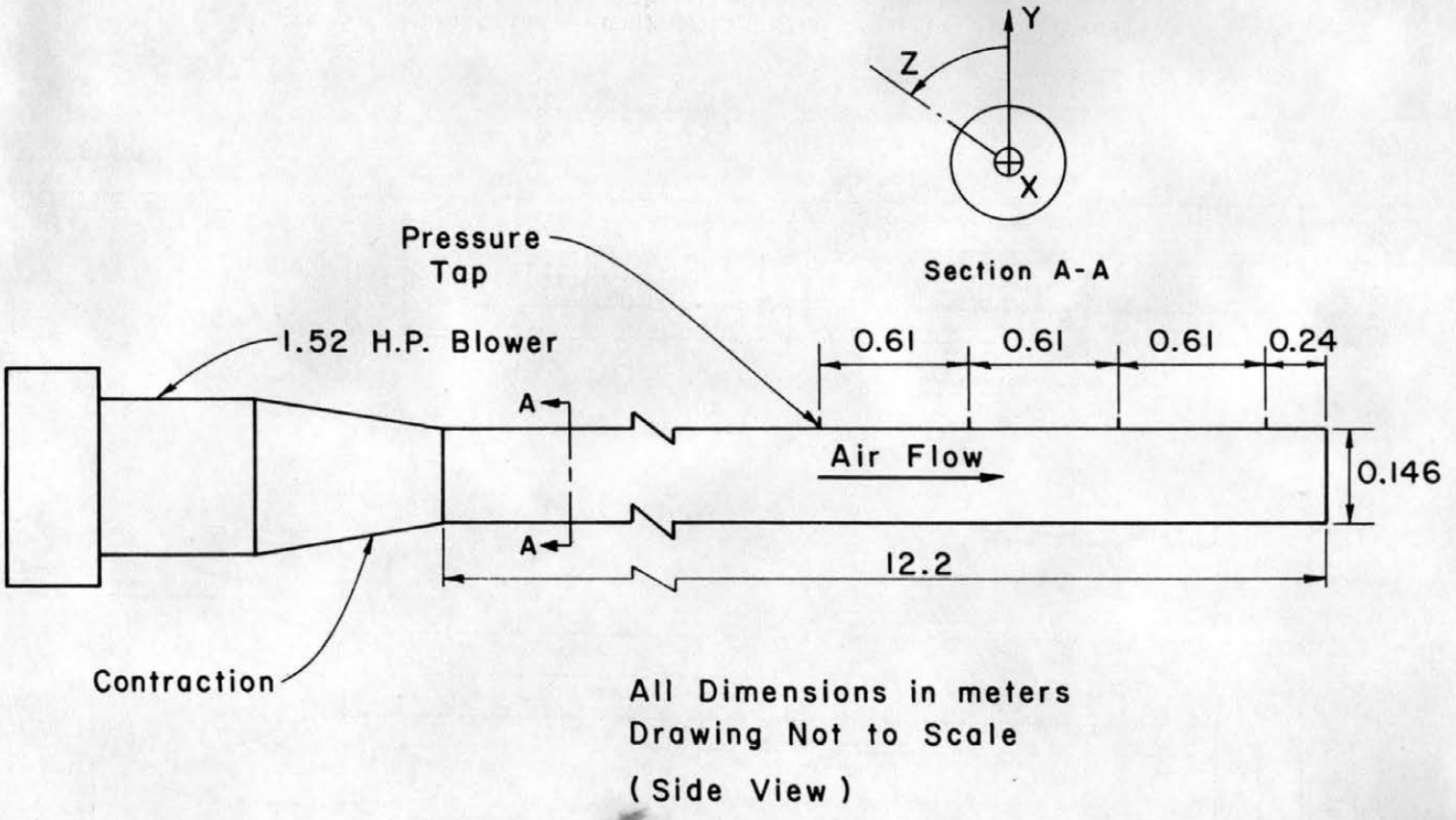

Figure 2. Pipe Test Facility, Fluid Dynamics and Diffusion Laboratory, Colorado State University.

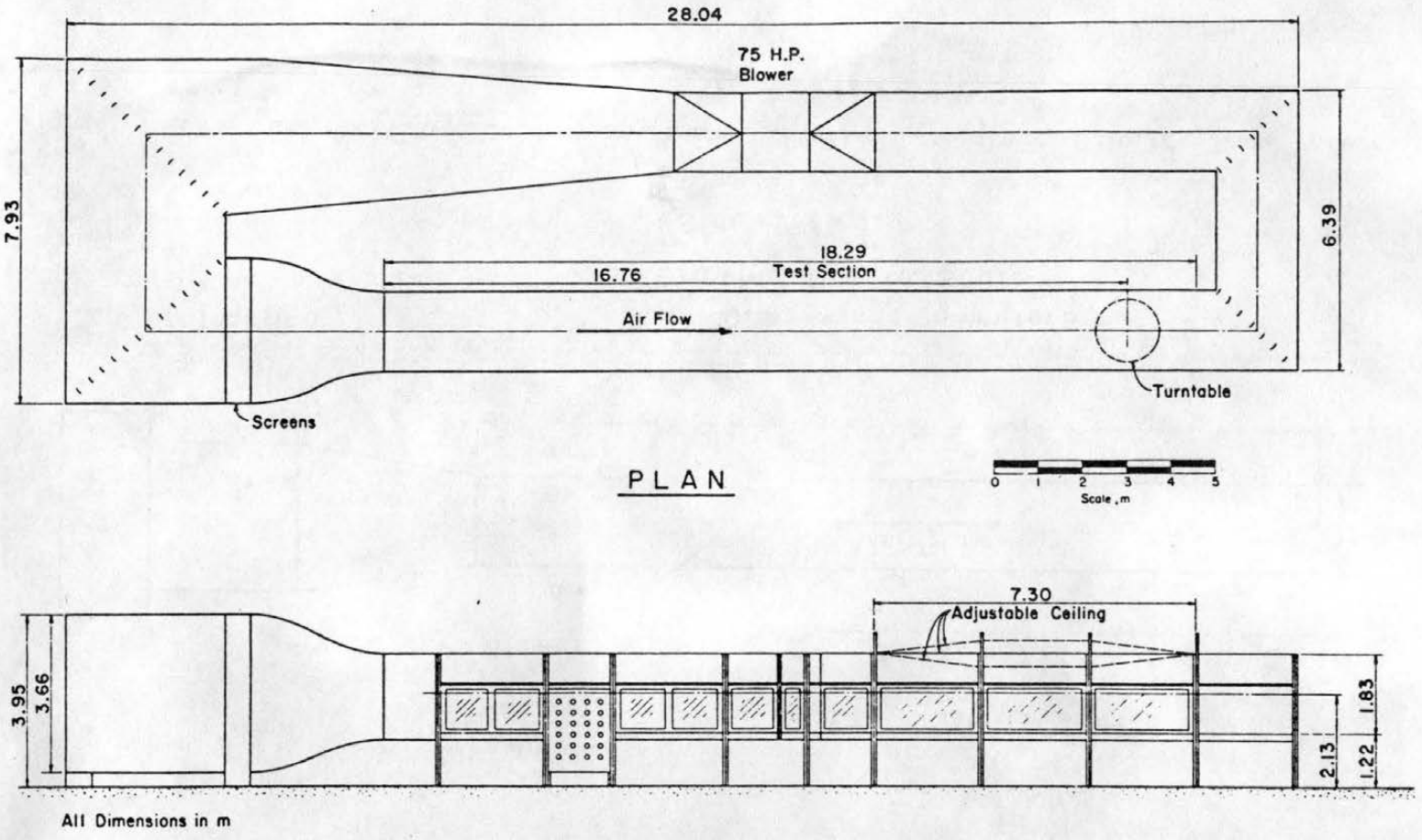

Figure 3. Industrial Aerodynamics Wind Tunnel, Fluid Dynamics and Diffusion Laboratory, Colorado State University.

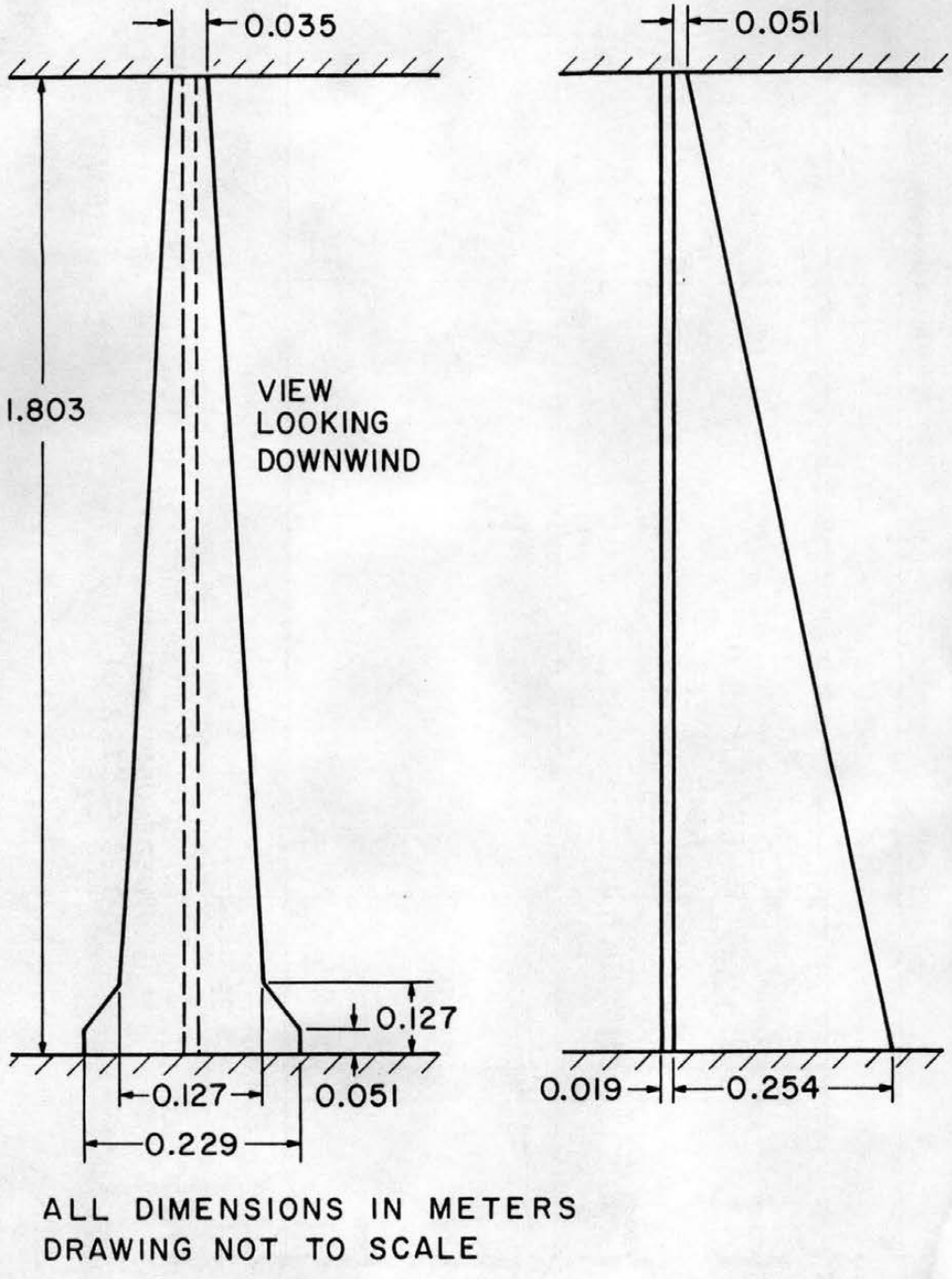

Figure 4. Spire Geometry.

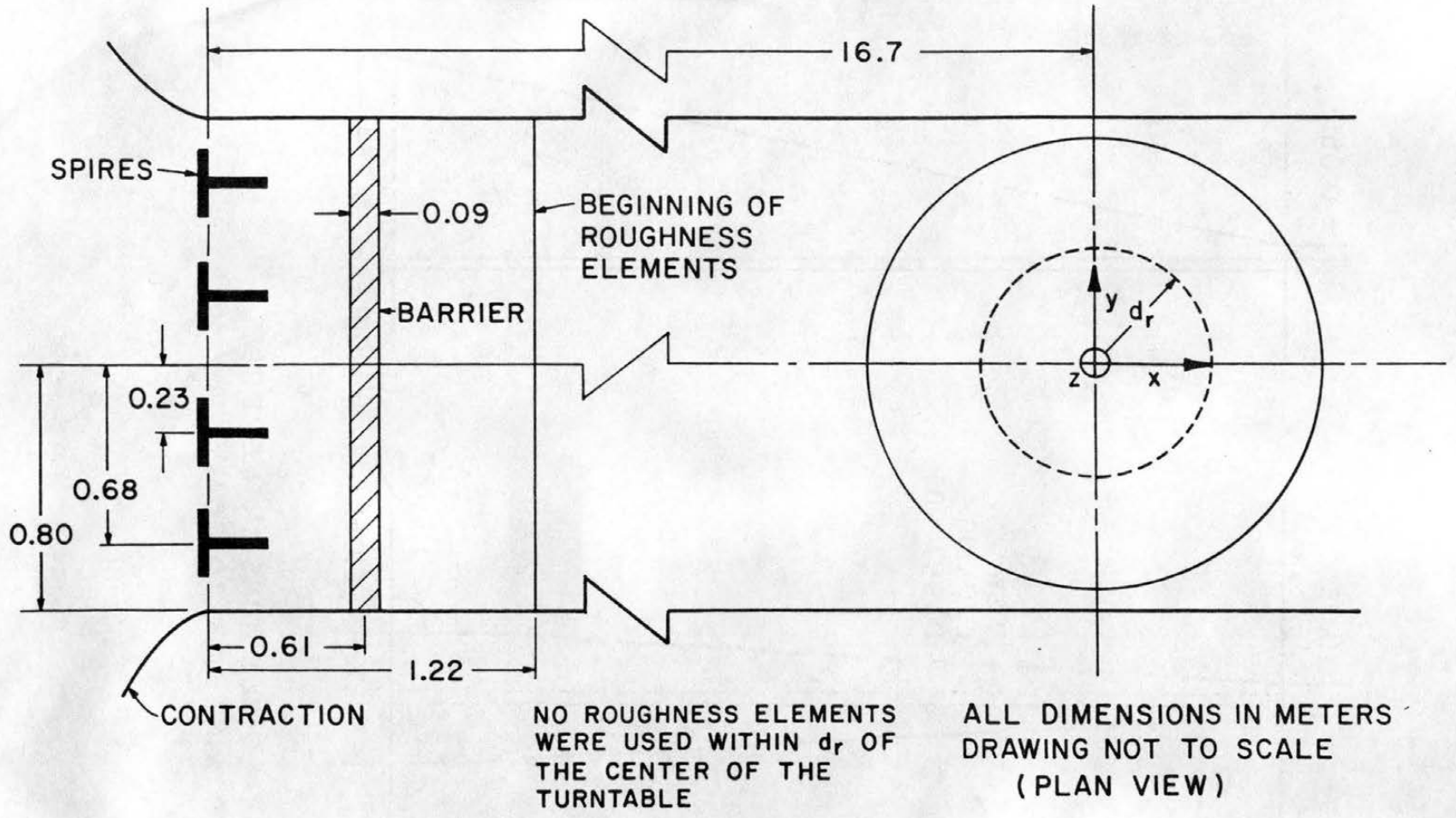

Figure 5. Wind Tunnel Arrangement.

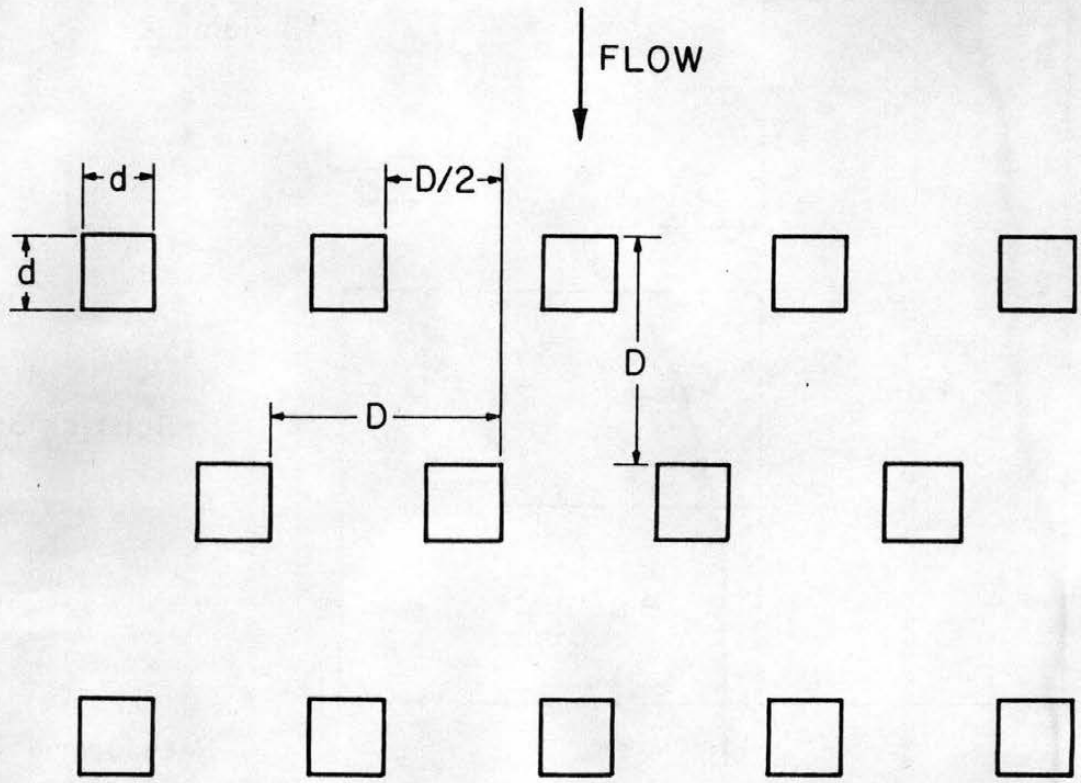

INDIVIDUAL BLOCKS ARE CUBES

BOUNDARY LAYER	D(m)	d(m)	d_r(m)
1	—	0.000	—
2	0.075	0.025	0.84

D/d = 3.0

Figure 6. Roughness Configuration.

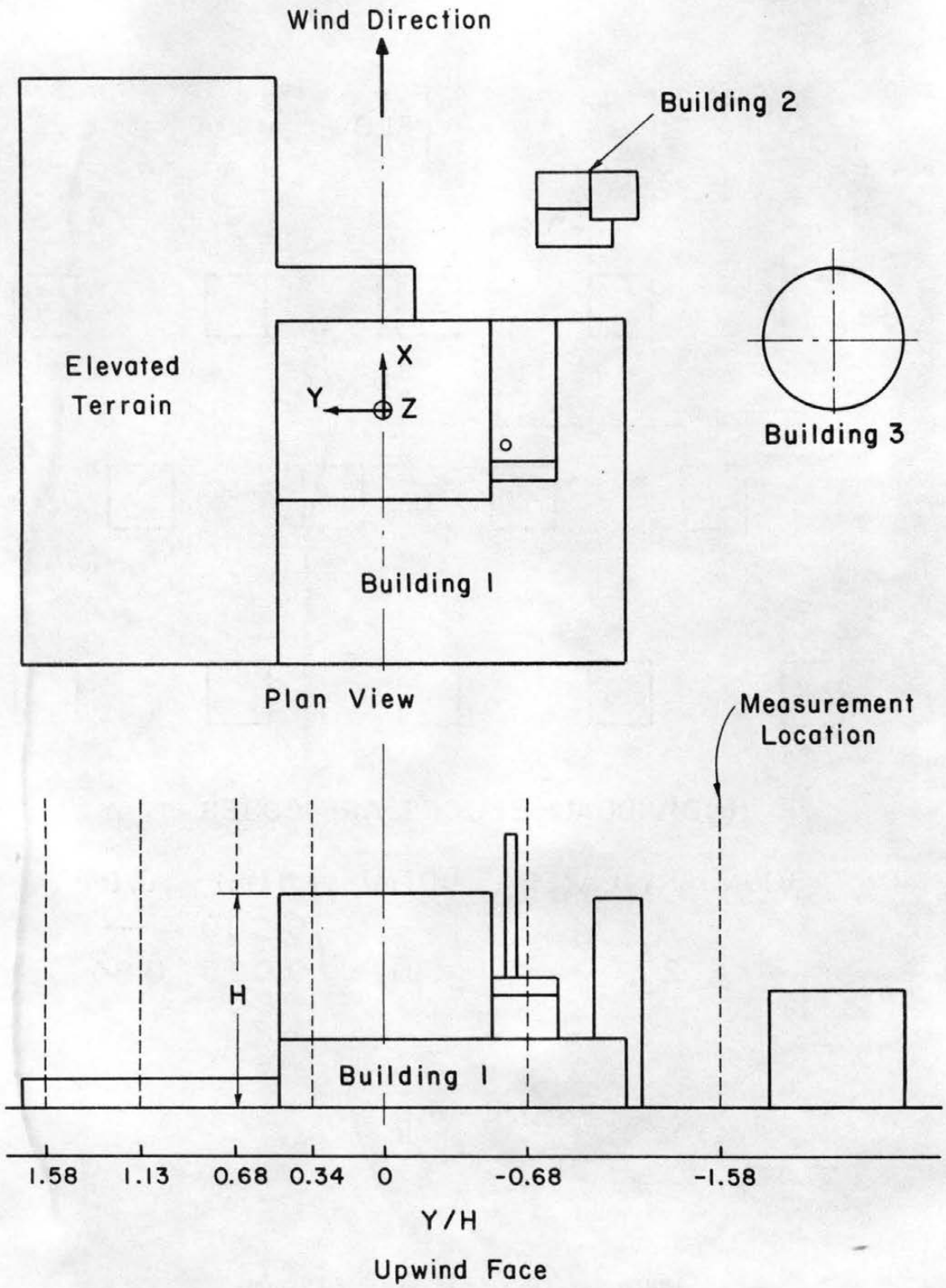

Figure 7. Schematic of Power Plant Model Showing the Coordinate System and the Measurement Locations.

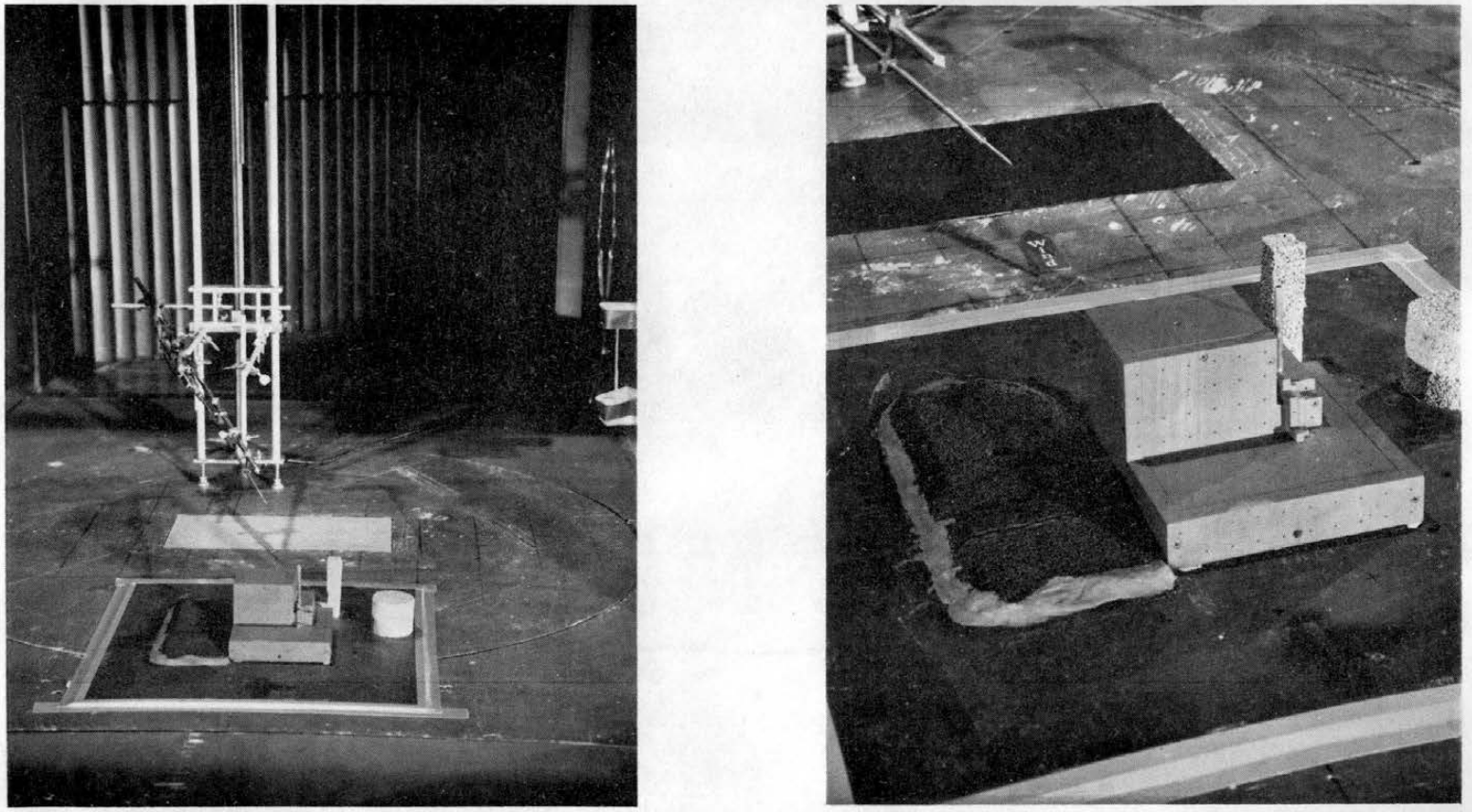

Figure 8. Power Plant Model Installed in the Wind Tunnel with Rotated Hot-Film Probe.

Figure 9. Rotated Hot-Film Probe System.

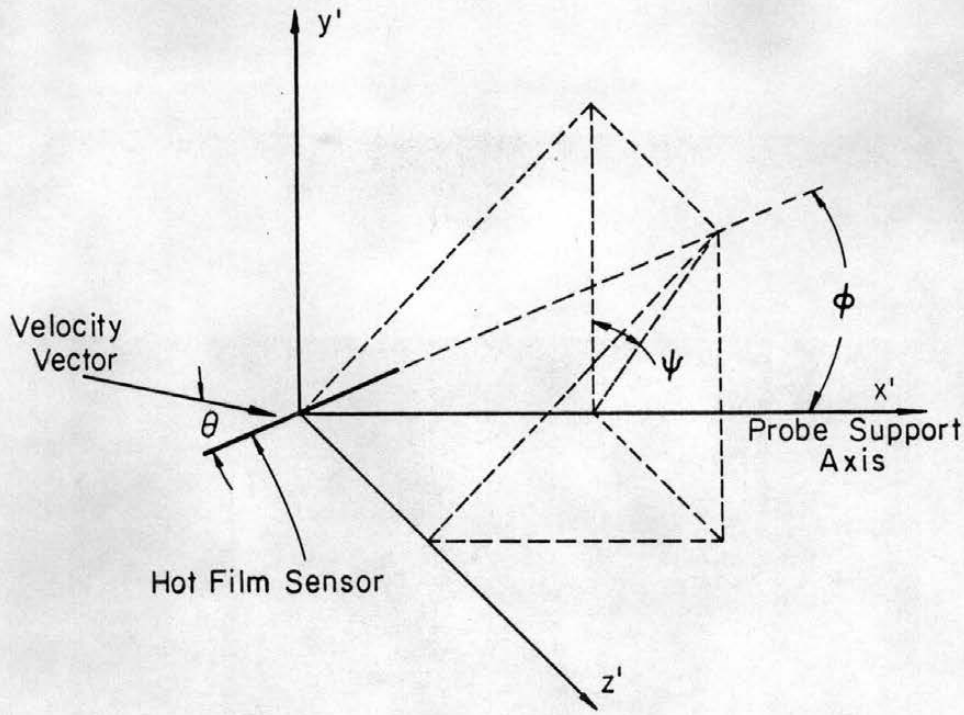

(a)

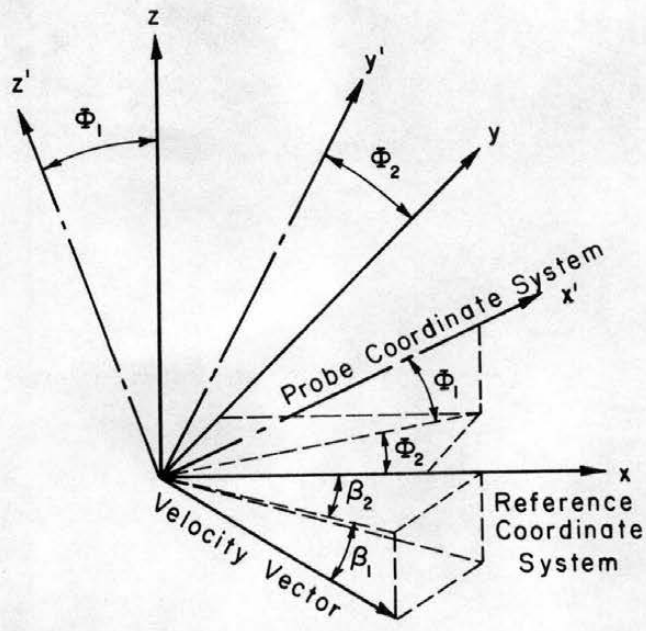

(b)

Figure 10. (a) Schematic of the Probe Coordinate System and (b) Definition of the Offset Angles Φ_1 and Φ_2 of the Probe Coordinate System from the Reference Coordinate System and the Definition of the Angles β_1 and β_2 in the Reference Coordinate System.

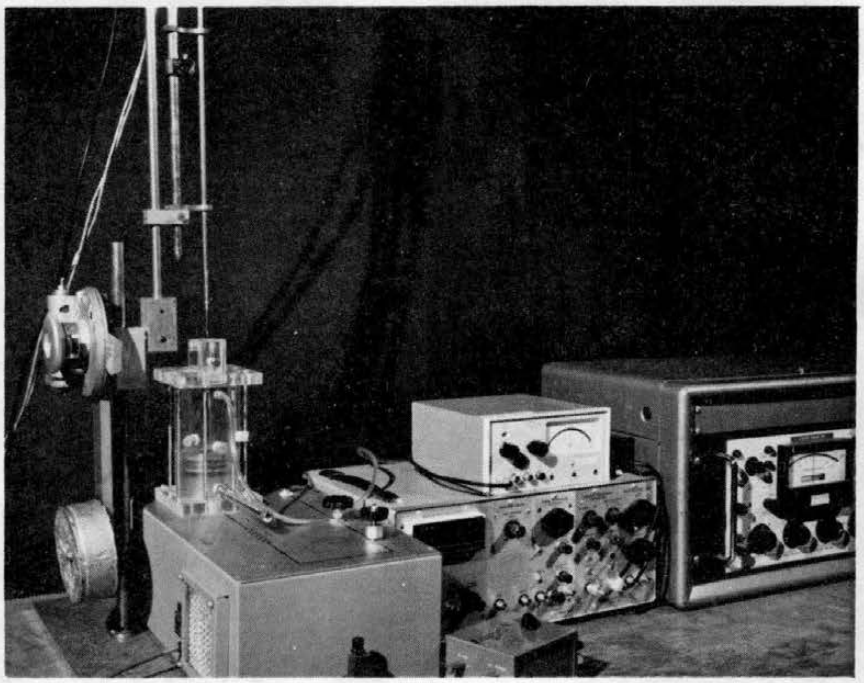

Figure 11. Calibration Setup for Rotated Hot-Film Sensor.

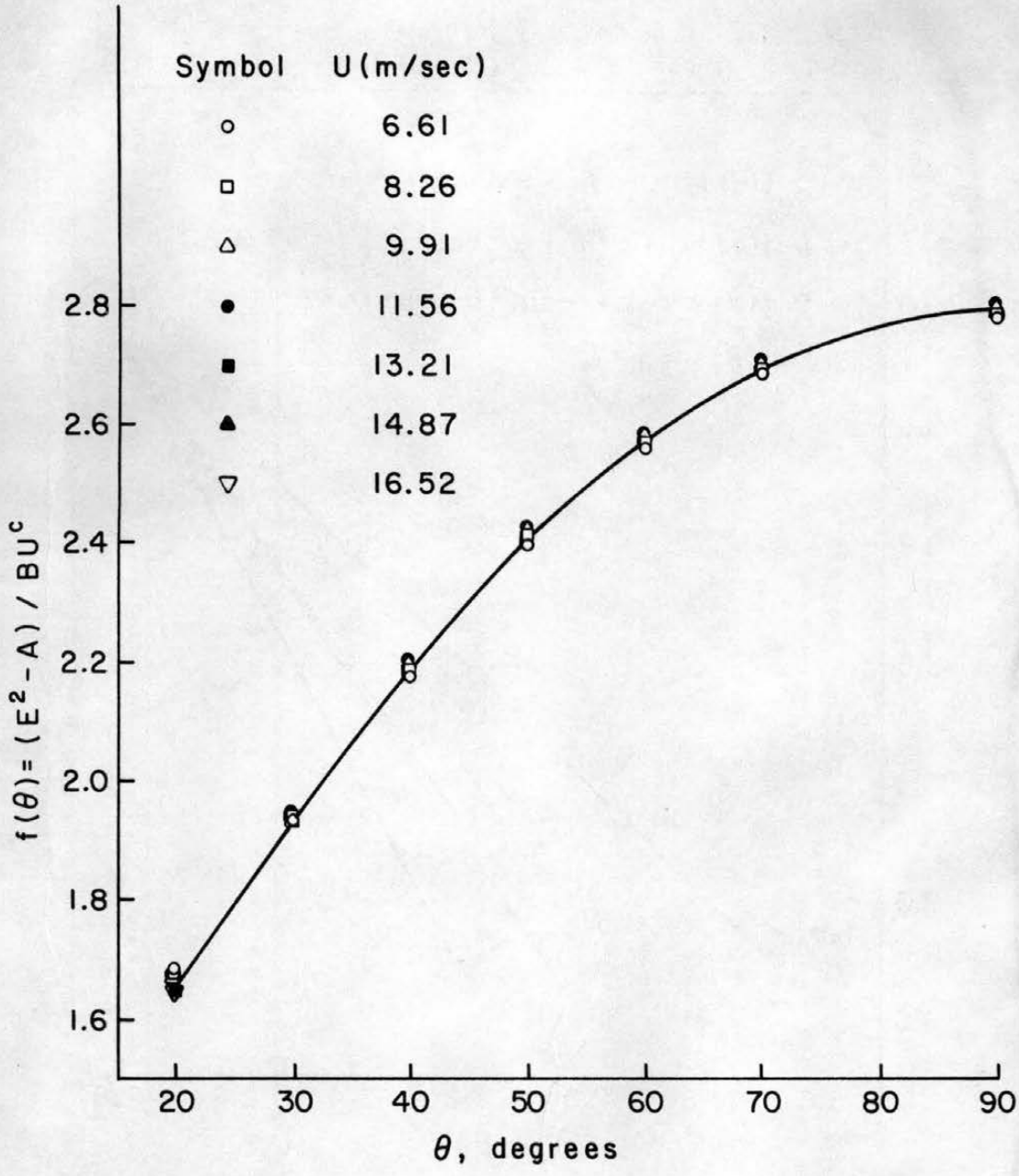

Figure 12. A Typical Rotated Hot-Film Anemometer Calibration.

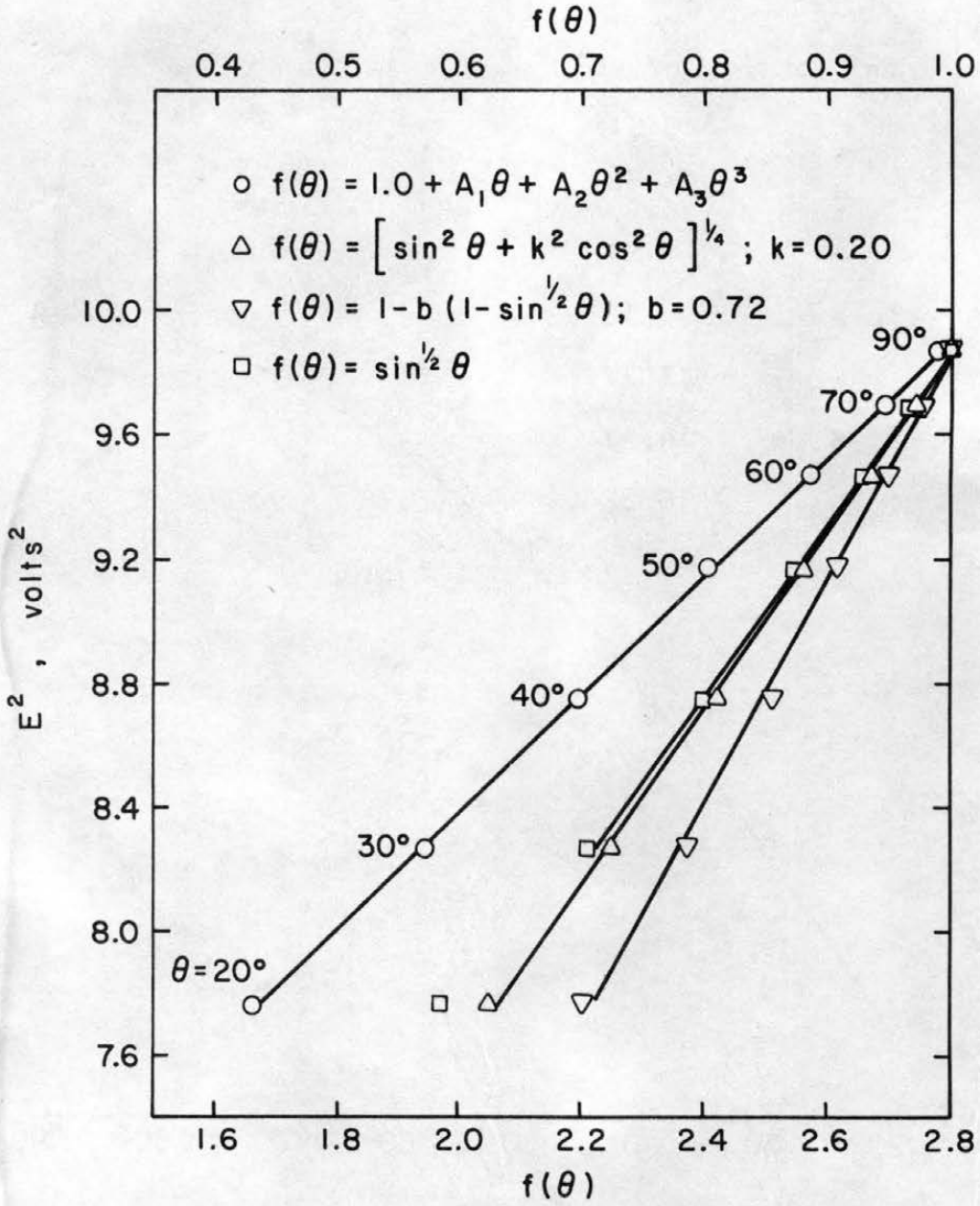

Figure 13. A Typical Graph Indicating the Accuracy of Different Functional Relationships for f(θ).

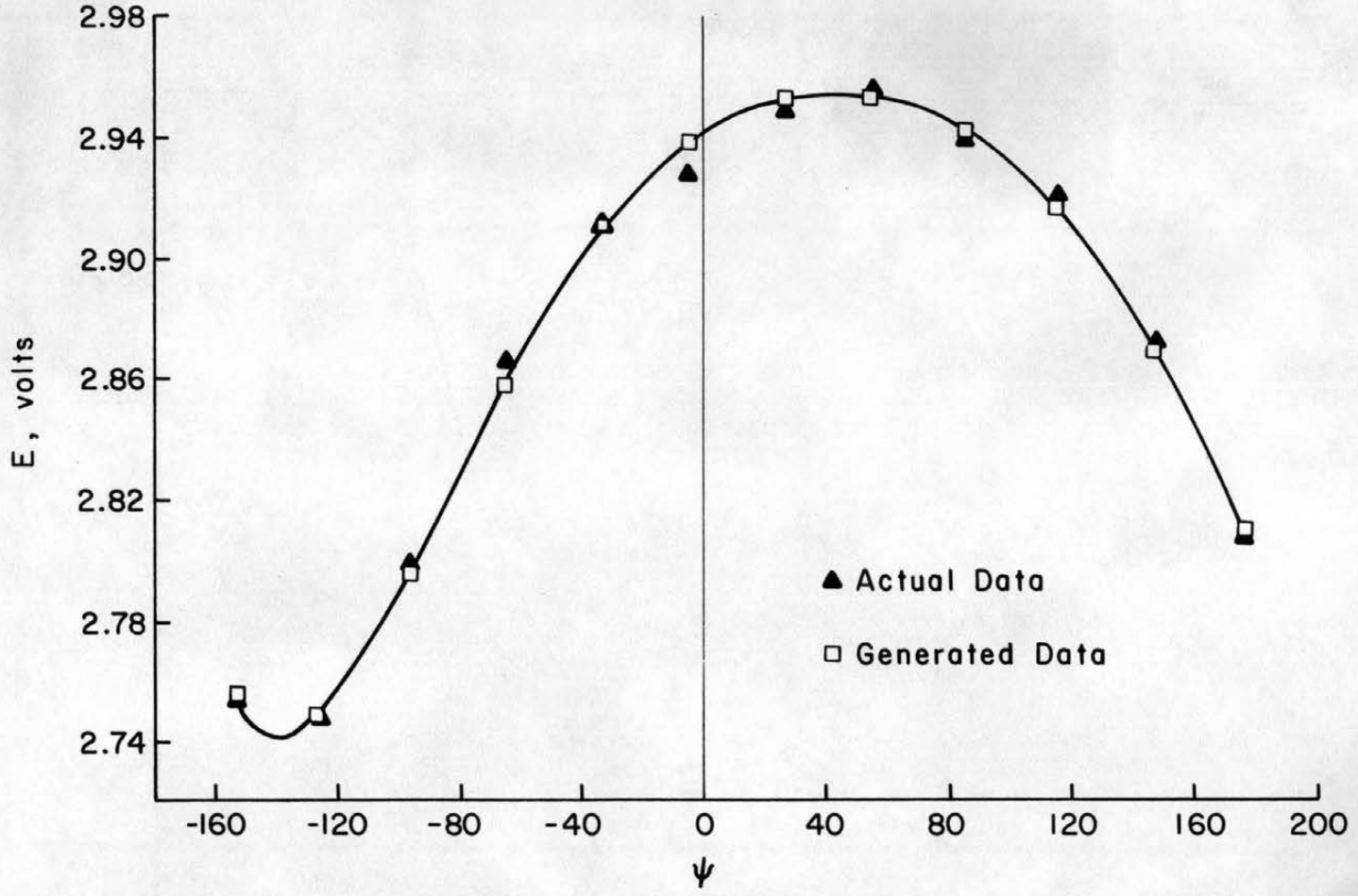

Figure 14. A Typical Curve Showing the Variation in Mean Voltage with Angular Measurement Location.

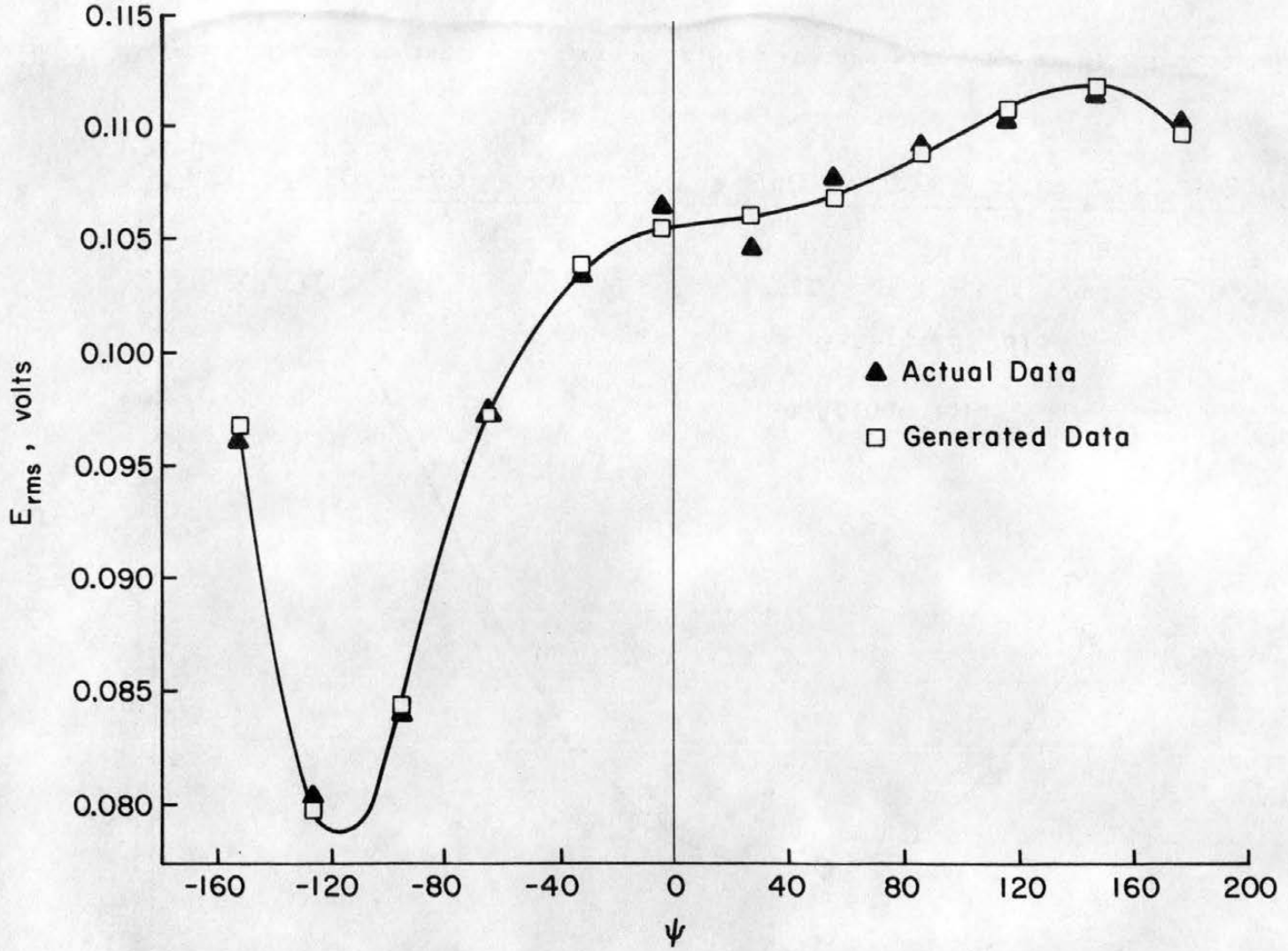

Figure 15. A Typical Curve Showing the Variation in Root-Mean-Square Voltage with Angular Measurement Location.

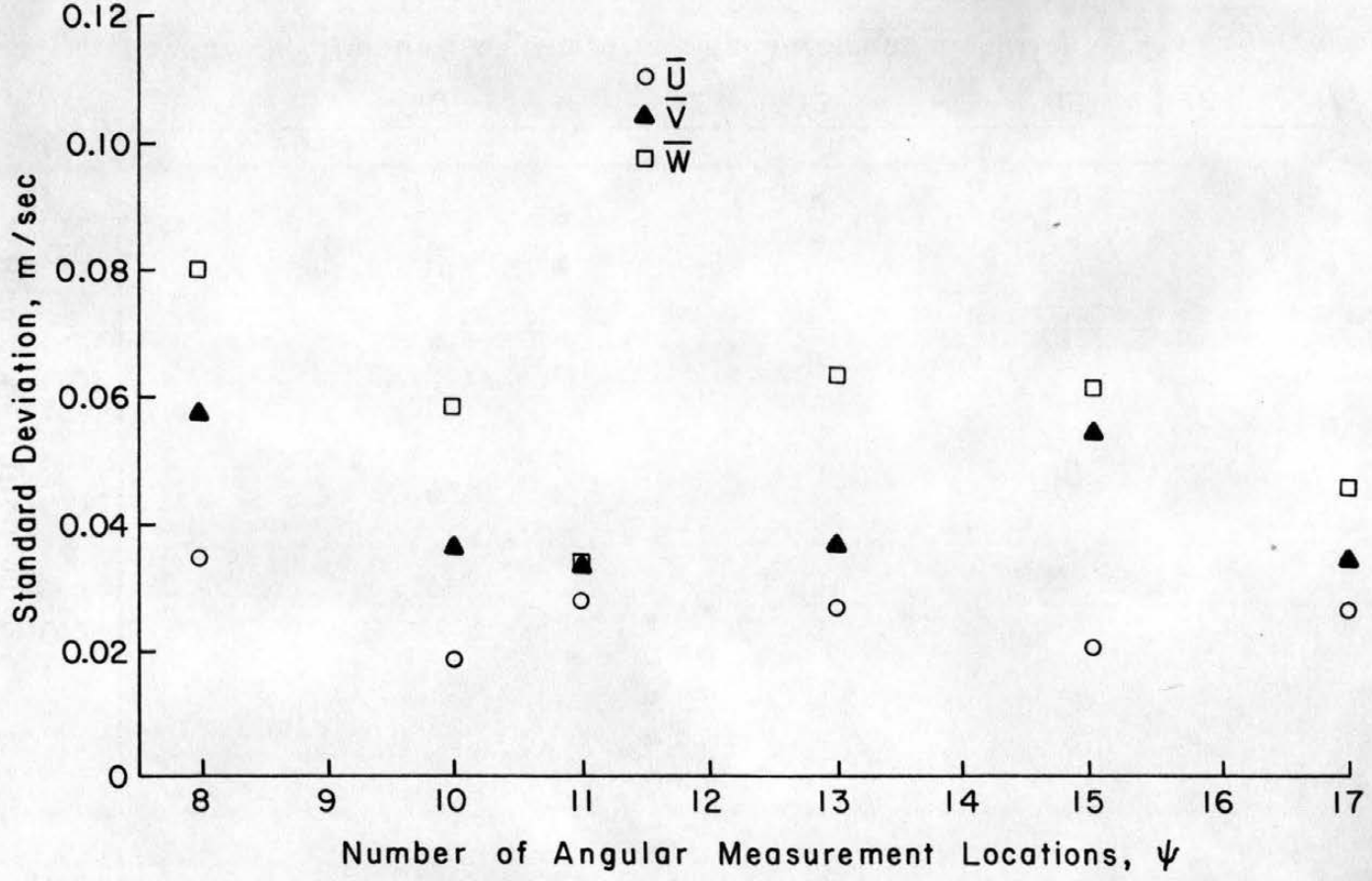

Figure 16. Standard Deviation in the Mean Velocity Components with the Number of Angular Measurement Locations.

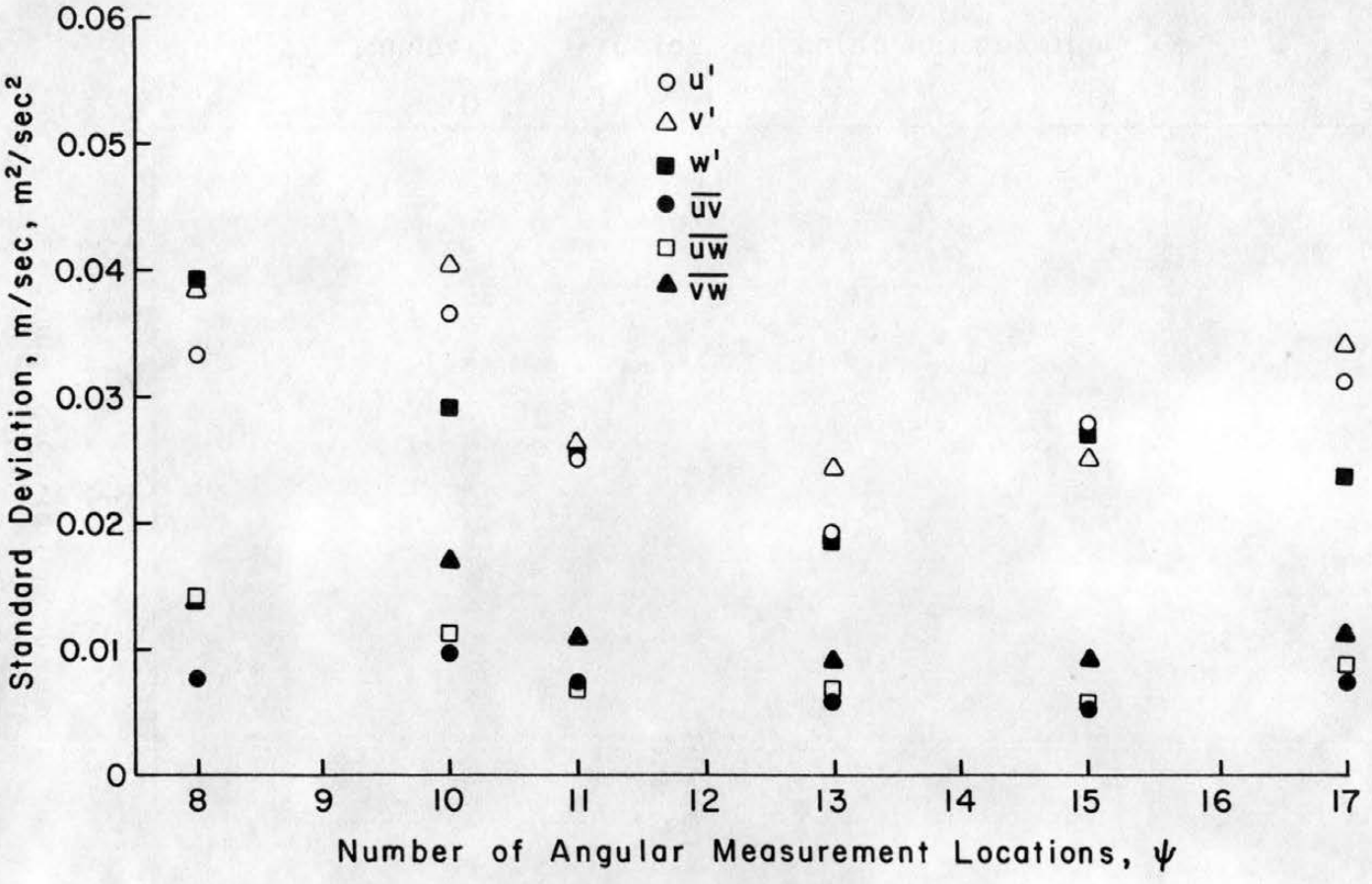

Figure 17. Standard Deviation in the Velocity Correlations with the Number of Angular Measurement Locations.

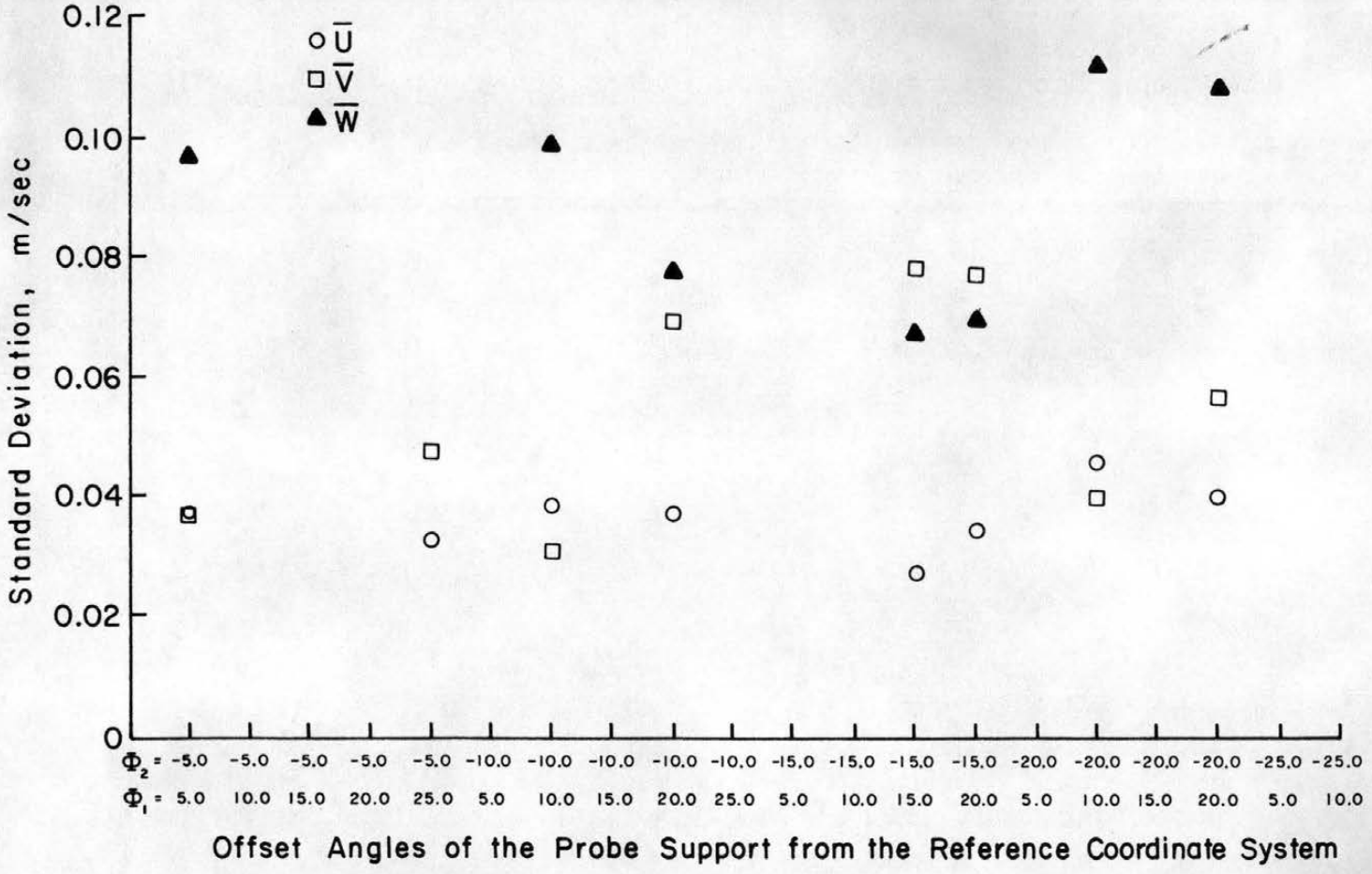

Figure 18. Standard Deviation in the Mean Velocity Components with Various Offset Angles of the Probe Support from the Reference Coordinate System.

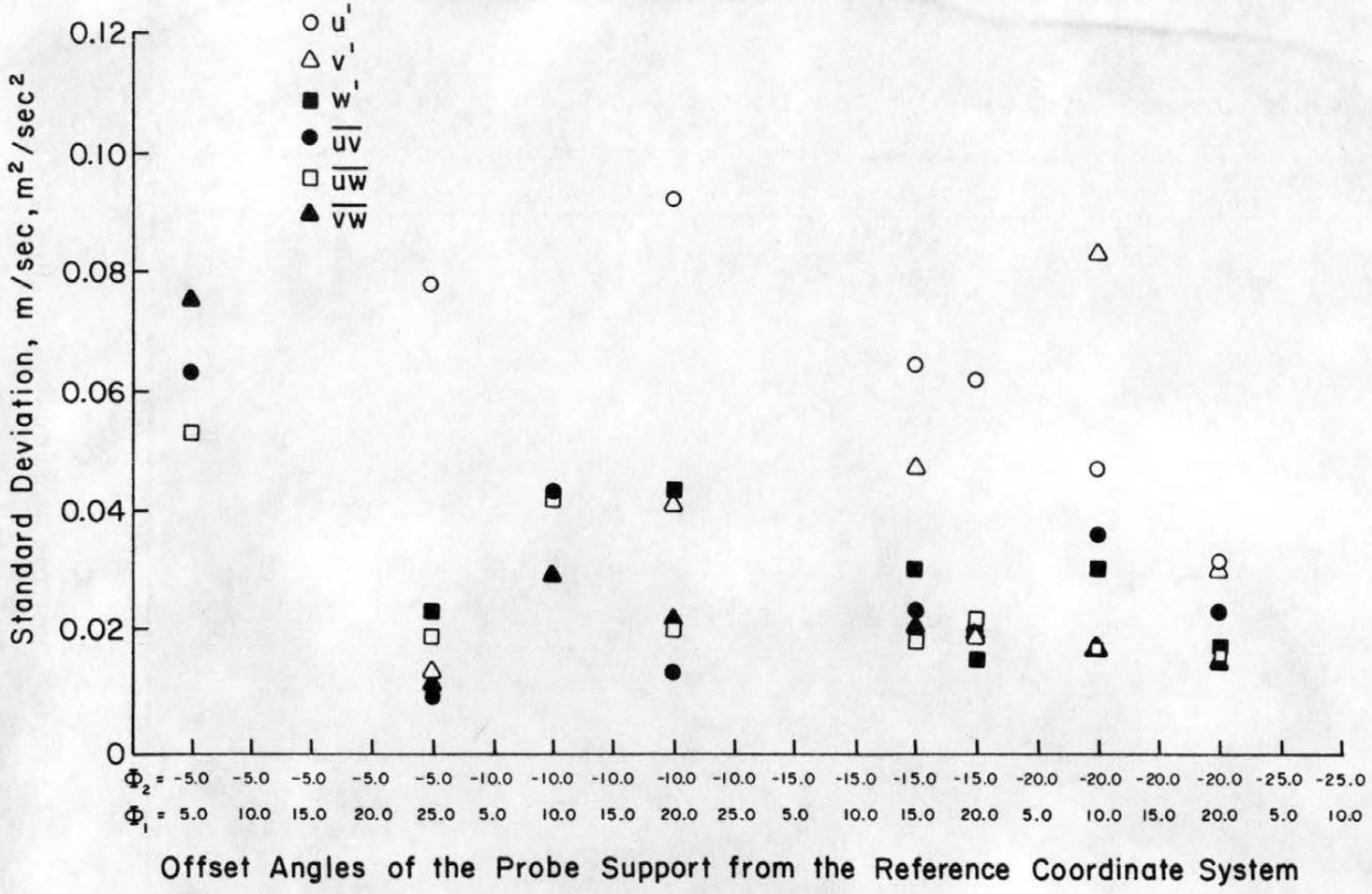

Figure 19. Standard Deviation in the Velocity Correlations with Various Offset Angles of the Probe Support from the Reference Coordinate System.

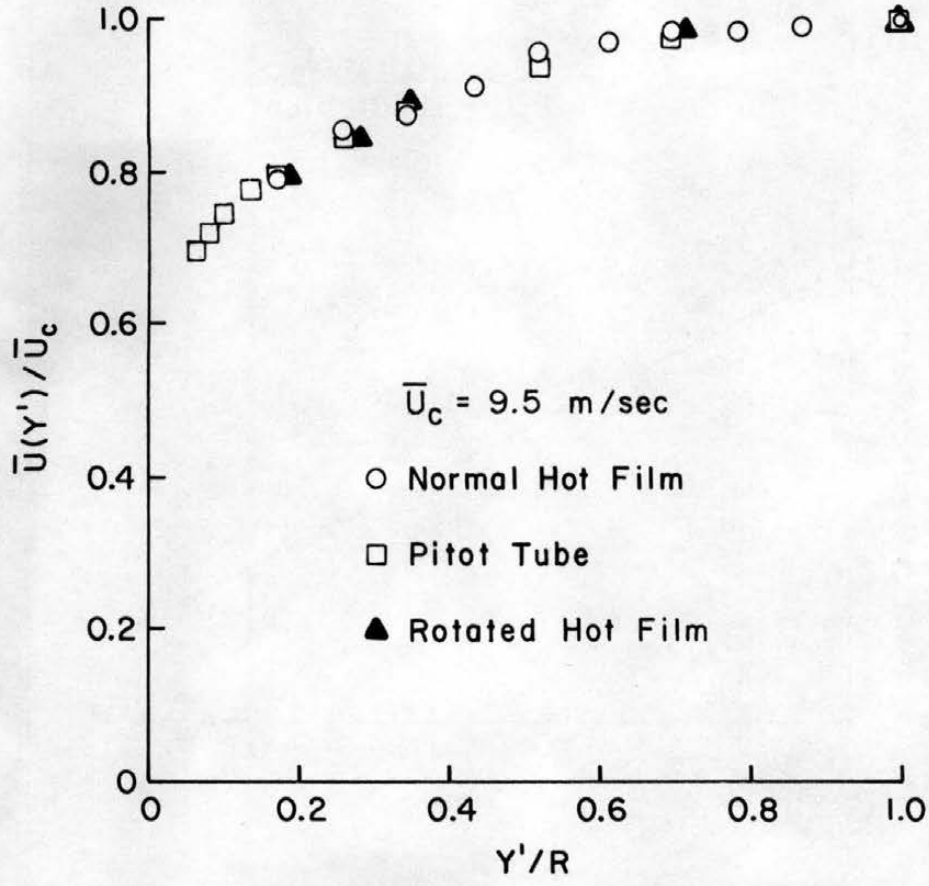

Figure 20. Comparison of the Mean Velocity Profile of the Pipe Flow.

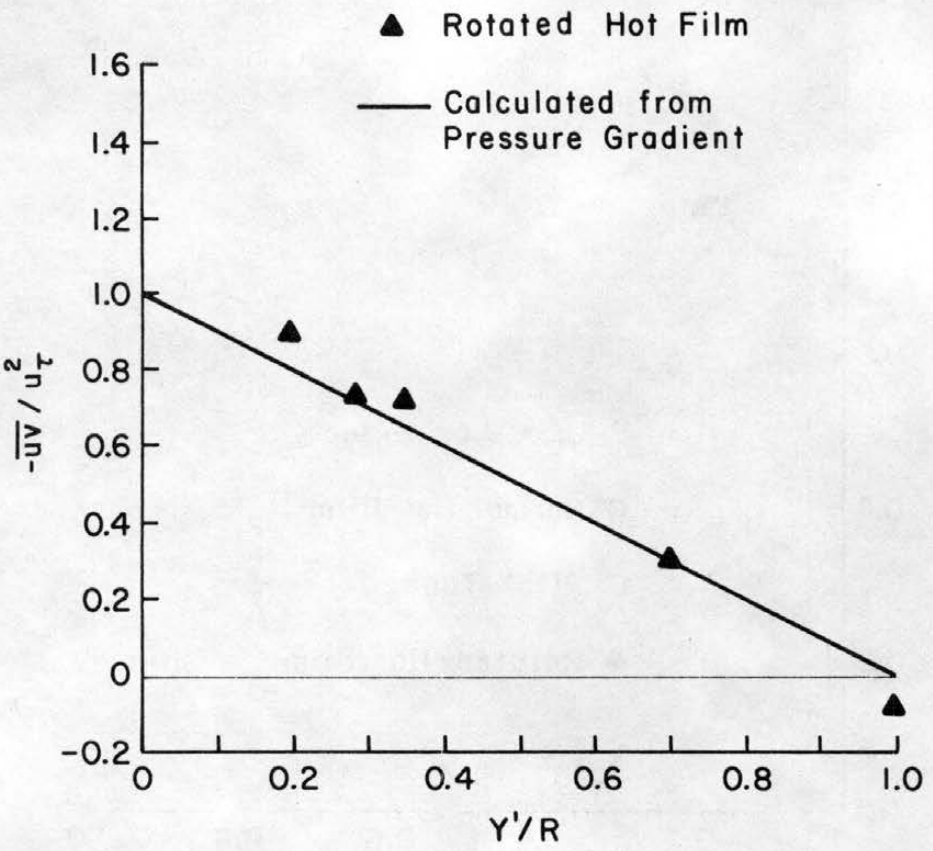

Figure 21. Comparison of the Turbulent Shear Stress Component $\overline{uv}$ Calculated from the Pressure Gradient in the Pipe Flow with the Value Measured with the Rotated Hot-Film Anemometer.

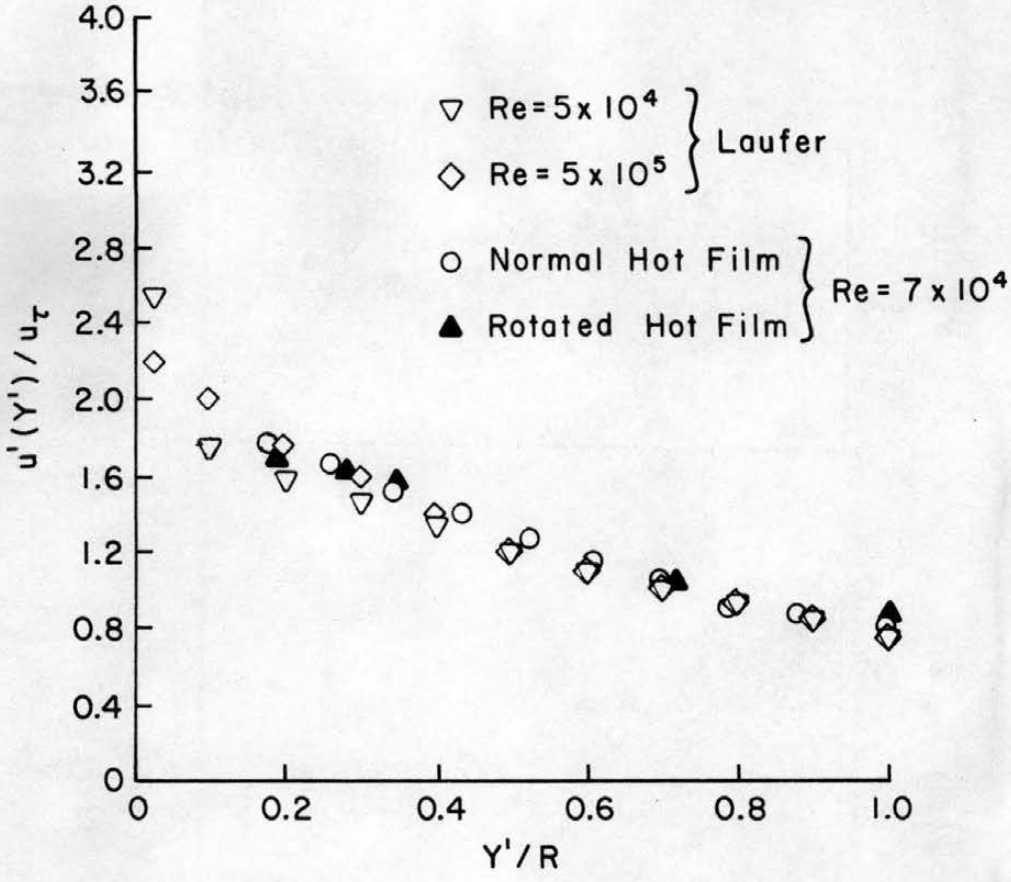

Figure 22. Comparison of the Distribution of the Component of Turbulent Velocity Fluctuation, u', in the Pipe Flow.

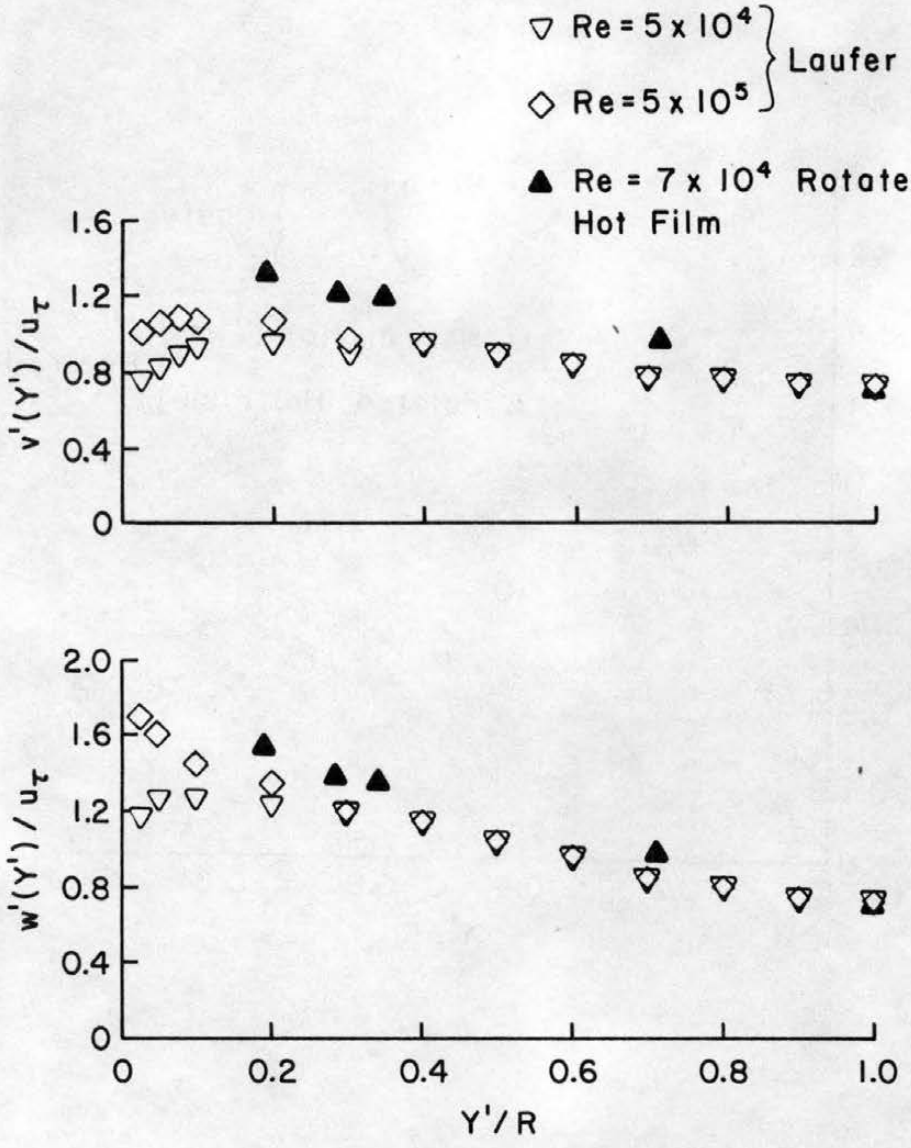

Figure 23. Comparison of the Distribution of the Components of Turbulent Velocity Fluctuation, v' and w', in the Pipe Flow.

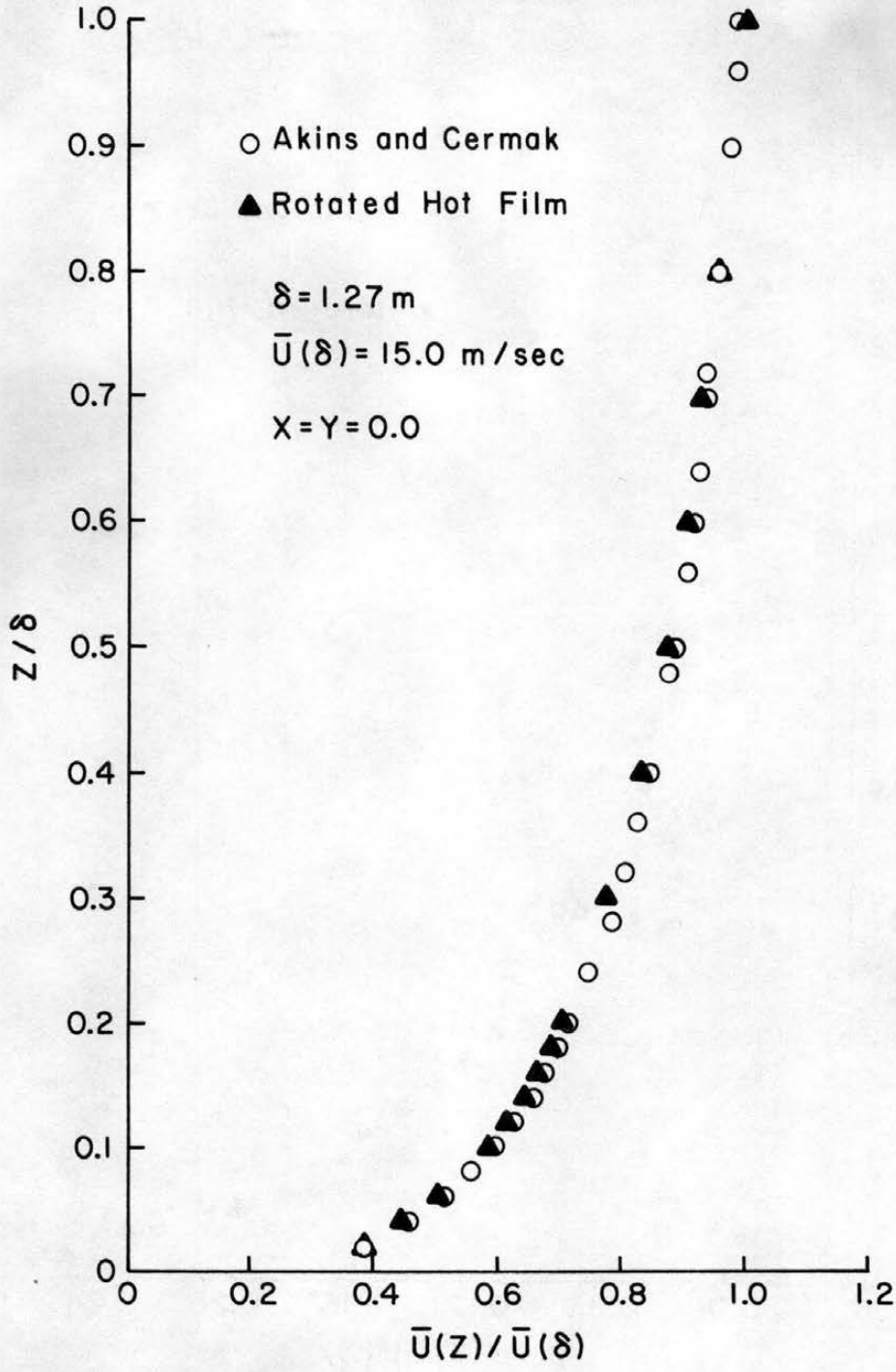

Figure 24. Comparison of the Vertical Mean Velocity Profile in Boundary Layer 2.

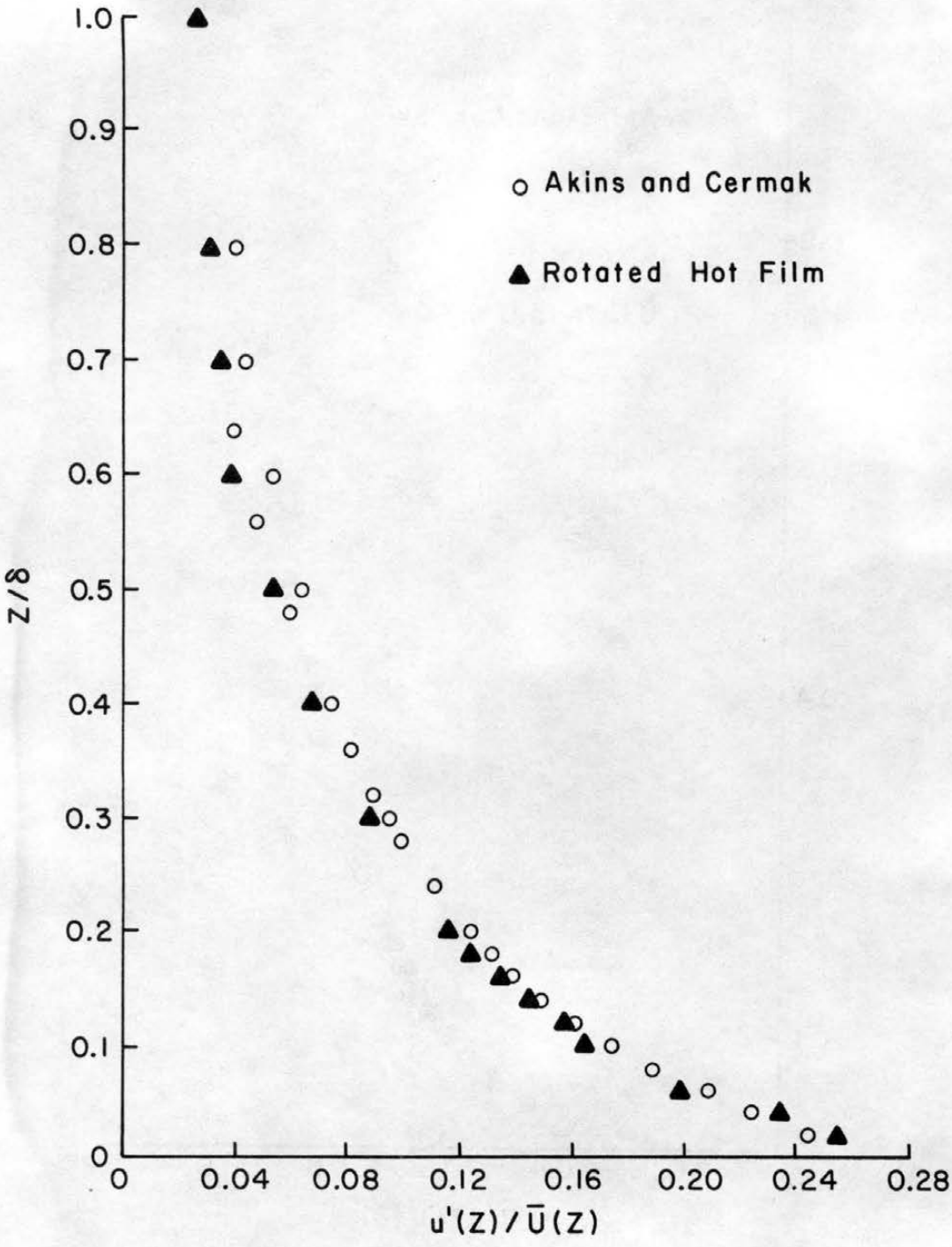

Figure 25a. Comparison of the Vertical Profile of the Component of Turbulent Velocity Fluctuation, u', in Boundary Layer 2.

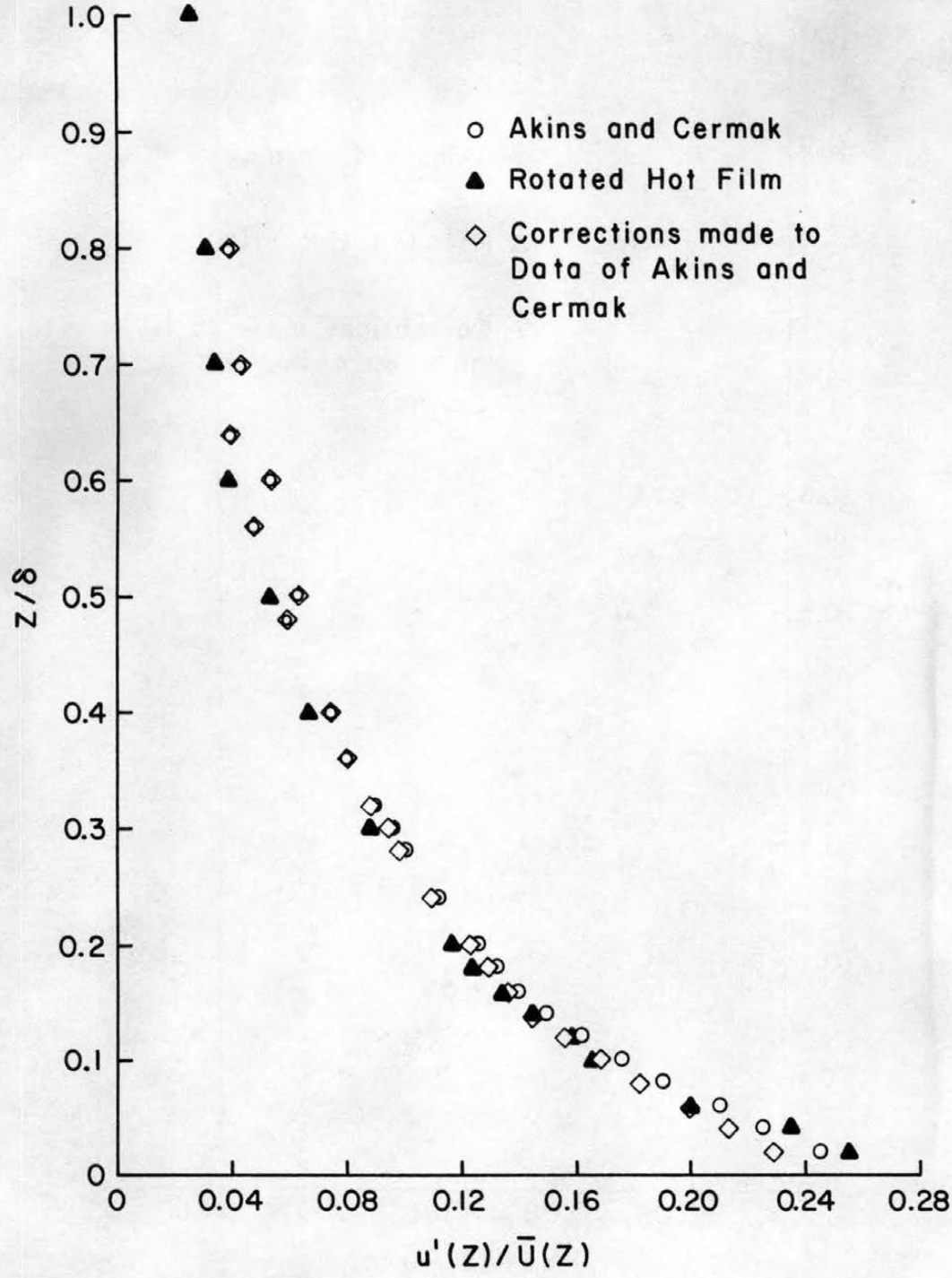

Figure 25b. Comparison of the Vertical Profile of the Component of Turbulent Velocity Fluctuation, u', in Boundary Layer 2 with Hinze's Correction Applied to the Data of Akins and Cermak.

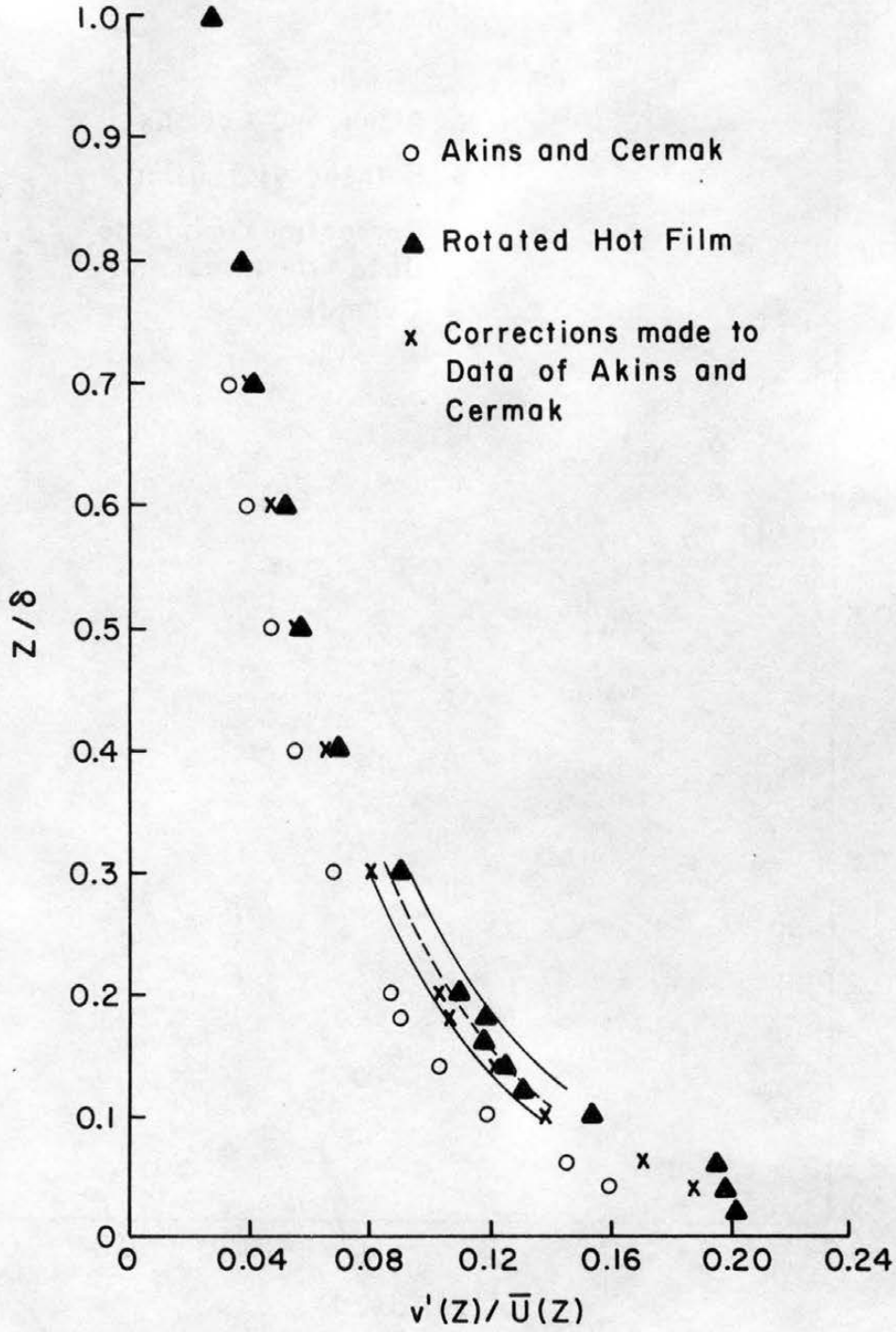

Figure 26. Comparison of the Vertical Profile of the Component of Turbulent Velocity Fluctuation, v', in Boundary Layer 2.

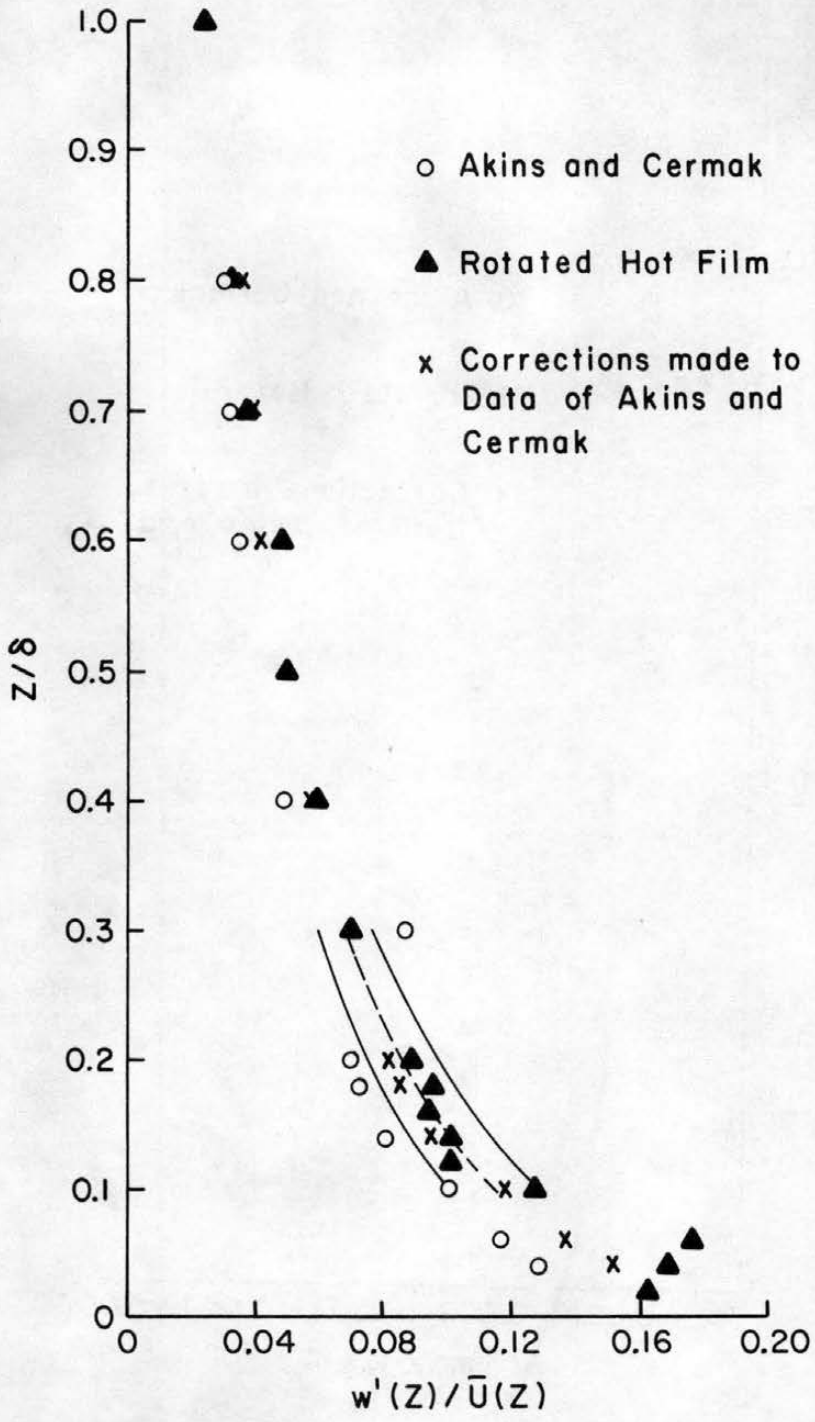

Figure 27. Comparison of the Vertical Profile of the Component of Turbulent Velocity Fluctuation, w', in Boundary Layer 2.

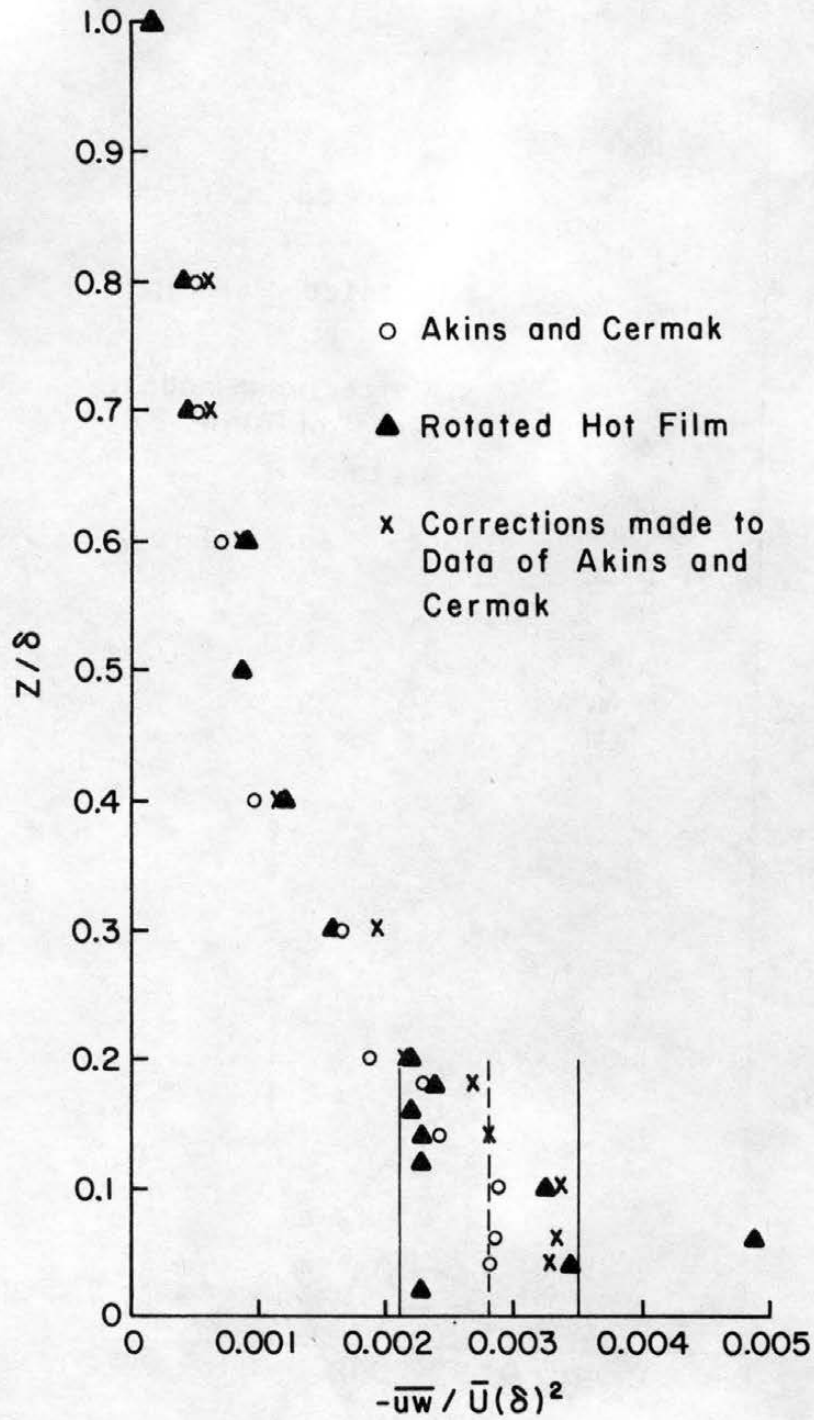

Figure 28. Comparison of the Vertical Profile of the Turbulent Shear Stress Component $\overline{uw}$ in Boundary Layer 2.

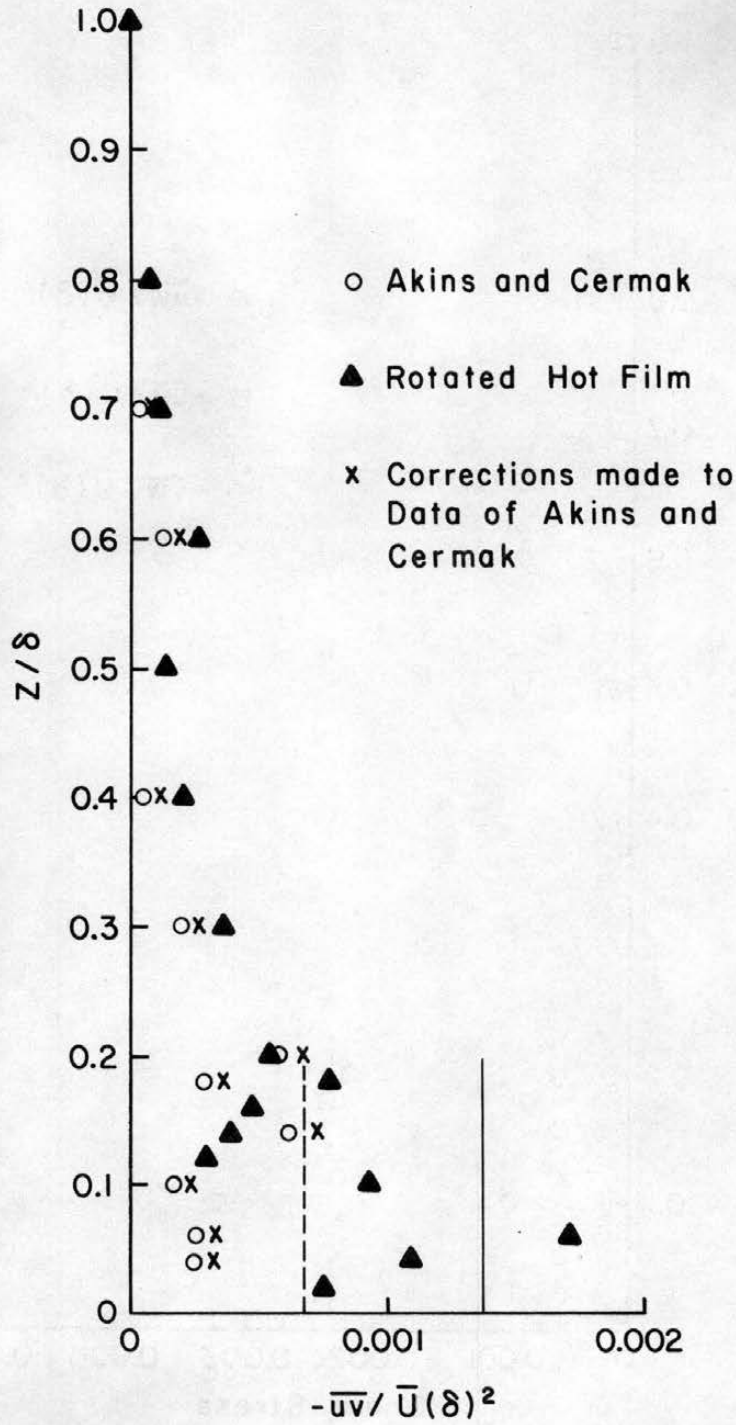

Figure 29. Comparison of the Vertical Profile of the Turbulent Shear Stress Component $\overline{uv}$ in Boundary Layer 2.

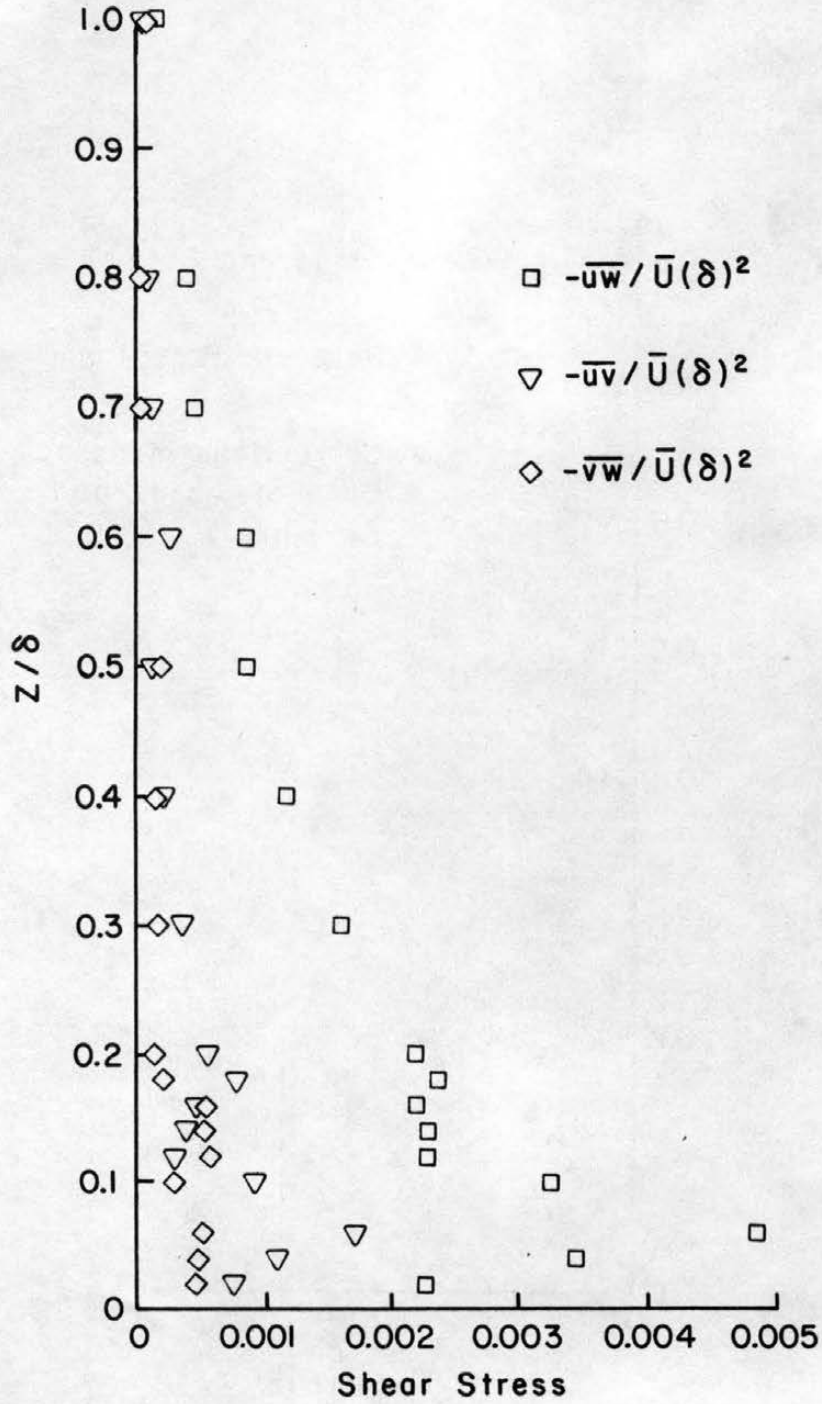

Figure 30. Vertical Profiles of the Turbulent Shear Stress Components $\overline{uw}$, $\overline{uv}$, and $\overline{vw}$ in Boundary Layer 2.

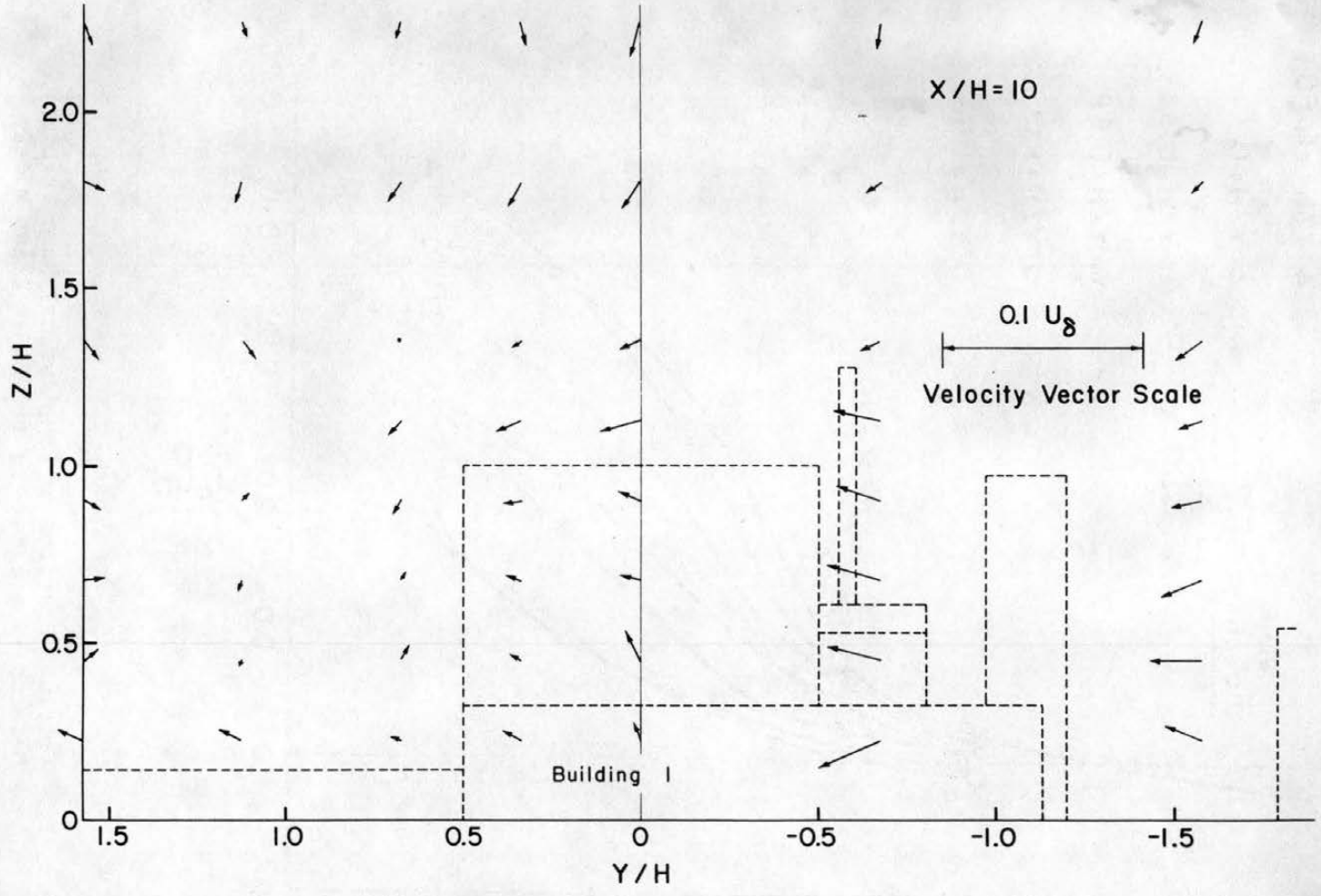

Figure 31. Mean Cross-Flow Velocity Vector Distribution as Seen Looking Downwind Past the Power Plant Model.

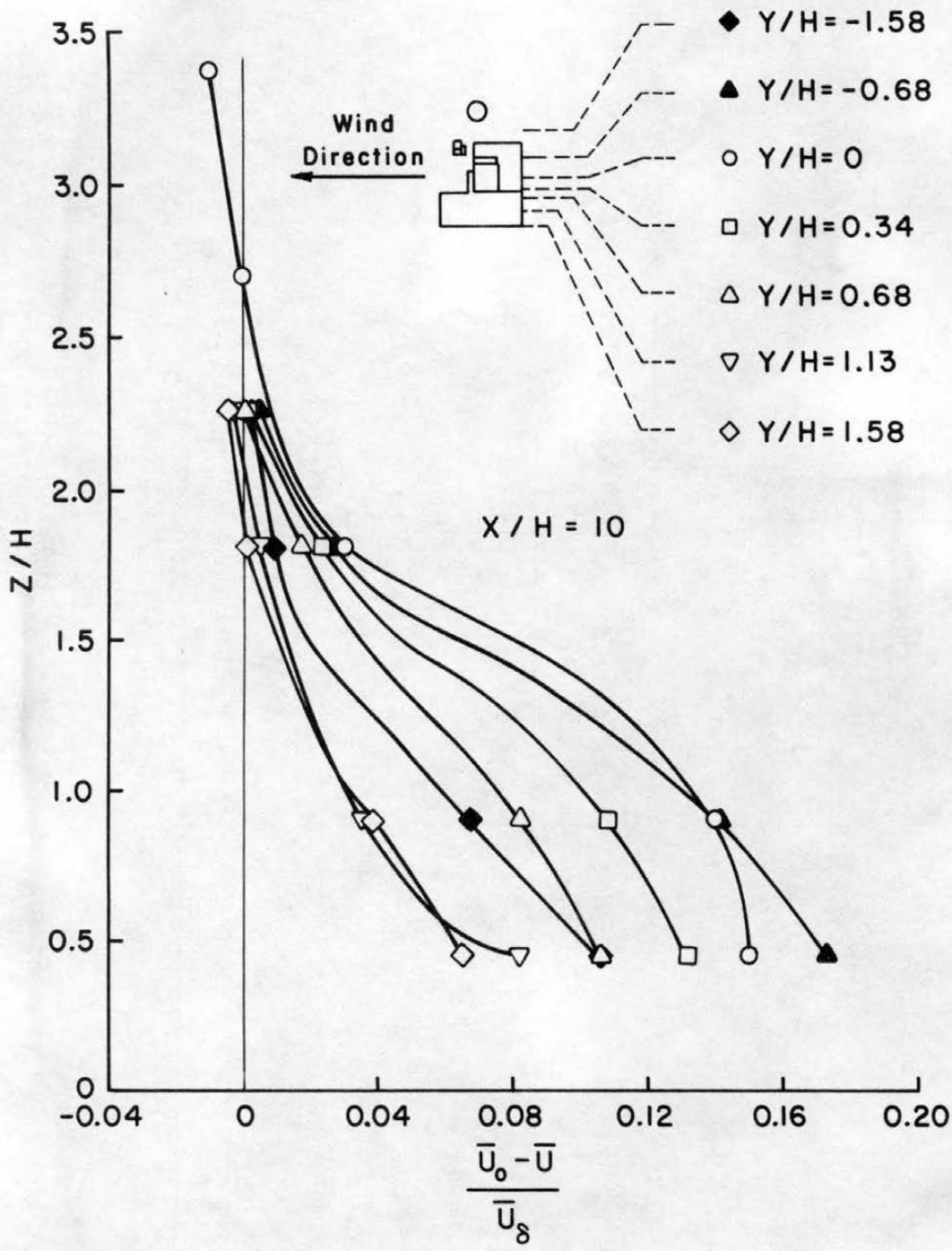

Figure 32. Vertical Profiles of Longitudinal Mean Velocity Defects in the Wake of the Power Plant Model.

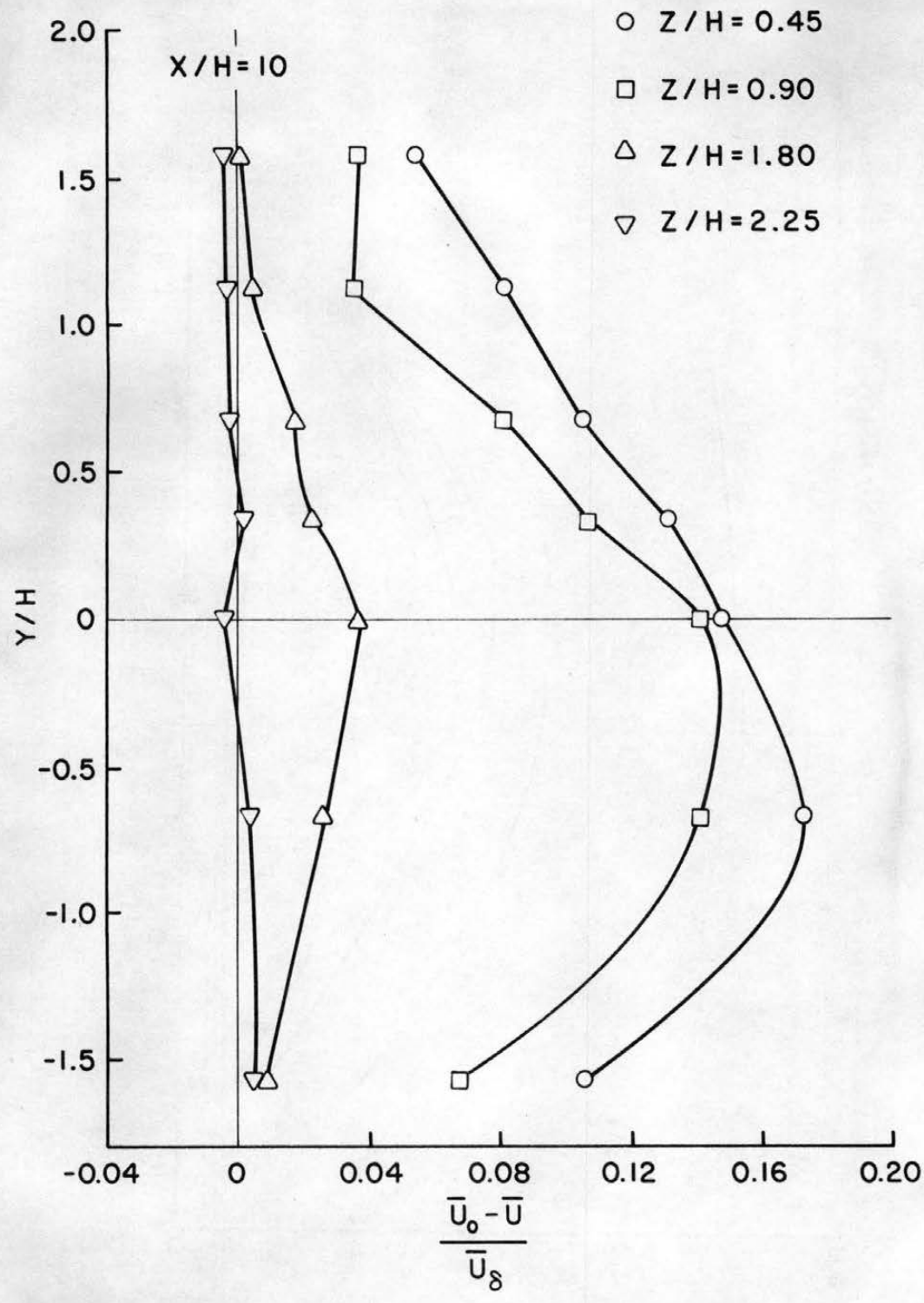

Figure 33. Lateral Profiles of Longitudinal Mean Velocity Defects in the Wake of the Power Plant Model.

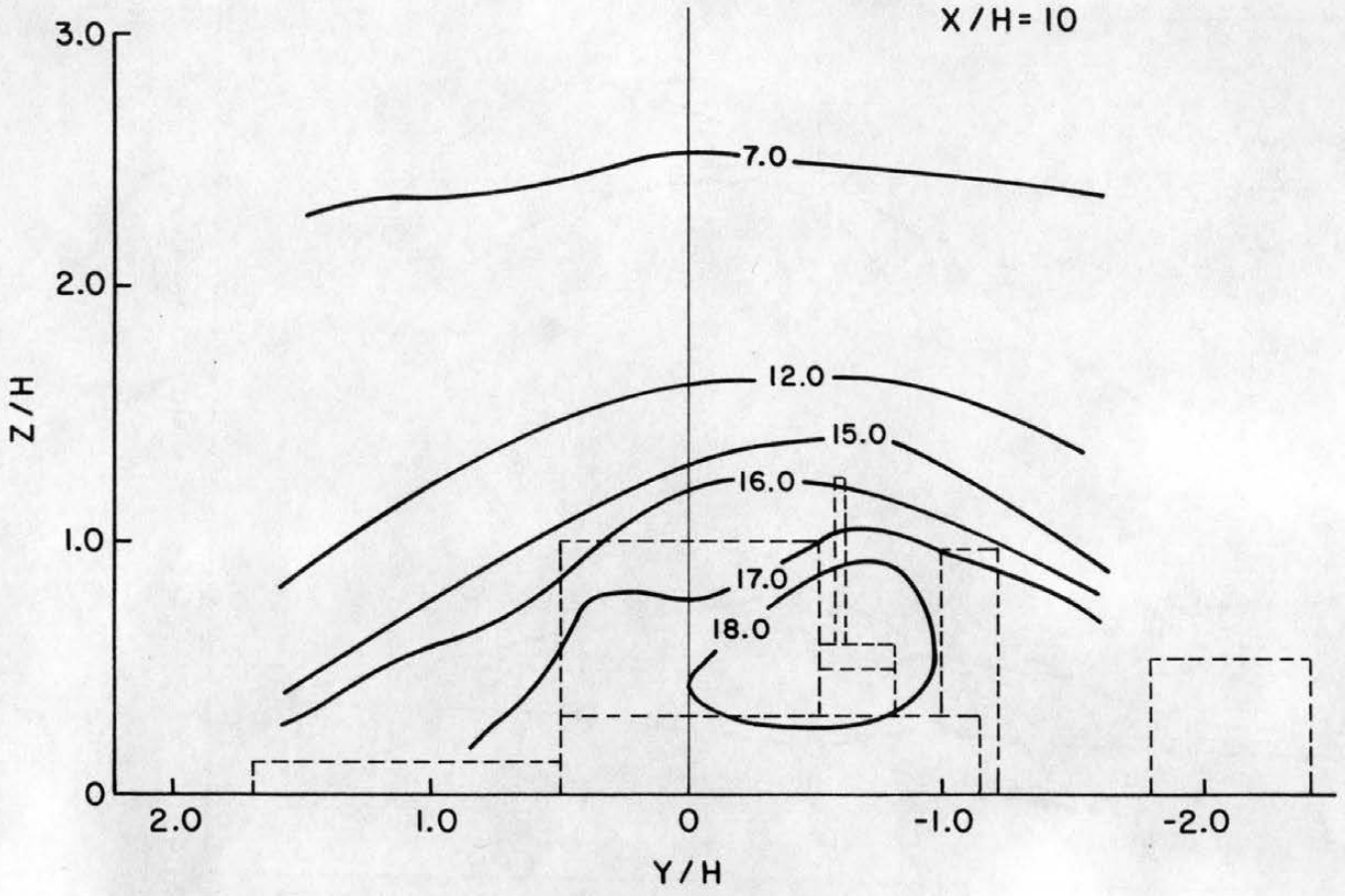

Figure 34. Contours of Longitudinal Turbulence Intensity (percent).

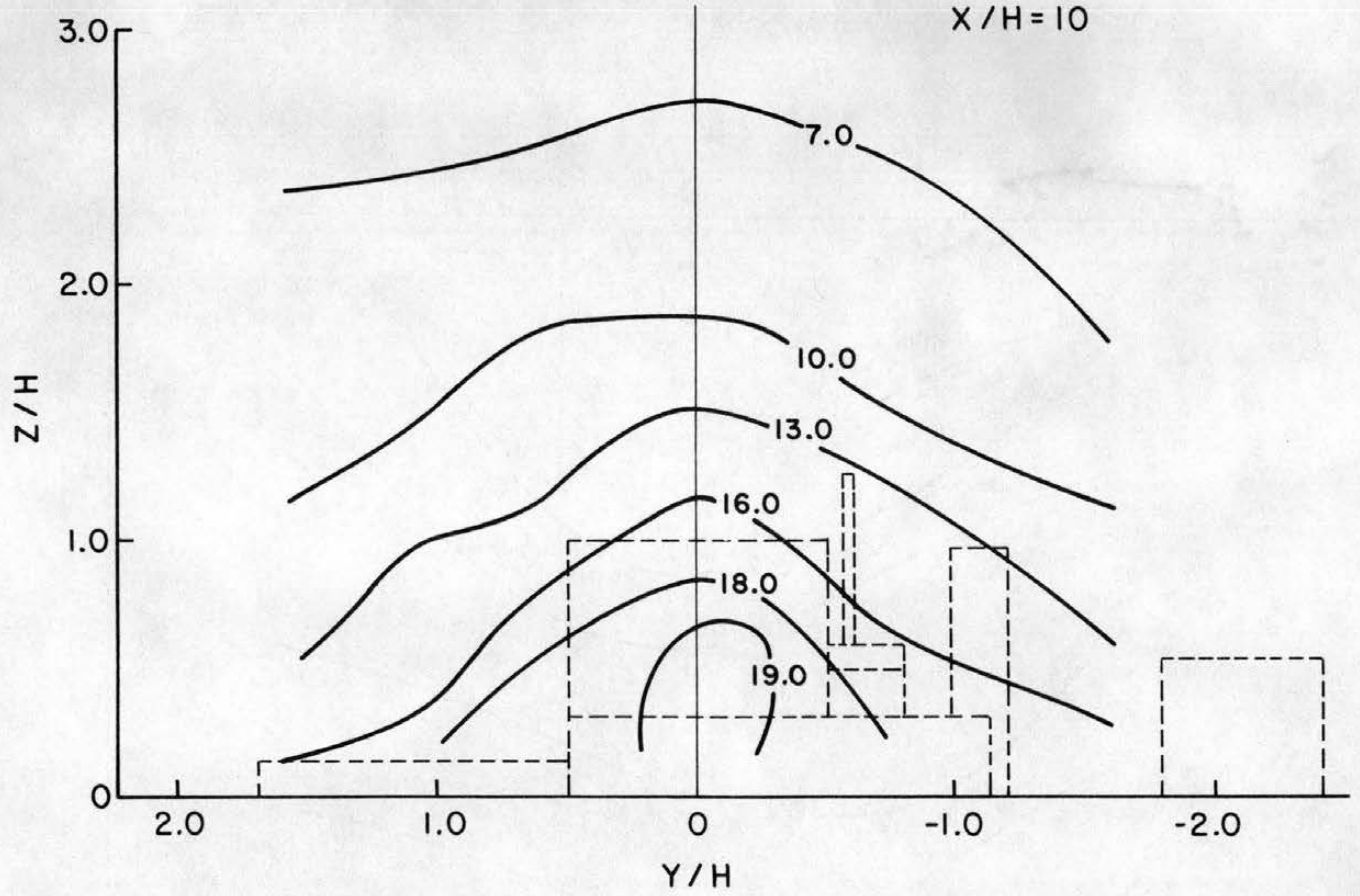

Figure 35. Contours of Lateral Turbulence Intensity (percent).

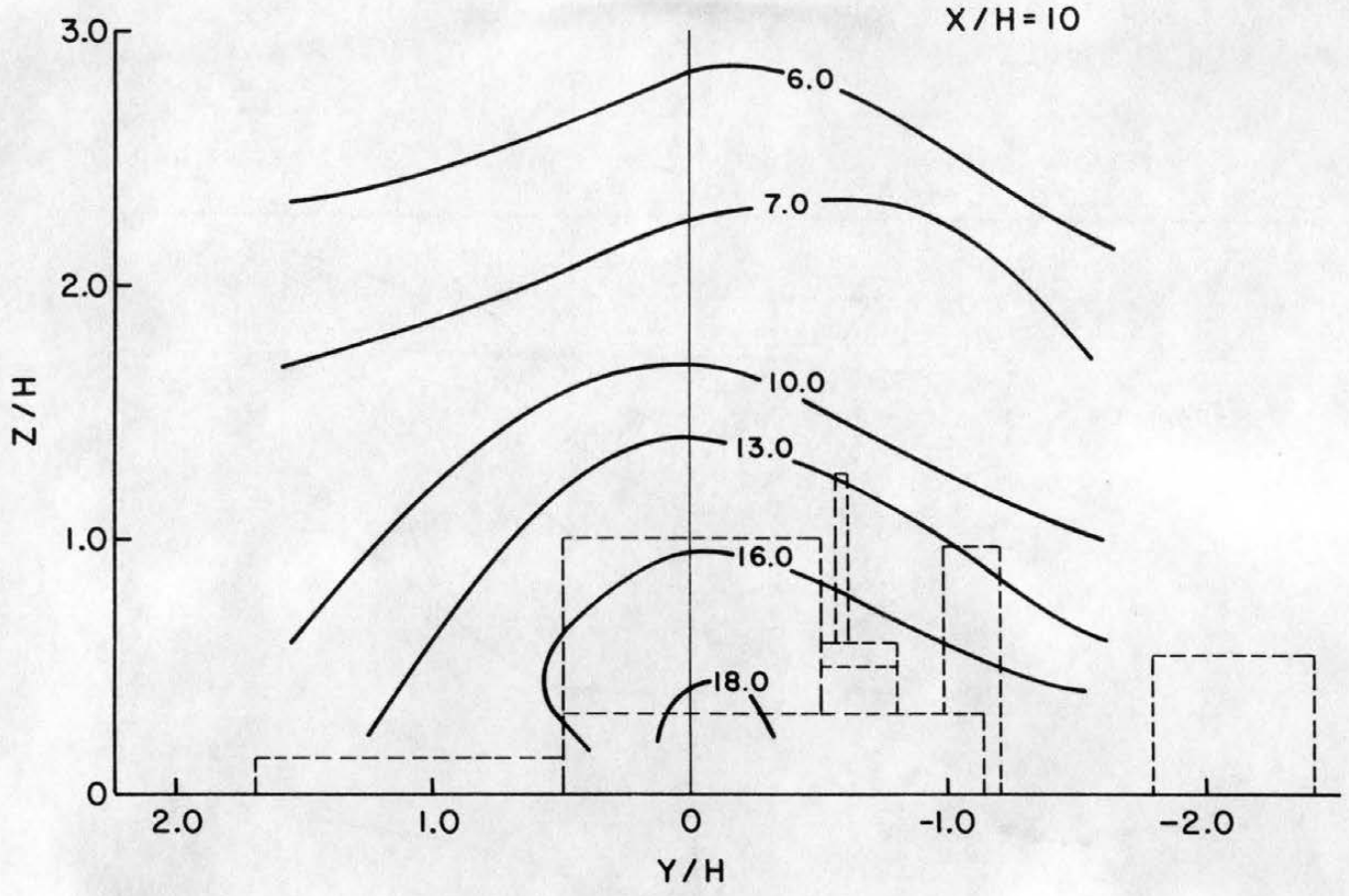

Figure 36. Contours of Vertical Turbulence Intensity (percent).

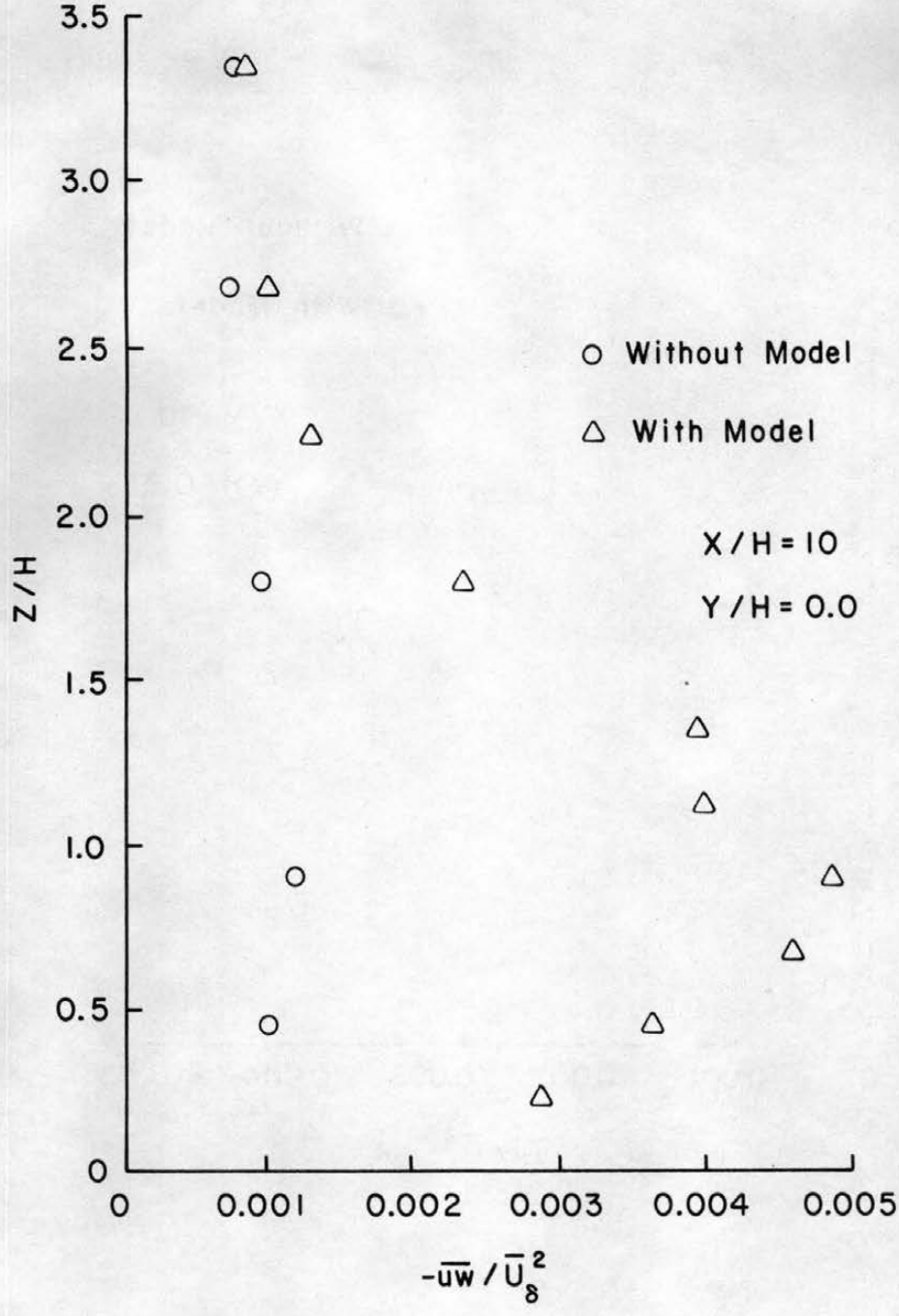

Figure 37a. Vertical Profile of the Turbulent Shear Stress Component $\overline{uw}$ in the Wake of the Power Plant Model. Y/H = 0.0.

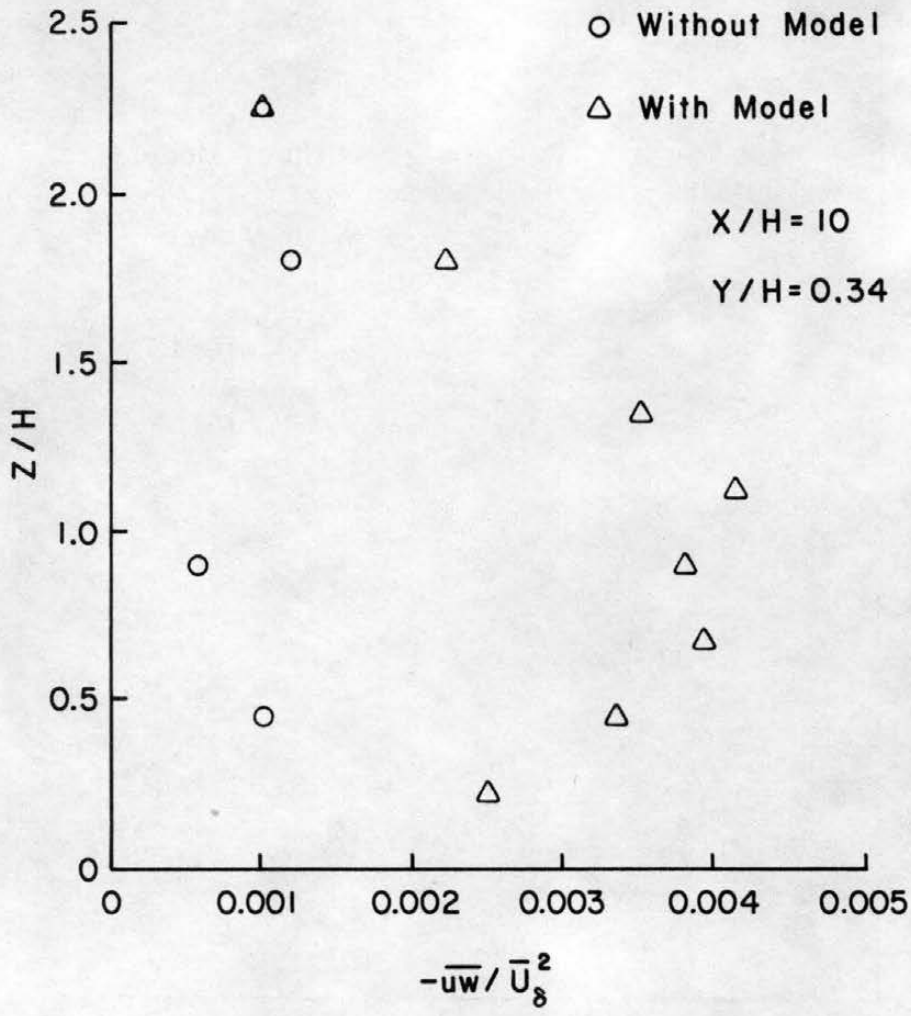

Figure 37b. Y/H = 0.34.

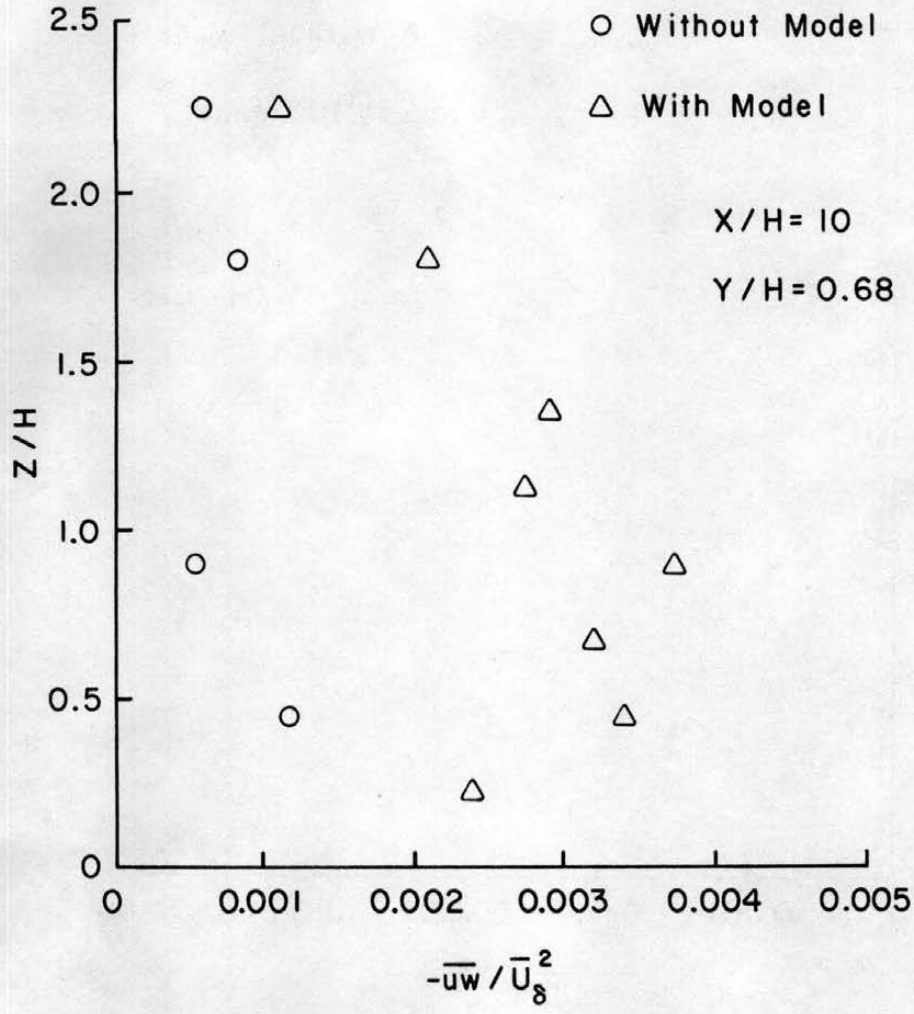

Figure 37c. Y/H = 0.68.

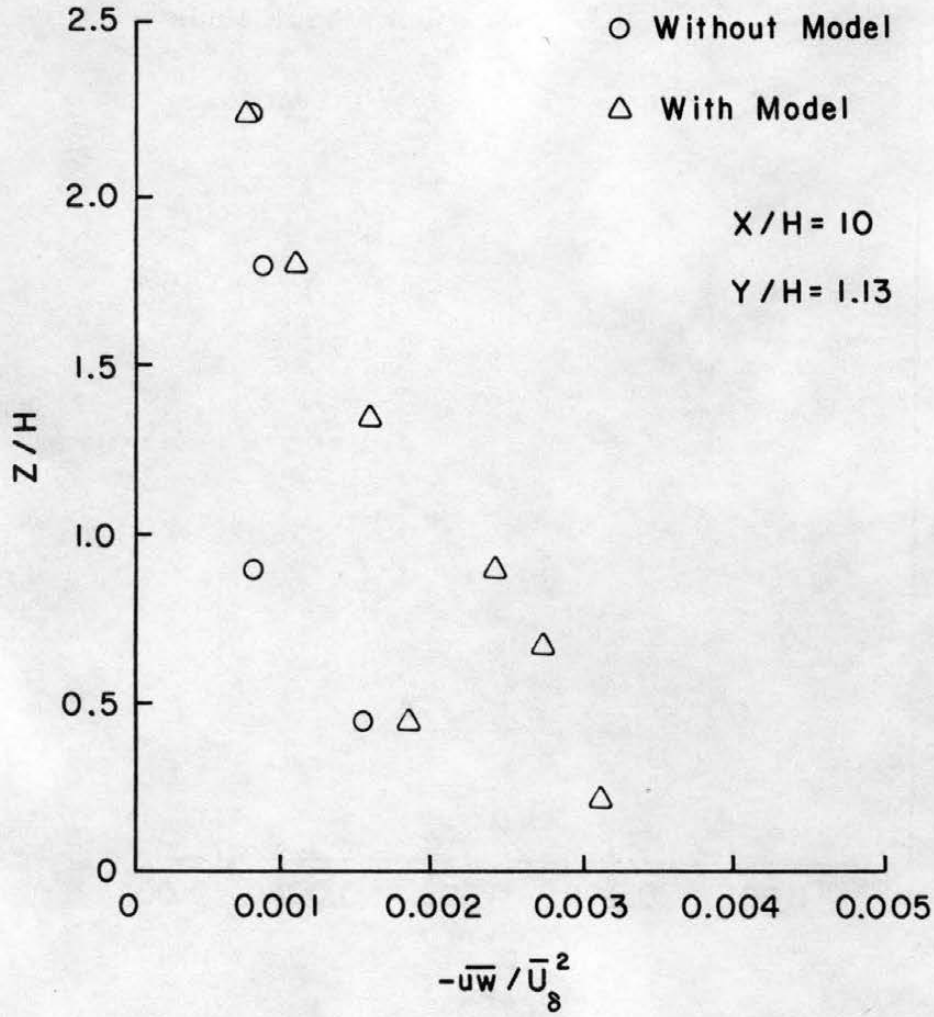

Figure 37d. Y/H = 1.13.

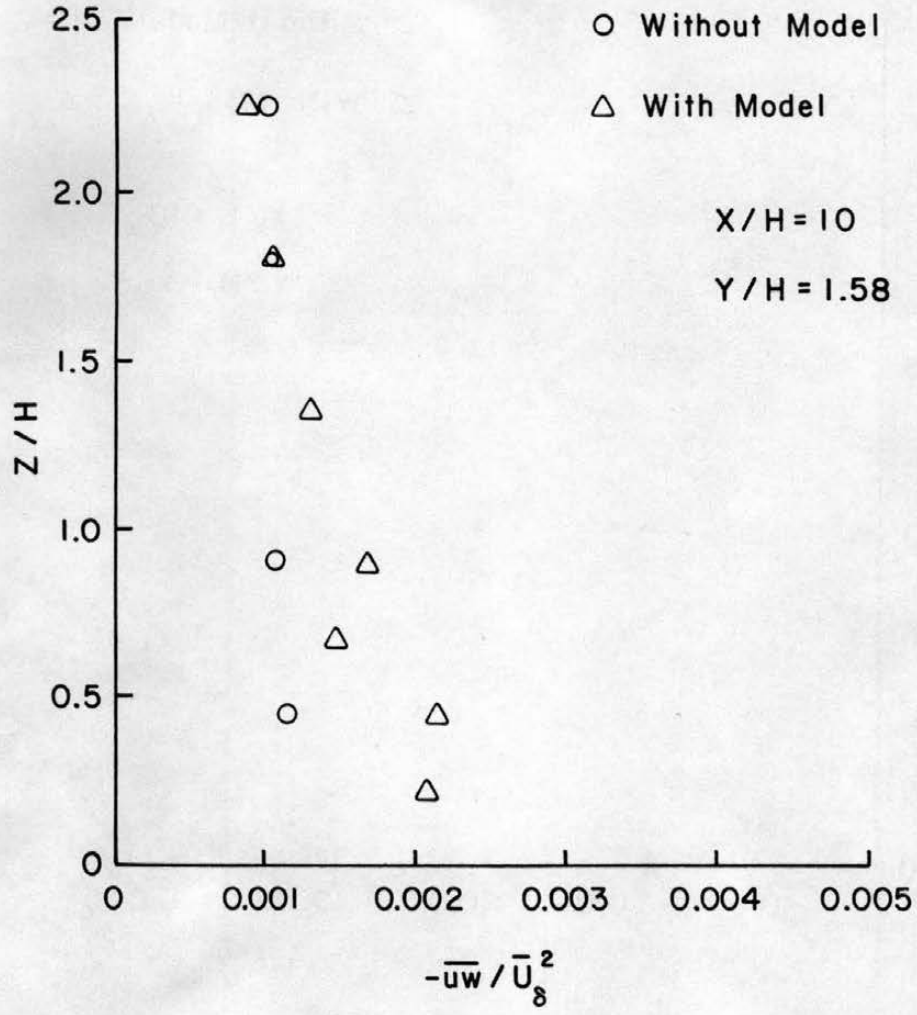

Figure 37e. Y/H = 1.58.

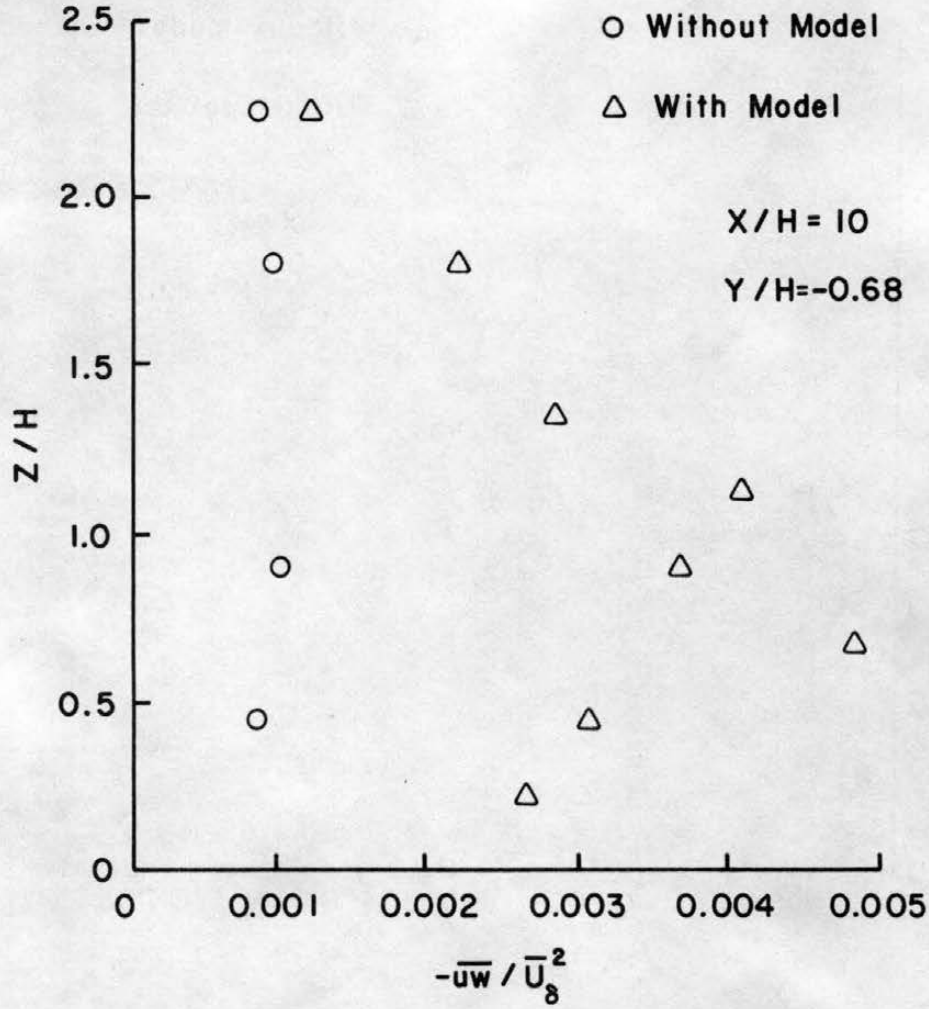

Figure 37f. Y/H = -0.68.

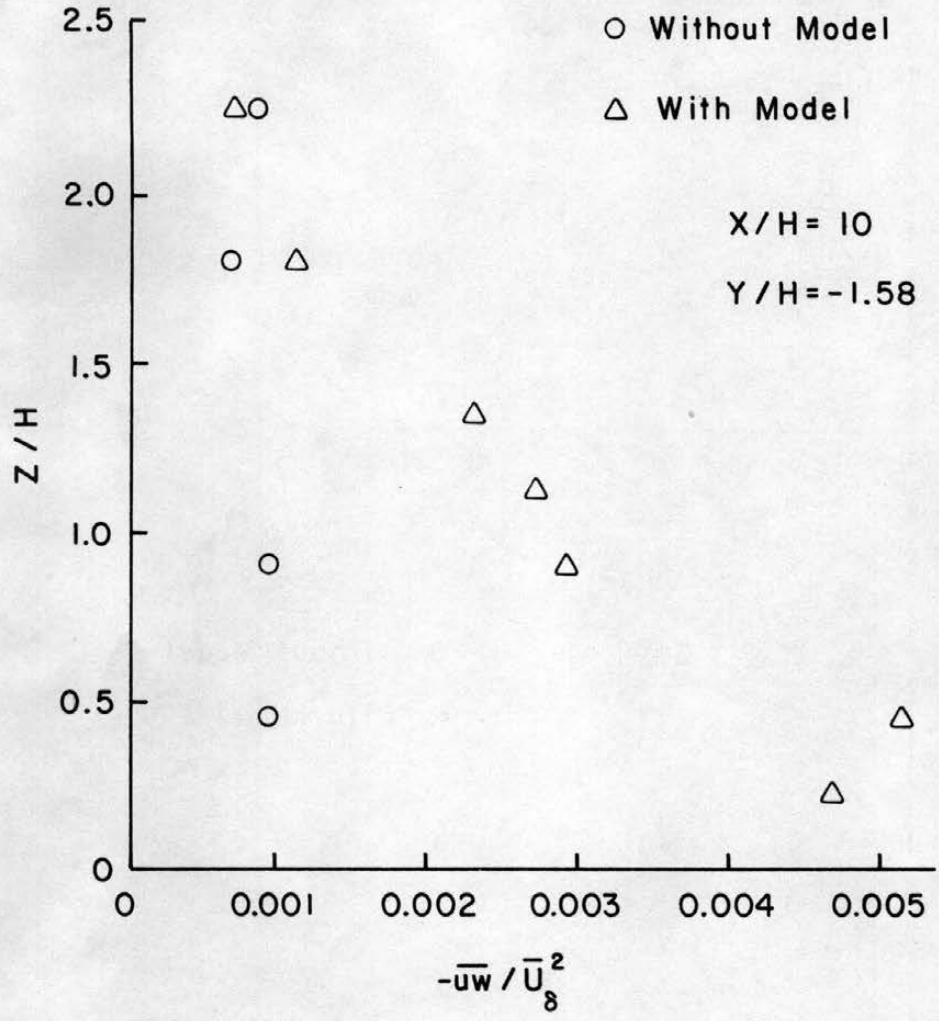

Figure 37g. Y/H = -1.58.

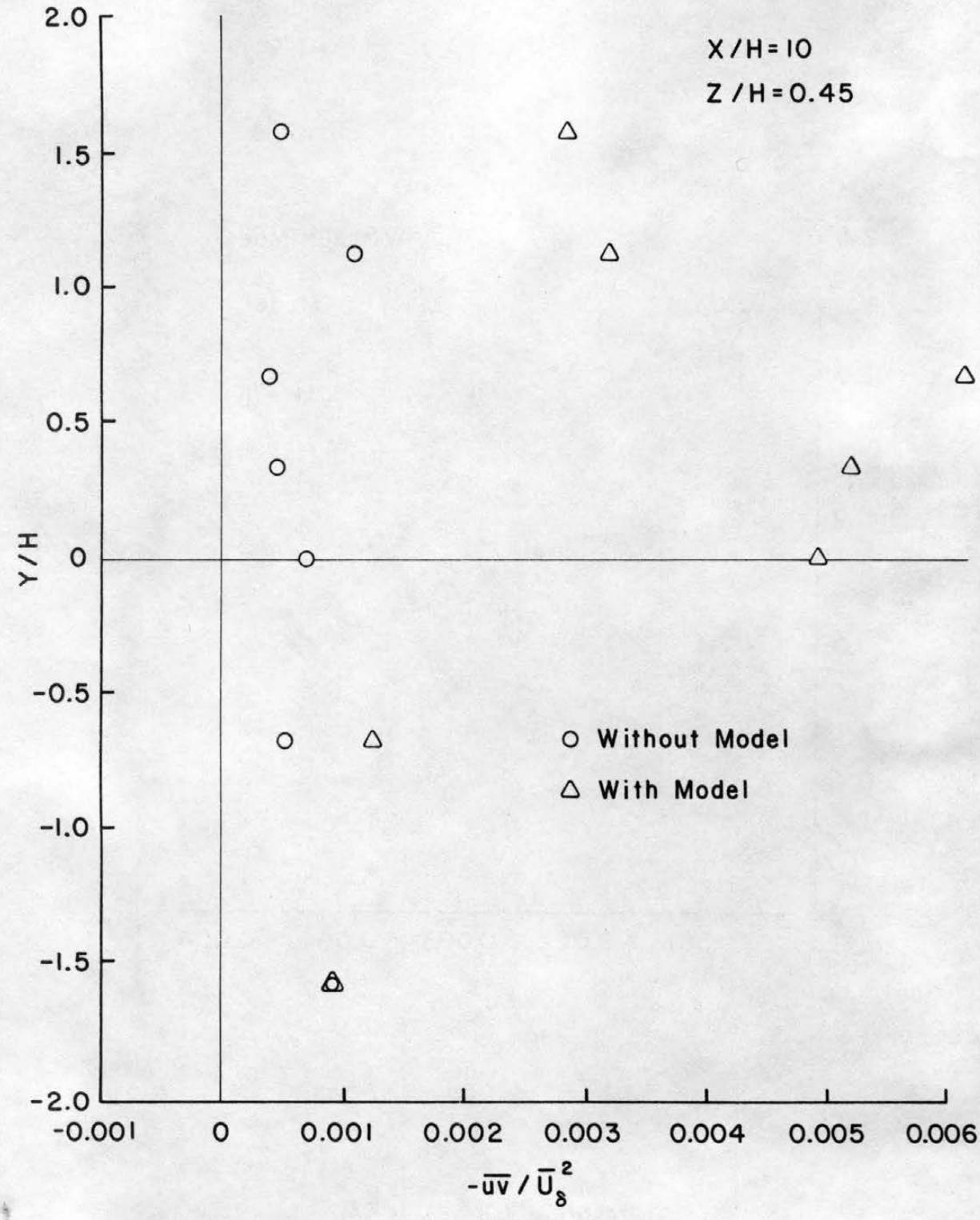

Figure 38a. Lateral Profile of the Turbulent Shear Stress Component $\overline{uv}$ in the Wake of the Power Plant Model. Z/H = 0.45.

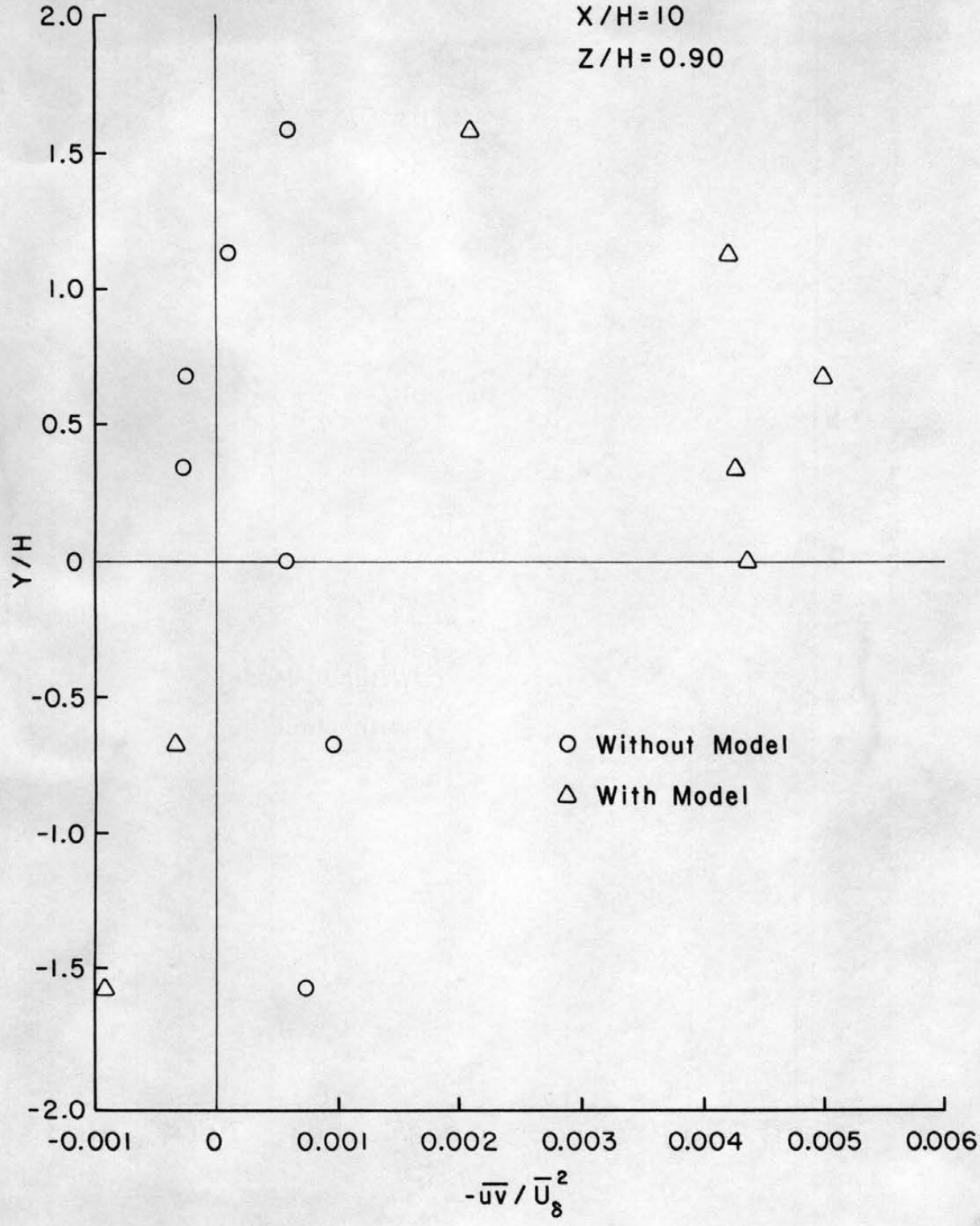

Figure 38b. Z/H = 0.90.

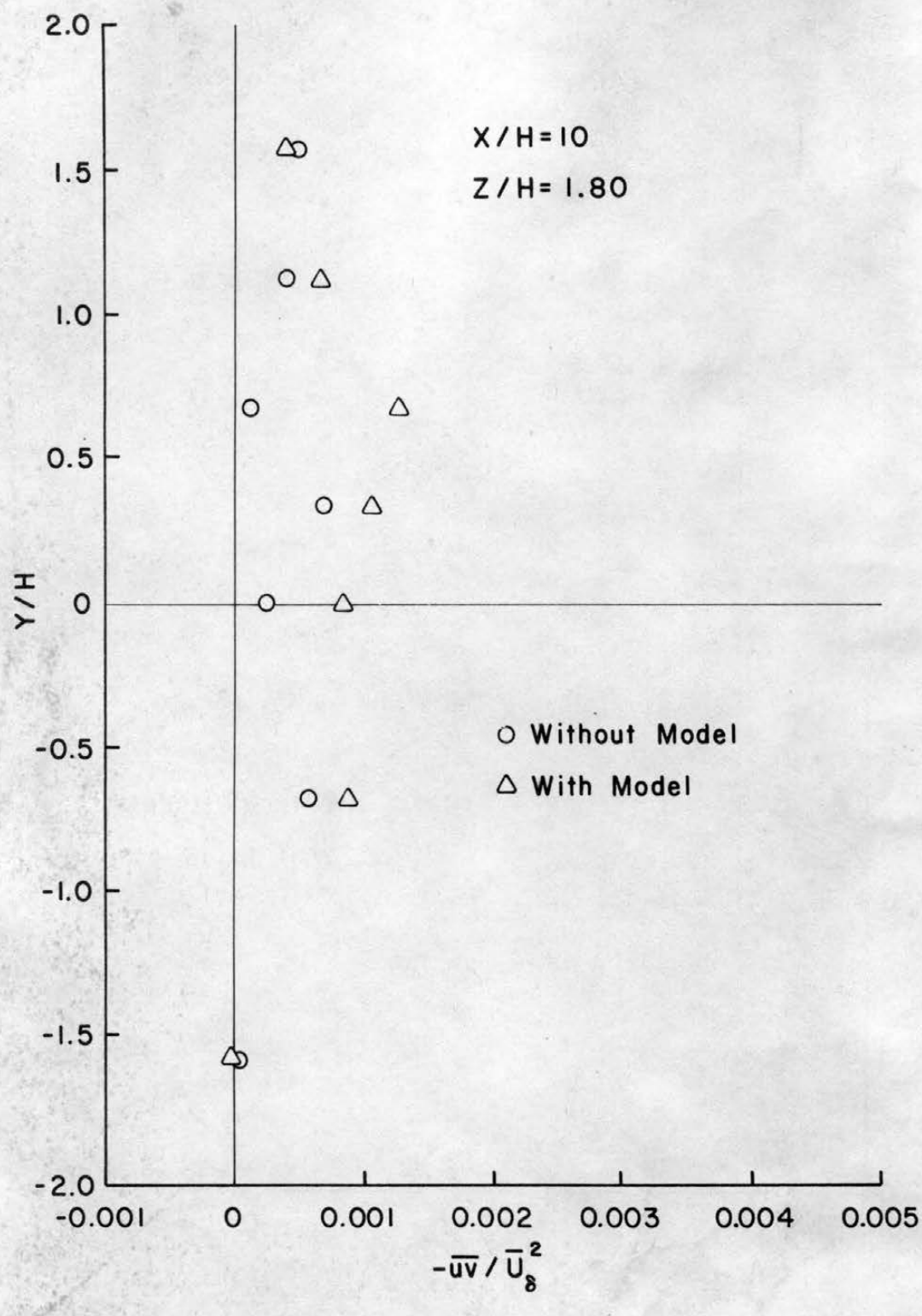

Figure 38c. Z/H = 1.80.

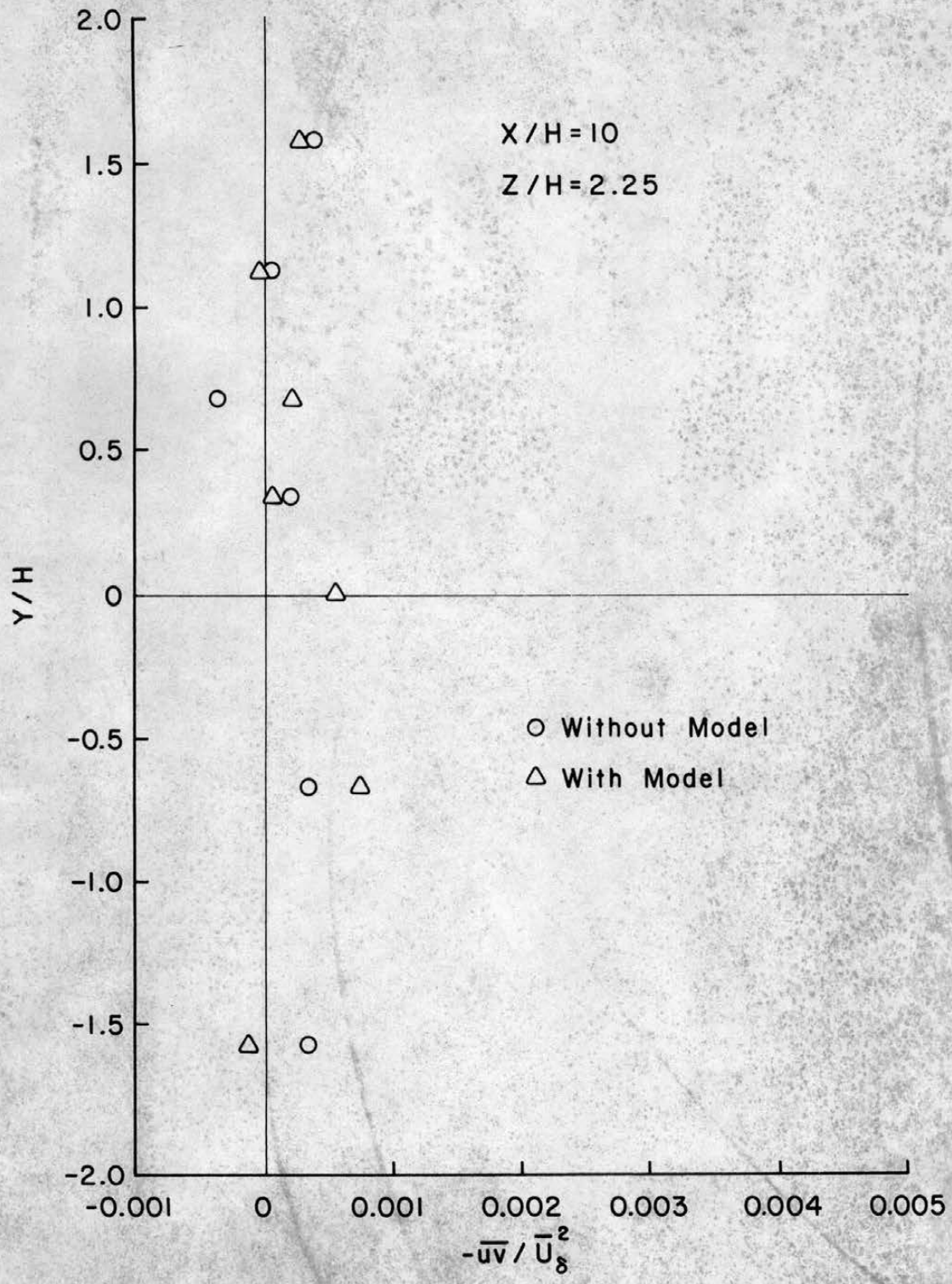

Figure 38d. Z/H = 2.25.